UNIVERSITY OF ROCHESTER
LABORATORY FOR LASER ENERGETICS

Volume 85
October–December 2000
DOE/SF/19460-378

LLE Review

Quarterly Report

About the Cover:

Inertial confinement fusion (ICF) research requires large-scale, multidimensional computer calculations to design ICF capsules. Nevertheless, the time-honored business of talking out these problems on the board and carrying out analytical calculations is necessary to address the underlying physics issues. Three of the co-authors of the article "Theory of the Hot-Spot Dynamics and Deceleration-Phase Instability of Imploding ICF Capsules" are shown in the cover photo engaged in an animated discussion regarding this work. The authors in the photo (left to right in the top photograph) are Professor Robert L. McCrory, Director, Laboratory for Laser Energetics (LLE) and Professor, Mechanical Engineering (ME); Professor Ricardo Betti, Associate Professor, ME, and Assistant Director for Academic Affairs (LLE); and Dr. Valeri Goncharov, Scientist, LLE.

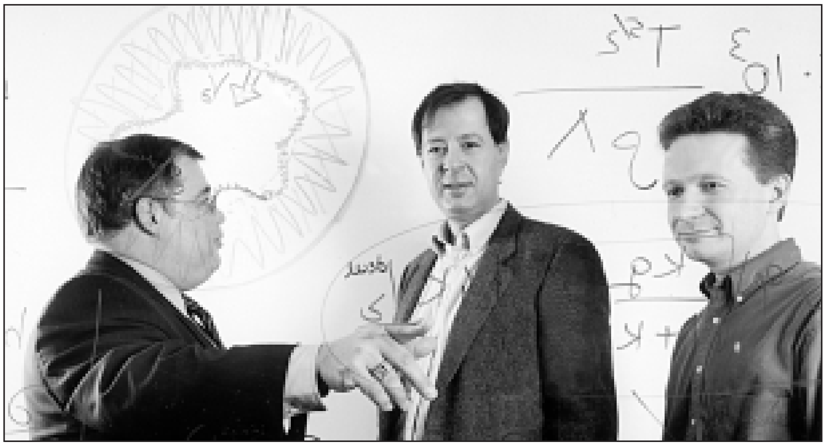

The work described in this volume includes current research at the Laboratory for Laser Energetics, which is supported by New York State Energy Research and Development Authority, the University of Rochester, the U.S. Department of Energy Office of Inertial Confinement Fusion under Cooperative Agreement No. DE-FC03-92SF19460, and other agencies.

Printed in the United States of America
Available from
National Technical Information Services
U.S. Department of Commerce
5285 Port Royal Road
Springfield, VA 22161

Price codes: Printed Copy A03
Microfiche A01

For questions or comments, contact John M. Soures, *Editor*, Laboratory for Laser Energetics, 250 East River Road, Rochester, NY 14623-1299, (716) 275-3866.

Worldwide-Web Home Page: http://www.lle.rochester.edu/

UNIVERSITY OF ROCHESTER
LABORATORY FOR LASER ENERGETICS

Volume 85
October–December 2000
DOE/SF/19460-378

LLE Review

Quarterly Report

Contents

In Brief

This volume of the LLE Review, covering October–December 2000, begins with an article by R. Betti, M. Umansky, V. Lobatchev, V. N. Goncharov, and R. L. McCrory, who report on the development of a model for the deceleration phase of an imploding inertial fusion capsule (p. 1). The model shows that the ablative flow off the inner shell surface plays a critical role in reducing the growth rate and suppressing short-wavelength modes in the deceleration-phase Rayleigh–Taylor instability.

Additional highlights of research presented in this issue are

- T. R. Boehly, J. A. Delettrez, J. P. Knauer, D. D. Meyerhofer, B. Yaakobi, R. P. J. Town, and D. Hoarty describe results (p. 11) of experiments conducted on OMEGA to assess the effects of shock heating on the stability of direct-drive inertial fusion capsules. Measurements indicate that pulses that rise rapidly to 10^{14} W/cm^2 produce shock-induced temperatures of ~25 eV, whereas more slowly rising pulses show less heating. A correlation is found between greater hydrodynamic stability for square-pulse drive (which has more shock heating) compared to the ramp-pulse drive that exhibits less shock heating and less stability.

- K. Xin and J. C. Lambropoulos report on a new model for material behavior under compression (p. 15). The model was motivated by the fact that fused silica densifies permanently under sufficiently large compressive stresses. It is also observed that the appearance of shear will facilitate densification. The model is based on a new constitutive law used to study spherical cavity expansion in material with densification.

- W. Bittle and R. Boni describe the design and performance of a selectable-streak-rate streak-camera deflection ramp generator (p. 21). This new method for generating streak-camera deflection voltage ramps uses a 50-Ω composite MOSFET/avalanche transistor step generator and a relay-selectable low-pass filter network. The design allows the remote selection of four different sweep rates and provides a 50-Ω interface to the streak camera’s deflection plates.

- A. V. Okishev, R. Boni, M. Millecchia, P. A. Jaanimagi, W. R. Donaldson, R. L. Keck, W. Seka, K. V. Dukelsky, M. A. Eronyan, V. S. Shevandin, G. A. Ermolaeva, G. Nikolaev, and V. B. Shilov discuss the development of a UV fiber-optic beam delivery system (p. 29) for the OMEGA 60-beam laser system. This new fiber optic system uses 15-m-long fibers with attenuation less than 220 dB/km (at a wavelength of 351 nm) to deliver optical pulses to the OMEGA multibeam, streak-camera-based pulse characterization system. The modal dispersion of the fibers is low enough to allow an overall bandwidth of the streak camera’s diagnostic system to be less than or equal to 30 GHz.

- G. Gol'tsman, O. Okunev, G. Chulkova, A. Lipatov, A. Dzardanov, K. Smirnov, A. Semenov, B. Voronov, C. Williams, and R. Sobolewski report (p. 34) on the fabrication and properties of a simple-to-manufacture and simple-to-operate NbN hot-electron photodetector (HEP) with picosecond response time, high intrinsic quantum efficiency, negligible dark counts, and the capability to detect single photons from the ultraviolet to the infrared wavelength range. Practical implementation of this device could lead to revolutionary progress in areas ranging from ultrafast free-space satellite communications through quantum computing and quantum cryptography to semiconductor integrated circuit testing.

- J. D. Zuegel, S. F. B. Morse, J. Mathers, D. Weiner, L. Hayes, and J. R. Fabretti present a preliminary design for the National Ignition Facility's (NIF's) 2-D SSD beam-smoothing system (p. 39). Broad-bandwidth-beam-smoothing techniques are critical to high-performance, direct-drive implosions. As a partner in the National Inertial Confinement Fusion (ICF) Program, LLE has the lead role in defining direct-drive requirements for NIF and preparing a preliminary 2-D SSD system design. A prototype NIF 2-D SSD preamplifier module (PAM) will be built and tested at LLE. This article describes the base-line system design for the NIF's direct-drive beam-smoothing system, which will be capable of 1-THz bandwidth in the ultraviolet, 50×100-μrad divergence, and 2×1 color cycles.

John M. Soures
Editor

Theory of the Hot-Spot Dynamics and Deceleration-Phase Instability of Imploding ICF Capsules

Introduction

In inertial confinement fusion[1] (ICF), a spherical shell of cryogenic deuterium and tritium (DT) filled with DT gas is accelerated by direct laser irradiation (direct drive) or x-rays produced by a high-Z enclosure (indirect drive). In direct-drive ICF, the laser pulse starts from a constant, low-intensity foot designed to drive a uniform shock through the shell. After the shock breaks out on the shell's inner surface, the latter expands forward, launching a shock in the gas and a rarefaction wave in the shell. As the rarefaction wave travels across the shell, the shell's outer surface moves at approximately constant velocity. When the rarefaction wave reaches the shell's outer surface, the latter starts accelerating and the so-called *acceleration phase* begins. At about the shock breakout time, the laser power begins to rise, first slowly and then more rapidly to keep the shell close to the shock front traveling inside the gas. A second shock originating within the shell is launched during the initial pulse rise and merges with the first shock before reaching the center of the capsule. The acceleration phase ends when the laser is turned off and the shell starts traveling at approximately constant velocity. Standard direct-drive pulse designs make use of such a sequence of two shocks merging into one, whereas the latest pulse designs of indirect-drive ICF make use of a sequence of four shocks[2] coalescing into one before reaching the center.

In both direct- and indirect-drive ICF, the single shock resulting from the multiple-shock coalescence travels in the gas in the form of a *strong* shock; i.e., $\Delta P/P_b >> 1$, where ΔP is the pressure jump across the shock and P_b is the gas pressure before the shock. Such a shock is reflected off the center of the capsule (return shock) and subsequently off the incoming inner shell surface, which in turn is impulsively decelerated. The shock reflected off the shell travels toward the center, where it is reflected again and subsequently reflected a second time from the shell. At each reflection off the shell, the latter is impulsively decelerated and the shock gets weaker until the pressure jump across the shock front is smaller than the pressure before the shock ($\Delta P/P_b < 1$). The time interval corresponding to the multiple shock reflections is referred to as the *impulsive deceleration phase*. Typically, the reflected shock becomes *weak* after the first or second reflection off the shell. At this point the material enclosed by the inner shell surface develops a fairly uniform pressure profile and is referred to as the *hot spot*. After the return shock reflects off the shell, the hot spot is formed, and its pressure is large enough that the shell velocity is lower than the hot-spot sound speed, i.e., the flow is subsonic. When the hot spot is formed, the shell is decelerated in a continuous (not impulsive) manner while acting like a piston on the hot spot. Such a continuous slowing down of the shell up to the stagnation point occurs over a period of a few hundred picoseconds and is referred to as the *continuous deceleration phase*. Figure 85.1 shows the time evolution of the deceleration g of a shell designed for direct-drive ignition[3] on the National Ignition Facility (NIF). The time $t = 0$ ns represents the stagnation point, and the continuous deceleration starts at about 200 ps before stagnation. The NIF capsule is a 345-μm-thick shell of DT ice with an inner radius of 1350 μm. The shell is filled with DT gas at a temperature of 18 K and a density of 2×10^{-4} g/cm^3. During the deceleration phase, the hot-spot pressure, density, and temperature increase until reaching the ignition conditions. If the shell is sufficiently dense, the ignited hot spot will trigger a propagating burn wave

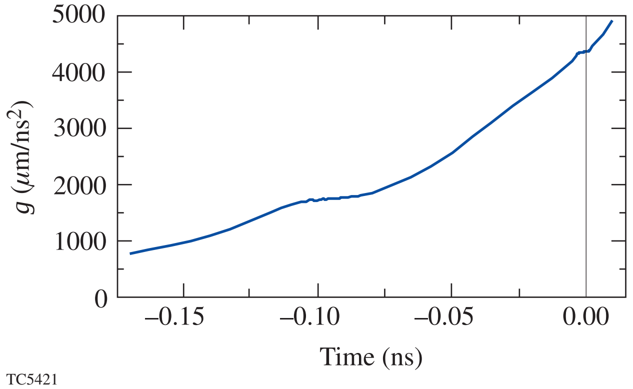

Figure 85.1
Time evolution of the inner-shell-surface deceleration for a direct-drive NIF capsule. Time $t = 0$ is the stagnation time.

in the shell and a significant fraction of the shell mass will undergo thermonuclear burn if the shell's areal density exceeds a few g/cm^2.

It is well known that the outer shell surface is unstable to the Rayleigh–Taylor (RT) instability during the acceleration phase; however, because of mass ablation, the instability growth rates are significantly reduced[4–10] with respect to their classical values. The theory of the RT instability in an accelerated planar foil has been carried out in Refs. 6–9, where the growth rate's dependence on the ablation velocity V_a, density-gradient scale length $L_m = \min\left[\rho\left(\rho'\right)^{-1}\right]$, front acceleration g, and power index for thermal conduction ν (here the thermal conductivity is approximated by $\kappa \approx \kappa_0 T^\nu$) is calculated by analytically solving the conservation equations. In Refs. 6–9, the stability of long ($kL_m < 1$) and short ($kL_m > 1$) wavelength modes is investigated for large and small Froude numbers (Fr), where $Fr = V_a^2 / gL_0$ and $L_0 = L_m \nu^\nu / (\nu+1)^{\nu+1}$. It is found that short-wavelength modes are completely suppressed when $Fr > 1$ and the unstable spectrum exhibits a cutoff at long wavelengths, i.e., $k_{\text{cutoff}} L_m < 1$. Instead, when $Fr < 1$, the cutoff occurs at short wavelengths ($k_{\text{cutoff}} L_m \sim 1/Fr^{1/3}$), and both long- and short-wavelength modes (up to the cutoff) are unstable. The stability analysis in Refs. 8 and 9 has been carried out separately for large and small Froude numbers as well as long and short wavelengths. In Ref. 10 the different growth-rate solutions have been combined into a single formula that asymptotically matches those solutions in the different parameter ranges.

Despite the significant growth-rate reduction induced by mass ablation and finite-density-gradient scale-length effects, the amplification of surface perturbations can be substantial, so the thickness of ICF shells must be chosen to prevent the shell from breaking up when the RT bubble amplitude equals the shell thickness.

Even when the shell integrity is preserved during the acceleration phase, the hot-spot ignition can be quenched[11] by the deceleration-phase RT instability. The latter is the instability of the inner shell surface that occurs when the shell is decelerated by the high pressure building up inside the hot spot. The deceleration-phase RT causes the cold shell material to penetrate and cool the hot spot, preventing it from achieving ignition conditions. Furthermore, if the inner-surface perturbation becomes nonlinear, a fraction of the shell's kinetic energy is used to feed the lateral shell motion induced by the instability, reducing the compression of the hot spot. Typical seeds for the deceleration-phase RT are the surface nonuniformities that feed through the shell from the outer surface during the acceleration-phase instability.

It is known that the deceleration-phase RT is classical[12] and all modes are unstable. The finite-density-gradient scale length[13] reduces the instability growth rates, which can be approximated by the classical fitting formula[1]

$$\gamma_{\text{dec}} \approx \sqrt{\frac{kg}{1+kL}}, \tag{1}$$

where L is the shell's density-gradient scale length and k is the perturbation wave number approximately equal to l/R with R being the hot-spot radius and l the mode number. Observe that Eq. (1) indicates that all modes are unstable, with the fastest-growing modes having short wavelengths ($kL >> 1$) and growth rates $\gamma_{\text{dec}}(kL >> 1) \simeq \sqrt{g/L}$. As described in Ref. 13, the finite-density-gradient scale length is produced by the thermal conduction inside the hot spot. It is shown in this article that mass ablation from the shell's inner surface significantly reduces the deceleration RT growth rates, leading to much lower growth rates than predicted by Eq. (1) and to a cutoff in the unstable spectrum. Mass ablation is caused by the heat flux leaving the hot spot and depositing on the shell's inner surface. We have calculated the ablation velocity and the shell's density-gradient scale length during the deceleration phase. Then, using the RT theory of Ref. 10, we have calculated the growth rates and compared them with the results of numerical simulations. For the direct-drive NIF-like capsule under consideration,[3] the cutoff mode number for the deceleration-phase RT is approximately $l_{\text{cutoff}} \approx 90$.

The remainder of this article is divided into two major sections that describe the hot-spot dynamics and the linear stability. The hot-spot model is valid from the beginning of the continuous deceleration phase (after the shock reflection off the shell) until the onset of the ignition process. The evolution of the hot-spot radius, mass, temperature, and density is calculated in terms of initial conditions and hot-spot pressure. The second section is devoted to the hydrodynamic stability analysis of the shell during the continuous deceleration phase. The growth rate of the RT instability is derived, including finite-density-gradient scale length and ablation velocity.

Hot-Spot Dynamics

The hot spot is a low-density plasma heated by the shock and by the *PdV* work of the cold, dense surrounding shell. Its mass is made of the ionized DT gas and the plasma ablated off the inner shell surface. The hot-spot dynamics is governed by the mass, momentum, and energy conservation equations. The energy equation must include the electronic thermal conduction and alpha-particle energy deposition. Bremsstrahlung radiation energy losses are neglected in this model because they add great complexity to the mathematical solution and their contribution is typically smaller than the mechanical work and/or the fusion power. The magnitude of the radiation losses is larger than the fusion power for temperatures below 4.4 keV, when the *PdV* work rate is typically greater than both radiation and fusion power. Thus at such low temperatures both radiation losses and alpha power are negligible with respect to the compression work rate. The *PdV* work rate decreases near the shell's stagnation point, where higher temperatures are reached within the hot spot. If such temperatures are well above 4.4 keV, the alpha-particle power is greater than the radiation losses and the bremsstrahlung term can again be neglected in the energy equation. The model described in this section may not apply to capsules that do not ignite or with small ignition margins (small mechanical work rate and low final temperatures) as their evolution can be significantly affected by radiation losses.

This model is expected to predict the main characteristics of the deceleration phase up to the onset of ignition. The actual ignition process in the hot spot is not accurately modeled because the alpha-particle energy is assumed to be locally deposited within the hot spot. Instead, the alpha-particle mean free path is typically of the same order of magnitude as the hot-spot radius, and a fraction of the alpha particles leaves the hot spot and is deposited on the shell's inner surface. Those alpha particles trigger the propagation of a burn wave in the cold, dense shell, which burns until it disassembles. The thermonuclear burn wave propagation is not described by our model and requires a diffusion (or kinetic) treatment of the alpha-particle population. Detailed analysis of the burn wave propagation and the effects of the RT instability on the capsule gain can be found in Ref. 11.

Even though the local deposition approximation used here is strictly valid only when all the alpha particles are absorbed within the hot spot, we artificially include the effect of alpha-particle diffusion by adding a multiplicative factor $\theta \le 1$ to the alpha power term. When $\theta < 1$, one should also include the alpha power deposited at the inner shell surface due to the $1-\theta$ fraction of leaking alpha particles. Such a contribution is not included in the derivation of the hot-spot profiles, ablation velocity, and density-gradient scale length because an analytic solution of the conservation equations could not be found. Thus, an additional limitation of this model is that the fraction of alpha particles leaving the hot spot is small compared to the fraction absorbed.

In conclusion, the model described below is suitable to describe the deceleration phase up to the onset of ignition, but it does not include the relevant physics pertaining to the ignition process or the burn wave propagation. We speculate that most of the RT instability growth occurs before ignition takes place when our model captures the essential physics of the hot-spot dynamics.

1. General Equations

The model is based on the Lagrangian form of the equations of motion as the boundary of the hot spot moves before and after stagnation. The Lagrangian equations of motion in spherical geometry can be written in the following form:

$$\frac{1}{\rho} = \frac{1}{3}\frac{\partial r^3}{\partial m}, \tag{2}$$

$$\frac{\partial U}{\partial t} + r^2 \frac{\partial P}{\partial m} = 0, \tag{3}$$

$$c_v \rho^{\Gamma-1} \frac{\partial}{\partial t}\frac{T}{\rho^{\Gamma-1}} = \frac{\partial}{\partial m}\kappa(T) r^4 \rho \frac{\partial T}{\partial m} + \frac{\rho}{4m_i^2}\theta E_\alpha \langle \sigma v \rangle, \tag{4}$$

where c_v = 3/2 A is the specific heat at constant volume, $A = m_i/(1+Z)$, m_i and Z are the ion mass and atomic number, respectively ($Z = 1$ for DT), Γ is the ratio of specific heats or adiabatic index ($\Gamma = 5/3$ for a monoatomic gas), $\kappa(T) = \kappa_0 T^\nu$ is the Spitzer thermal conductivity, $\nu = 5/2$, $E_\alpha = 3.5$ MeV, θ is the absorbed alpha-particle fraction, and $\langle \sigma v \rangle$ is the fusion reaction rate. The independent variable m is proportional to the mass within the radius r:

$$m = \int_0^r \rho(x,t) x^2 dx. \tag{5}$$

Equation (4) has been derived by using the standard ideal gas equation of state $P = \rho T/A$ and by neglecting bremsstrahlung losses. To solve the conservation equations, we adopt the subsonic flow ordering, which represents a good approximation after the shock transient. We let $t \sim R/C_s$ (or $t \sim R/U$), $r \sim R$, and $U \sim \in C_s$, where $\in << 1$ represents the flow Mach number. We find the solution of Eqs. (2)–(4) by a formal expansion in powers of $\in$. By inspection, Eq. (3) reduces to $\partial_m P = O(\in P/m)$, yielding

$$P \simeq P_{\mathrm{hs}}(t) \tag{6}$$

and reproducing the well-known flat pressure approximation.

The density in the energy equation can be eliminated by using the equation of state, and the fusion rate can be approximated with a quadratic term $\langle\sigma v\rangle = S_\alpha T^2$. Such an approximation is valid as long as $5 < T < 25$ keV, which is a temperature range relevant to ICF ignition experiments. After a straightforward manipulation, the energy equation can be rewritten in the following form:

$$c_v \frac{P_{\mathrm{hs}}(t)^{\Gamma-1}}{T^{\Gamma-1}} \frac{\partial}{\partial t} \frac{T^{\Gamma}}{P_{\mathrm{hs}}(t)^{\Gamma-1}}$$

$$= A\kappa_0 P_{\mathrm{hs}}(t) \frac{\partial}{\partial m} r^4 T^{\nu-1} \frac{\partial T}{\partial m} + \frac{\theta E_\alpha S_\alpha A}{M_i^2} P_{\mathrm{hs}}(t) T. \tag{7}$$

Equation (7) can be further simplified by defining the variables $\Pi \equiv T \big/ P_{\mathrm{hs}}^{1-1/\Gamma}$ and

$$\tau = \frac{3^{4/3}}{A^{1/3}} \frac{\kappa_0}{\Gamma c_v} \int_0^t P_{\mathrm{hs}}(t')^{\beta} dt' + \tau_0, \quad \beta = \frac{3(\Gamma-1)\nu - 1}{3\Gamma}, \tag{8}$$

where τ_0 is a constant to be determined by the initial conditions. Using Eq. (2) to determine the relation between the volume within the radius r and Π, one finds

$$r^3 = \frac{3}{A P_{\mathrm{hs}}(t)^{1/\Gamma}} \Phi, \qquad \Phi \equiv \int_0^m \Pi(m', \tau)\, dm', \tag{9}$$

and the energy equation can be rewritten in the following simple form:

$$\frac{\partial \Pi}{\partial \tau} = \frac{\partial}{\partial m} \Pi^{\nu-1} \Phi^{4/3} \frac{\partial \Pi}{\partial m} + \Delta_\alpha \Pi P_{\mathrm{hs}}(t)^{\delta}, \tag{10}$$

where

$$\delta = \frac{3\nu + 1 + 3\Gamma(1-\nu)}{3\Gamma}, \qquad \Delta_\alpha = \left(\frac{A}{3}\right)^{4/3} \frac{\theta E_\alpha S_\alpha}{4\kappa_0 m_i^2}. \tag{11}$$

The next step is to integrate Eq. (10) between 0 and m and to eliminate Π, leading to the following equation for Φ:

$$\frac{\partial \Phi}{\partial \tau} = \Phi^{4/3} \left(\frac{\partial \Phi}{\partial m}\right)^{\nu-1} \frac{\partial^2 \Phi}{\partial m^2} + \Delta_\alpha \Phi P_{\mathrm{hs}}(t)^{\delta}. \tag{12}$$

Observe that the α particle term on the right-hand side of Eq. (12) can be combined with the left-hand side by defining the new dependent (Ψ) and independent (η) variables:

$$\Psi = \Phi \exp\left[-D_\alpha \int_{t_0}^{t} P_{\mathrm{hs}}(t')\, dt'\right], \tag{13}$$

$$\eta = \eta_0 + \frac{3^{4/3}\kappa_0}{A^{1/3}\Gamma c_v} \int_{t_0}^{t} dt' P_{\mathrm{hs}}(t')^{\beta}$$

$$\exp\left[\left(\nu + \frac{1}{3}\right) D_\alpha \int_{t_0}^{t'} P_{\mathrm{hs}}(t'')\, dt''\right], \tag{14}$$

where $t = t_0$ represents the beginning of the continuous deceleration phase,

$$D_\alpha = \frac{\Gamma - 1}{4\Gamma} \frac{\theta E_\alpha S_\alpha}{(1+Z)^2}, \tag{15}$$

and η_0 is a new constant. After a short calculation, Eq. (12) can be rewritten in the following simple form:

$$\frac{\partial \Psi}{\partial \eta} = \Psi^{4/3} \left(\frac{\partial \Psi}{\partial m}\right)^{\nu-1} \frac{\partial^2 \Psi}{\partial m^2}. \tag{16}$$

A self-similar solution of Eq. (13) can be found by setting

$$\Psi = \left(\frac{a^{-3(\nu+1)}}{\eta^{3[1-\Omega(\nu+1)]}}\right)^{\frac{1}{3\nu+1}} F(\xi), \qquad \xi = \frac{am}{\eta^{\Omega}}, \tag{17}$$

where ξ and $F(\xi)$ are dimensionless and a is a constant with the dimensions of η^{Ω}/m to be determined using the initial conditions. Substituting Eq. (17) into Eq. (16) yields the following ordinary differential equation for $F(\xi)$:

$$\frac{3[1-\Omega(\nu+1)]}{3\nu+1}F+\Omega\xi\frac{dF}{d\xi}+F^{4/3}\left(\frac{dF}{d\xi}\right)^{\nu-1}\frac{d^2F}{d\xi^2}=0. \quad (18)$$

At the hot spot/shell interface, the temperature is considerably less than the central hot-spot temperature. Since the temperature is proportional to $dF/d\xi$, one can neglect corrections of the order of $T_{\text{shell}}/T(r=0)$ and look for solutions of Eq. (18), satisfying $dF/d\xi = 0$ at the hot-spot radius. The function F is proportional to the internal energy inside the hot spot and therefore positive by definition. Thus, the solution of Eq. (18) satisfying the boundary conditions can be found only when $\Omega = 1/(\nu+1)$, leading to the simplified hot-spot equation

$$\frac{1}{\nu+1}\xi+F^{4/3}\left(\frac{dF}{d\xi}\right)^{\nu-2}\frac{d^2F}{d\xi^2}=0. \quad (19)$$

The numerical solution of such an equation requires the derivative at $\xi = 0$, $F'(0)$. It can be easily shown, however, that all the physical quantities are independent of the choice of $F'(0)$; thus, without loss of generality, we set $F'(0) = 1$. The solution of Eq. (19) for $\nu = 5/2$, $F(0) = 0$, and $F'(0) = 1$ is shown in Fig. 85.2. Observe that $dF/d\xi$ (and therefore T) vanishes at $\xi_0 = 1.23$ and $F(\xi_0) = 0.70$. Defining the hot spot as the region with $\xi \le \xi_0$ leads to the following expression of the hot-spot mass:

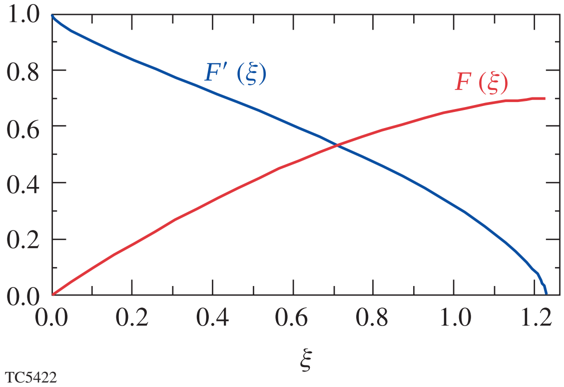

Figure 85.2
Functions $F(\xi)$ (proportional to the internal energy) and $F'(\xi)$ (proportional to the temperature) obtained from the numerical solution of Eq. (19) with $\nu = 5/2$, $F(0) = 0$, and $F'(0) = 1$. The hot spot is defined to be the region with $\xi \le 1.23$.

$$M_{\text{hs}} = 4\pi m_{\text{hs}} = 4\pi\xi_0\eta^{1/(\nu+1)}\big/a. \quad (20)$$

The constants a and η_0 can be determined from the initial conditions applied to Eqs. (20), (17), and (9), leading to

$$a=\left[\frac{3F(\xi_0)}{AR_{\text{hs}}(0)^3P_{\text{hs}}(0)^{1/\Gamma}}\right]^{\frac{3\nu+1}{3(\nu+1)}},\quad \eta_0=\left[\frac{aM_{\text{hs}}(0)}{4\pi\xi_0}\right]^{\nu+1}, \quad (21)$$

where $R_{\text{hs}}(0)$, $P_{\text{hs}}(0)$, and $M_{\text{hs}}(0)$ are the initial hot-spot radius, pressure, and mass, respectively. A short calculation using Eqs. (9), (13), (17), and (20) and the equation of state yields the relevant hot-spot parameters [mass, areal density (ρR), density, and temperature] as functions of the hot-spot pressure and radius:

$$M_{\text{hs}}(t)=\Bigg\{M_{\text{hs}}(0)^{\nu+1}+\chi_0\kappa_0A^{\nu+1}\int_{t_0}^{t}P_{\text{hs}}(t')^{\beta}\left[R_{\text{hs}}(t')^3P_{\text{hs}}(t')^{\frac{1}{\Gamma}}\right]^{\nu+\frac{1}{3}}dt'\Bigg\}^{\frac{1}{\nu+1}}, \quad (22)$$

$$\rho R\equiv\int_0^{R_{\text{hs}}}\rho dr=\mu_0\frac{M_{\text{hs}}(t)}{4\pi R_{\text{hs}}(t)^2}, \quad (23)$$

$$\rho_{\text{hs}}(m,t)=\frac{3M_{\text{hs}}(t)}{4\pi R_{\text{hs}}(t)^3}\,\frac{F(\xi_0)}{\xi_0F'(\xi)},$$

$$T_{\text{hs}}(m,t)=\frac{AP_{\text{hs}}(t)}{\rho_{\text{hs}}(m,t)}, \quad (24)$$

where

$$\chi_0\equiv\frac{\Gamma-1}{\Gamma}\,\frac{3^{1-\nu}(4\pi\xi_0)^{\nu+1}}{F(\xi_0)^{\nu+\frac{1}{3}}},$$

$$\mu_0=\frac{F(\xi_0)^{2/3}}{\xi_0}\int_0^{\xi_0}\frac{d\xi}{F(\xi)^{2/3}}. \quad (25)$$

For $\nu = 5/2$ and $\Gamma = 5/3$, we find $\mu_0 = 2.27$ and $\chi_0 = 3052.8$. Observe that the hot-spot mass increases with time at a rate that depends on the thermal conductivity coefficient. The mass increase is due to the ablation off the shell's inner surface. The hot-spot radius and pressure are related through Eq. (9), which can be rewritten by using the initial conditions, leading to

$$\frac{R_{\text{hs}}(t)^3}{R_{\text{hs}}(0)^3} = \left[\frac{P_{\text{hs}}(0)}{P_{\text{hs}}(t)}\right]^{1/\Gamma} \exp\left[D_\alpha \int_{t_0}^{t} P_{\text{hs}}(t)\right]. \qquad (26)$$

In the absence of alpha-particle heating ($D_\alpha = 0$), Eq. (26) yields $P_{\text{hs}} R_{\text{hs}}^{3\Gamma} = \text{constant}$, indicating that the hot spot behaves like a closed system that is adiabatically heated (PV^Γ = constant, where V is the volume). This result is somewhat surprising because the hot spot is not a closed system since its mass increases with time. From the energetic point of view, however, the hot spot is indeed insulated as the heat conduction losses are recycled into the hot spot via the ablated shell material. This can be shown by writing the total (internal + kinetic) energy equation in the conservative form:

$$\frac{\partial}{\partial t}\left(\frac{P}{\Gamma - 1} + \rho\frac{U^2}{2}\right) + \nabla \cdot \left[\mathbf{v}\left(\frac{\Gamma P}{\Gamma - 1} + \rho\frac{U^2}{2}\right)\right]$$

$$= \nabla \cdot \kappa(T)\nabla T + \frac{\rho^2}{4M_i^2}\theta E_\alpha \langle\sigma v\rangle. \qquad (27)$$

Using the subsonic flow assumption, we neglect the hot-spot kinetic energy with respect to the internal energy. Then, after approximating the fusion cross section with the quadratic form $\langle\sigma v\rangle \simeq S_\alpha T^2$, Eq. (27) is integrated over the hot-spot volume enclosed by the inner shell surface. At the inner surface, the shell material is cold and the thermal conduction can be neglected. A straightforward calculation leads to the following form of the energy equation:

$$\frac{d}{dt}\left(P_{\text{hs}} R_{\text{hs}}^3\right) + 3R_{\text{hs}}^2 P_{\text{hs}}\left[\Gamma U\left(R_{\text{hs}}, t\right) - \frac{dR_{\text{hs}}}{dt}\right]$$

$$= \Gamma D_\alpha P_{\text{hs}}^2 R_{\text{hs}}^3, \qquad (28)$$

where $U(R_{\text{hs}},t)$ is the flow velocity at the shell's inner surface. The flow velocity results from the combination of the inner surface motion and the ablative flow:

$$U\left(R_{\text{hs}}, t\right) = \dot{R}_{\text{hs}} - V_a, \qquad (29)$$

where V_a is the ablation velocity and $\dot{R}_{\text{hs}}$ scales with the implosion velocity. Since $V_a \ll \dot{R}_{\text{hs}}$, the ablation velocity can be neglected, and Eq. (28) yields the exact solution shown in Eq. (26). Thus, Eqs. (26) and (28) are equivalent forms of the energy equation. Notice that the heat conduction losses do not enter into the global energy balance of the hot spot. This is because the heat flux leaving the hot spot is deposited onto the shell's inner surface. A fraction of this energy is transformed into internal energy of the shell material ablating into the hot spot. The remaining fraction produces the *PdV* work done by the ablated plasma entering the hot spot against the hot-spot pressure. In other words, the energy leaving the hot spot in the form of heat conduction losses goes back into the hot spot in the form of internal energy and compression work of the ablated plasma. Therefore, conduction losses are not real energy losses and do not affect the global energy balance of the hot spot as shown by Eq. (28). It is important to emphasize that the hot-spot energy is proportional to its pressure and the conduction losses affect the hot-spot temperature but not its pressure. This conclusion implies that greater heat conduction losses would lower the temperature and raise the density (through larger ablation at the shell's inner surface), leaving the pressure ($P \sim \rho T$) unaltered.

Equation (26) relates hot-spot radius and pressure. All the hydrodynamic quantities shown in Eqs. (22)–(24) can therefore be expressed as functions of the pressure only, using Eq. (26). It follows that a fully self-consistent implosion model requires additional equations relating $P_{\text{hs}}(t)$ to the shell's properties. The coupling between the hot spot and the shell will be discussed in a forthcoming LLE Review. Here, we consider P_{hs} as a given function of time and use the hot-spot analysis developed in this section to determine the ablation velocity and density-gradient scale length.

2. Ablation Velocity and Density-Gradient Scale Length

An important result of the analysis carried out in the previous section concerns the hot-spot mass. Equation (22) shows that the hot-spot mass increases with time. Its rate of increase depends on the magnitude of the heat conduction coefficient κ_0 [here, $\kappa(T) = \kappa_0 T^\nu$] and the hot-spot pressure. The ablation velocity at the shell's inner surface follows by noticing that the mass ablation rate off the shell, $\dot{M}_a$, must equal the rate of change of the hot-spot mass $\dot{M}_{\text{hs}}$. Given the hot-spot radius R_{hs} and the shell's peak density ρ_{shell}, the ablation rate is $\dot{M}_a = 4\pi R_{\text{hs}}^2 \rho_{\text{shell}} V_a$, where V_a is the ablation velocity. Thus setting $\dot{M}_a = \dot{M}_{\text{hs}}$ yields the ablation velocity

$$V_a = \frac{\dot{M}_{\text{hs}}}{4\pi R_{\text{hs}}^2 \rho_{\text{shell}}}, \tag{30}$$

where $\dot{M}_{\text{hs}}$ can be determined from Eq. (22). Then, using the m-derivative of Φ to relate T and η, the ablation velocity can be written in terms of standard hot-spot and shell parameters

$$V_a = \frac{3(\Gamma-1)}{(\nu+1)\Gamma} \frac{\xi_0}{F'(0)^{\nu} F(\xi_0)^{1/3}} \frac{A\kappa_0 T_{\text{hs}}(0,t)^{\nu}}{\rho_{\text{shell}}(t) R_{\text{hs}}(t)}, \tag{31}$$

where both the central hot-spot temperature and radius depend only on the hot-spot pressure. Using $F'(0) = 1$ and $\nu = 5/2$ to solve Eq. (18) leads to $\xi_0 = 1.23$, $F(\xi_0) = 0.7$. The ablation velocity can then be calculated using standard ICF units, leading to the following simple form:

$$V_a(\mu\text{m/ns}) = 6\times 10^3 \frac{\left(T_{\text{keV}}^{\text{hs}}\right)^{5/2}}{R_{\mu\text{m}}^{\text{hs}}\, \rho_{\text{g/cm}^3}^{\text{shell}}\, \Lambda^{\text{hs}}}, \tag{32}$$

where R^{hs}, T^{hs}, and Λ^{hs} are the hot-spot radius in μm, central temperature g in keV, and Coulomb logarithm, and ρ^{shell} is the shell's peak density in g/cm^3. Figure 85.3 shows the temporal evolution of the ablation velocity for a direct-drive NIF capsule obtained from Eq. (32) and the result of numerical simulations using $\Lambda^{\text{hs}} = 5$.

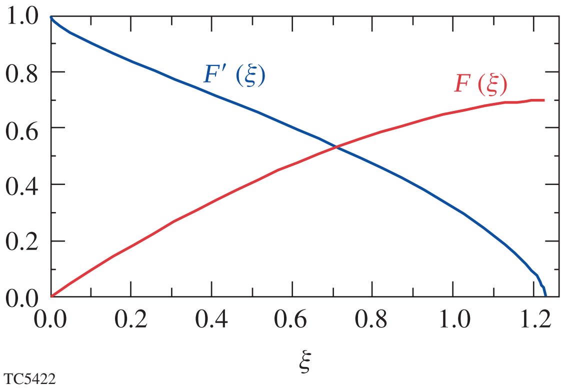

Figure 85.3
Evolution of the ablation velocity at the shell's inner surface of a NIF-like capsule as predicted by Eq. (32) (dashed) and the result of numerical simulations (solid).

In addition to the ablative stabilization, the RT growth rates are reduced by the well-known finite-density-gradient effects. Since the ablative flow at the inner shell surface is subsonic, the minimum density-gradient scale length can be calculated using the well-known isobaric model[14] characterized by the following approximate form of the energy equation:

$$\nabla \cdot \left[\mathbf{v}\frac{\Gamma P_{\text{hs}}(t)}{\Gamma-1} - \kappa\nabla T\right] = 0. \tag{33}$$

Integrating Eq. (33) and using the continuity of the mass flow (ρU = constant) leads to the following ordinary differential equation for the density profile near the shell's inner surface:

$$\frac{1}{\hat{\rho}}\frac{\partial\hat{\rho}}{\partial r} = \hat{\rho}^{\nu}\frac{(1-\hat{\rho})}{L_0}, \tag{34}$$

where $\hat{\rho} = \rho/\rho_{\text{shell}}$ is the density normalized to the peak density in the shell (ρ_{shell}) and

$$L_0 = \frac{\Gamma-1}{\Gamma}\frac{A\kappa\left(T_{\text{shell}}\right)}{\rho_{\text{shell}} V_a}. \tag{35}$$

Here $T_{\text{shell}} = AP_{\text{hs}}(t)/\rho_{\text{shell}}$ represents the temperature calculated at the peak of the density. Equation (35) is valid only near the shell's inner surface within a distance of the order of the length L_0. The minimum value of the density-gradient scale length (L_m) can be determined by setting to zero the radial derivative of Eq. (34). A straightforward manipulation yields

$$L_m = L_0\frac{(\nu+1)^{\nu+1}}{\nu^{\nu}}. \tag{36}$$

Using $\nu = 5/2$ in Eq. (36) and substituting Eq. (32) into Eq. (35) leads to the following simple expression of the density-gradient scale length:

$$L_m = 6.8\, R_{\text{hs}}\left[AP_{\text{hs}}(t)/\rho_{\text{shell}} T_{\text{hs}}(0,t)\right]^{5/2}, \tag{37}$$

where $P_{\text{hs}}(t)$ is the hot-spot pressure. Figure 85.4 shows the temporal evolution of L_m calculated from Eq. (37) and from the numerical simulations of a NIF direct-drive capsule. Observe that the density-gradient scale length is quite smaller than the hot-spot radius, implying that its stabilizing effects will impact only short-wavelength modes (large l-mode numbers).

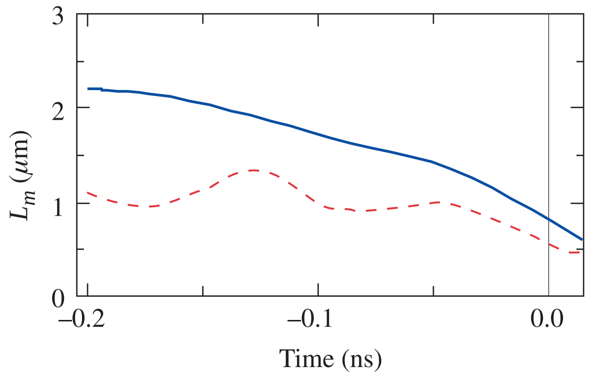

Figure 85.4
Evolution of the density-gradient scale length at the shell's inner surface of a NIF-like capsule as predicted by Eq. (37) (dashed) and the result of numerical simulations (solid).

In the next section, the theory developed in the **General Equations** section is used to calculate the hydrodynamic profiles inside the hot spot and to show how the profiles are affected by the ablation process.

3. Hot-Spot Profiles

The density, temperature, and velocity profiles inside the hot spot can be determined easily from the theory developed in the **Hot-Spot Dynamics** section. The theory is based on the solution of the gas dynamic equations in a Lagrangian form with m,t as independent variables. All the spatial profiles are described by the function $F(\xi)$, where $\xi = am/\eta^{2/7}$ for $\nu = 5/2$. Instead of the variable ξ, a more convenient expression of the profiles should make use of the spatial coordinate $\hat r \equiv r/R_{hs}(t)$. The relation between $\hat r$ and ξ can be found by rewriting Eq. (9) using Eqs. (26), (17), and (21). A simple manipulation yields the following relation:

$$\hat r^3 = \frac{F(\xi)}{F(\xi_0)}. \tag{38}$$

All the spatial hot-spot profiles for $\nu = 5/2$ can be found by inverting Eq. (38) and finding ξ in terms of $\hat r$; however, since $F(\xi)$ is not analytical, the inversion must be carried out numerically, leading to the following approximation for ξ and $F'(\xi)$:

$$\xi \approx \xi_0\left\{1-\left[1-\hat r^3\right]^{3/5}\right\}, \tag{39}$$

$$F'(\xi) \approx \frac{\left(1-\hat r^2\right)^{2/5}}{1-0.15\hat r^2}. \tag{40}$$

The hot-spot temperature profile follows immediately from Eq. (24) and Eq. (40) leading to

$$T_{hs}(r,t) \approx T_{hs}(0,t)\frac{\left(1-\hat r^2\right)^{2/5}}{1-0.15\,\hat r^2}. \tag{41}$$

When compared with the commonly used profile[1] $T_c = T_0\left(1-\hat r^2\right)^{2/7}$, Eq. (41) is in very good agreement except near the boundary of the hot spot $\hat r \approx 1$. The different behavior near the hot-spot boundary is relevant to the calculation of the heat flux leaving the hot spot, which is proportional to $\left[T^{5/2}d_{\hat r}T\right]_{\hat r=1}$. The common profile with the power 2/7 yields a finite heat flux while the profile given by Eq. (41) yields zero flux. Since the hot-spot boundary represents the cold shell's inner surface, the heat flux cannot propagate through the shell because the heat conductivity is negligible throughout the shell material. The correct temperature profiles must therefore produce a vanishing heat flux at the hot-spot boundary as indicated by Eq. (41). As mentioned in the **General Equations** section, the heat flux is absorbed on the shell's inner surface by the material that ablates into the hot spot.

The hot-spot density profile follows from Eq. (41) and the isobaric assumption, leading to

$$\rho_{hs}(r,t) \approx \rho_{hs}(0,t)\frac{1-0.15\,\hat r^2}{\left(1-\hat r^2\right)^{2/5}+\in}, \tag{42}$$

where the *ad hoc* term $\in \equiv 0.85\rho_{hs}(0,t)/\rho_{shell} << 1$ has been included to remove the singularity at $\hat r = 1$, which arises from the zero shell temperature approximation used to solve the hot-spot equation [Eq. (16)].

The velocity profile can be determined from the Lagrangian equation $u = \partial_t r$ and Eq. (9). Using the definition of the ablation velocity given in Eq. (30), the hot-spot velocity profile has the form

$$u(r,t) = \hat{r}\dot{R}_{\mathrm{hs}} - \frac{\xi(\hat{r})}{\xi_0}\frac{\rho_{\mathrm{shell}}}{\rho_{\mathrm{hs}}(r,t)}\frac{V_a}{\hat{r}^2}, \tag{43}$$

where $\xi(\hat{r})$ and $\rho_{\mathrm{hs}}(r,t)$ are given in Eqs. (38) and (43), respectively. During the deceleration phase, the velocity is negative (i.e., directed in the negative *r*-direction) and the velocity profile has a minimum (i.e., a maximum for the absolute value of *u*) due to the blowoff of the material ablated off the shell [the second term in Eq. (43)]. The minimum occurs at the radial position

$$\hat{r}_{\min} \approx \frac{1+0.6\hat{V}_b}{1+0.72\hat{V}_b}, \tag{44}$$

where $\hat{V}_b = \rho_{\mathrm{shell}}V_a/\rho_{\mathrm{hs}}(0,t)\left|\dot{R}_{\mathrm{hs}}\right|$. Near stagnation, $\hat{V}_b >> 1$, $\hat{r}_{\min} \approx 0.8$, and the velocity at the point of minimum is approximately

$$u(\hat{r}_{\min},t) \approx 0.8\ \dot{R}_{\mathrm{hs}} - 0.6\ V_a\frac{\rho_{\mathrm{shell}}}{\rho_{\mathrm{hs}}(r_{\min},t)}, \tag{45}$$

where $\rho_{\mathrm{hs}}(\hat{r}_{\min},t) \approx 1.46\ \rho_{\mathrm{hs}}(0,t)$ is the density at the location of minimum velocity. Observe that Eq. (45) is a useful tool for calculating the ablation velocity near stagnation from the numerical simulations because the velocity $u_{\min} = u(\hat{r}_{\min},t)$, and the densities $\rho_{\mathrm{hs}}(\hat{r}_{\min},t)$ and ρ_{shell} can be easily determined from the codes' output, while $\dot{R}_{\mathrm{hs}}$ is small and can be neglected.

Growth Rates of the Deceleration RT Instability

During the continuous deceleration phase after the interaction of the shell with the return shock, the shell's inner surface is unstable to the RT instability and any small perturbation in the hydrodynamic quantities would grow rapidly. The general formula derived in Ref. 10 yields the growth rate of the ablative RT as a function of the ablation velocity V_a, the shell deceleration *g*, the power index for thermal conduction $\nu = 5/2$, and the mode wave number $k \approx l/R_{\mathrm{hs}}$ for $l >> 1$. Since all such quantities are functions of time, the exponential growth of the linear perturbation occurs for sufficiently large *l*'s only when the typical growth time is shorter than the characteristic time scale of the one-dimensional evolution. In order to verify the theoretical results, we have carried out several 2-D single-mode simulations.

The 1-D code *LILAC*'s[15] output for the NIF-like capsule at 9.3 ns, characterizing the beginning of the coasting phase, was later used as input for a high-resolution Eulerian hydrocode.[16] The latter solves the single fluid mass, momentum, and energy equations, including Spitzer conduction, local alpha deposition, and bremsstrahlung on a very fine grid. The high resolution is needed to correctly simulate the growth of short-wavelength modes on the shell's inner surface. Aside from the bremsstrahlung losses, the code solves the same single fluid model on which the theory is based, providing a robust check of the theoretical results. The RT evolution is investigated by introducing a small-amplitude, 2-D perturbation of the hydrodynamic variables at about 200 ps before stagnation when the continuous deceleration phase begins.

For a direct-drive NIF-like capsule the deceleration phase occurs over an interval of approximately 200 ps. During that time (see Fig. 85.1) the deceleration varies from a few hundreds μm/ns^2 to about 4000 μm/ns^2, the ablation velocity increases from ~13 to ~25 μm/ns, the density-gradient scale length varies between 1 to 2 μm, and the hot-spot radius reduces from 100 μm to about 55 μm. The RT growth becomes significant during the last 100 ps before stagnation when the acceleration is large, and the hot-spot radius decreases from 75 to 55 μm. The growth rate of large *l* modes can be determined using the planar results of Ref. 10 derived for the acceleration-phase RT. For a NIF-like capsule during the continuous deceleration phase in the 100-ps interval before stagnation $<g> \approx 3100$ μm/ns^2, $<V_a> \approx 18$ μm/ns, $<L_m> \approx 1.5$ μm, and $<R_{\mathrm{hs}}> \approx 65$ μm, leading to a Froude number $Fr \approx 0.5$, where $Fr = V_a^2/gL_0$ and $L_0 = 0.12\,L_m$. Using Eq. (23) and Fig. 6 of Ref. 7, we determine the appropriate growth-rate formula:

$$\gamma = 0.9\sqrt{\frac{k\langle g\rangle}{1+k\langle L_m\rangle}} - 1.4\ k\langle V_a\rangle, \tag{46}$$

where $k \simeq l/R_{\mathrm{hs}}$ for large *l*'s.

Figure 85.5 compares the unstable spectrum calculated using Eq. (46) with $R_{\mathrm{hs}} = 65$ μm, the classical RT spectrum without ablation [Eq. (1) with $L = L_m$], and the results of numerical simulations. Except for $l = 2,4$ (open circles), the numerical growth rates are calculated in the 100-ps time interval before stagnation. The simulations of modes $l = 2,4$ (open circles) show a clear exponential growth only after the shell stagnation time, and their numerical growth rate is calculated during the 50-ps interval after stagnation. It is important to observe that the planar theory agrees well with the numerical results only for $l \geq 20$. Low l modes seem to grow faster (almost classically) than predicted by Eq. (46), indicating that convergence effects may reduce the ablative stabilization at low l. Furthermore, Fig. 85.5 shows that the finite ablation velocity off the shell's inner surface induces a cutoff in the RT unstable spectrum, suppressing short-wavelength modes with $l > 90$.

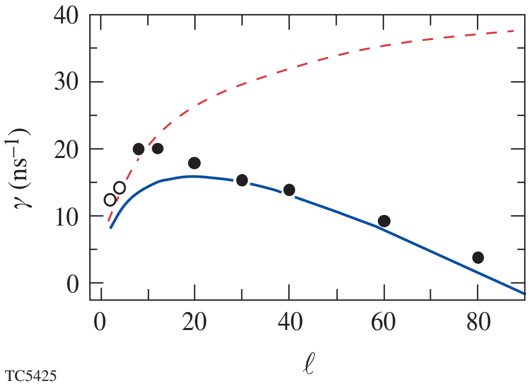

Figure 85.5
Growth rate versus mode number for the deceleration-phase RT of a NIF-like capsule as predicted by this work [Eq. (46) (solid)], by the classical fitting formula [Eq. (1)] with $L = L_m$ (dashed), and by the results of numerical simulations (open circles). The classical formula overestimates the growth rate of the instability for $l \gtrsim 10$.

Conclusion

In conclusion, an analytic model of the hot-spot dynamics has been developed, and all hot-spot profiles and hydrodynamic quantities relevant to the deceleration-phase instability have been determined. We have shown that the ablative flow off the shell's inner surface plays a crucial role in reducing the growth rate and suppressing short-wavelength modes in the deceleration-phase RT instability. The ablation velocity and the density-gradient scale length have been calculated in terms of standard hot-spot parameters. Using the theory of Ref. 10, the growth rate formula has been determined. Detailed numerical simulations have confirmed the theoretical results and have shown RT suppression at short wavelengths. Calculations of the unstable spectrum of a direct-drive NIF-like capsule[3] during the deceleration phase have indicated that the instability is suppressed for mode numbers $l > 90$.

ACKNOWLEDGMENT

This work was supported by the U.S. Department of Energy Office of Inertial Confinement Fusion under Cooperative Agreement No. DE-FC03-92SF19460, the University of Rochester, and the New York State Energy Research and Development Authority. The support of DOE does not constitute an endorsement by DOE of the views expressed in this article.

REFERENCES

1. J. D. Lindl, *Inertial Confinement Fusion: The Quest for Ignition and Energy Gain Using Indirect Drive* (Springer-Verlag, New York, 1998).
2. T. R. Dittrich *et al.*, Phys. Plasmas **6**, 2164 (1999).
3. Laboratory for Laser Energetics LLE Review **79**, 121, NTIS document No. DOE/SF/19460-317 (1999). Copies may be obtained from the National Technical Information Service, Springfield, VA 22161.
4. S. E. Bodner, Phys. Rev. Lett. **33**, 761 (1974).
5. H. Takabe *et al.*, Phys. Fluids **28**, 3676 (1985).
6. J. Sanz, Phys. Rev. Lett. **73**, 2700 (1994).
7. R. Betti, V. N. Goncharov, R. L. McCrory, P. Sorotokin, and C. P. Verdon, Phys. Plasmas **3**, 2122 (1996).
8. V. N. Goncharov, R. Betti, R. L. McCrory, P. Sorotokin, and C. P. Verdon, Phys. Plasmas **3**, 1402 (1996).
9. V. N. Goncharov, R. Betti, R. L. McCrory, and C. P. Verdon, Phys. Plasmas **3**, 4665 (1996).
10. R. Betti, V. N. Goncharov, R. L. McCrory, and C. P. Verdon, Phys. Plasmas **5**, 1446 (1998).
11. R. Kishony, "Ignition Criterion in Inertial Confinement Fusion Using Self-Similar Solutions, and the Effect of Perturbations on Ignition," Ph.D. thesis, Tel Aviv University, 1999.
12. F. Hattori, H. Takabe, and K. Mima, Phys. Fluids **29**, 1719 (1986).
13. M. Murakami, M. Shimoide, and K. Nishihara, Phys. Plasmas **2**, 3466 (1995).
14. H. J. Kull, Phys. Fluids B **1**, 170 (1989).
15. J. Delettrez and E. B. Goldman, Laboratory for Laser Energetics Report No. 36, University of Rochester (1976); also NTIS document No. DOE/SF/19460-118. Copies may be obtained from the National Technical Information Service, Springfield, VA 22161.
16. V. A. Lobatchev, "Hydrodynamics of Inertial Fusion Capsules: Feedout and Deceleration Phase Instability," Ph.D. thesis, University of Rochester, 2000.

The Effect of Shock Heating on the Stability of Laser-Driven Targets

Introduction

Hydrodynamic instability is a key issue for inertial confinement fusion (ICF).[1–3] The effects of the Rayleigh–Taylor (RT) instability can be reduced by shocks that heat the target shell, causing a slight decompression; this increases the ablation velocity and reduces the RT growth rate.[4,5] ICF target designs use shock heating to determine the implosion isentrope to establish a balance between performance and stability. This article presents the first experimental demonstration of a correlation between increased hydrodynamic stability and higher shock temperatures produced early in the interaction. This correlation is attributed to increased ablative stabilization resulting from target decompression caused by shock heating.

Experimental Implementation

Pulse shapes with different rise times were used to irradiate planar CH targets that had embedded Al layers whose temperatures were probed using time-resolved x-ray absorption spectroscopy. The 1*s*–2*p* Al absorption lines provided information about the ionization state of the Al, which, in turn, was used to infer both the shock-induced temperature and the heat-front propagation into the targets. The experiments indicate that steeply rising drive pulses produce shocks that heat the embedded Al layer to ~25 eV, while the slowly rising pulses produce shock heating below ~15 eV—our detection threshold. The heat front driven by the rapidly rising pulses showed the expected behavior, whereas the slowly rising pulses experienced mixing[6] caused by the RT instability that is seeded by laser imprinting.[7] Mix was not observed in the rapid-rise pulses because increased shock heating produces higher ablative stabilization.

In these experiments, 20-μm-thick CH targets were irradiated by six UV OMEGA[8] beams having 0.2-THz smoothing by spectral dispersion (SSD).[9] A 0.5-μm-thick layer of Al was embedded at either 5 or 10 μm below the irradiated surface. The laser pulses were either (1) a steeply rising (~200-ps rise time), nearly square shaped pulse with 1-ns duration and on-target intensity of $\sim 4 \times 10^{14}$ W/cm^2 or (2) a "ramp" pulse that rose linearly to 3×10^{14} W/cm^2 in 3 ns. One-dimensional calculations indicate that these pulses produce shock pressures of ~35 Mb and ~15 Mb, respectively. The targets were probed with x rays from a microdot of Sm that were dispersed by a streaked x-ray spectrometer.

Observations

Figure 85.6(a) shows the time-resolved absorption spectrum from a 20-μm-thick CH target (with the Al layer 10 μm deep) irradiated with the square pulse. Along the spectral direction, the 1*s*–2*p* absorption lines (dark bands) due to ionization states from F-like Al to Li-like Al are identified. The detailed structure of these transition arrays is not re-

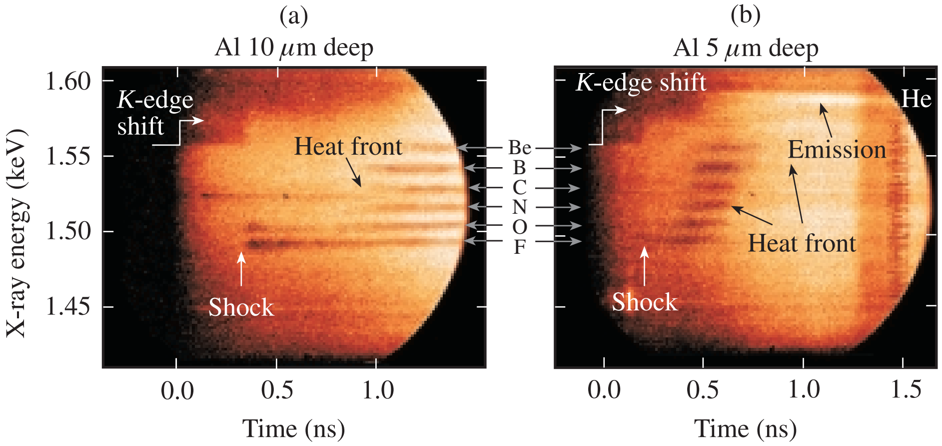

S18244, S18243
E10346

Figure 85.6
(a) Time-resolved absorption spectrum (dark horizontal bands) from an Al layer embedded 10 μm deep in a 20-μm-CH target irradiated by a square pulse. The F- and O-like absorption lines appear at ~325 ps due to shock heating. Later (~800 ps), higher ionization states occur when the heat front reaches the Al. (b) Absorption spectrum with the Al layer 5 μm deep. The F- and O-like absorption lines appear at ~200 ps and the heat front arrives at ~400 ps. He-like Al *emission* is observed when the heat front reaches the Al.

solved, but their mean energies and widths are consistent with predictions[10] and other observations.[11] The data in Fig. 85.6(a) indicate that both F-like and O-like lines appear at ~325 ps, and then later at ~800 ps, higher ionization states appear in progression.

Time is referenced to the start of the drive pulse that is preceded 300 ps by the backlighter. This allows observation of the *K*-shell absorption edge (at ~1.56 keV) in *cold* Al. At approximately the same time that the F-like and O-like lines appear, the *K* edge shifts to higher energy. This results primarily from the change in ionization of the Al ions. Later, as higher ionization states (N-like and above) appear, the *K* edge shifts to higher energy.

The abrupt onset of the F-like and O-like absorption lines is caused by shock heating of the Al layer; the higher ionization states (that appear later at a time ~800 ps) result from the incipient heating by the laser-driven heat front. These dynamics are confirmed by data from a target with the Al layer closer to the surface. Figure 85.6(b) is the spectrum from an experiment with the Al layer 5 μm deep. Here the onset of the F-like and O-like Al absorption lines is not clear, but one can readily see the abrupt change in the *K*-edge energy occurring at ~200 ps, consistent with the shock speed inferred from Fig. 85.6(a). Here the heat front also arrives earlier (~400 ps), but, in this case, the heating is sufficient to not only create absorption in higher ionization states but also produce He-like *emission*. The He-like emission occurs because the heat front has penetrated the 5 μm CH, and has then heated and ablated the Al. The absorption lines are short lived because the temperature rises sufficiently to "burn through" these states, thereby reducing the population in the lower tail of the charge-state distribution.

The dependence of shock heating on the temporal profile of the drive was measured by irradiating similar targets with the ramp pulse. Figure 85.7 shows an extended temporal record of absorption spectra from a target having the Al layer 5 μm deep and irradiated by the ramp pulse. The backlighter produces bright, broadband emission that ceases at ~2 ns. Coincidentally at that time He-like Al emission begins, which indicates that portions of the Al are heated to over 500 eV. Preceding this emission, no Al absorption lines (1.48 to 1.56 keV) are observed. Similar experiments on targets with the Al 10 μm deep also showed no absorption lines on these shots; the He-like emission occurred ~400 ps later than that shown in Fig. 85.7. These results are significant for two reasons: (1) They indicate the absence of significant shock heating before emission begins. (Note, however, that the *K* edge at 1.56 keV becomes diffuse at about 600 ps, suggesting some low-level shock heating.) (2) The lack of absorption lines preceding the He-like emission suggests that Al is instantaneously heated from <15 eV to >500 eV, contrary to expected behavior. Heat fronts in both directly driven[12] and indirectly driven targets[11] normally exhibit a succession of Al absorption lines that appear before the emission lines, as in Fig. 85.6(b).

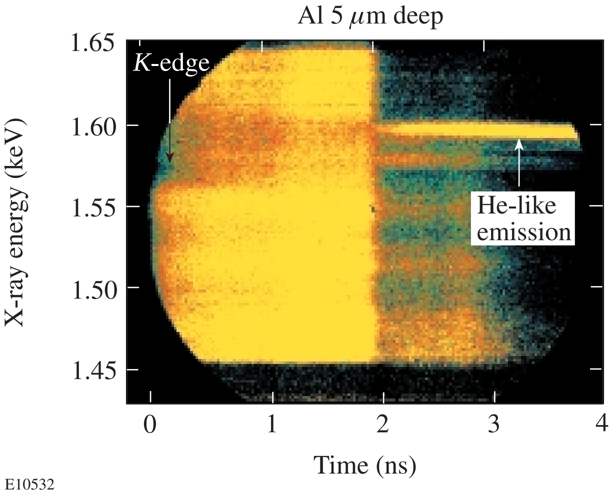

Figure 85.7
Absorption spectra from a target with the Al layer 5 μm deep and irradiated by a ramp pulse. No Al absorption lines are observed preceding the Al He-like emission lines that begin at ~1.9 ns.

In summary, the slowly rising ramp pulse produces less shock heating (no absorption lines) than the square pulse, and targets driven by the ramp pulse show no Al absorption lines even in the presence of He-like emission. The latter observation will be attributed to the effects of RT instability, while the former will confirm the correlation of ablative stabilization with shock heating.

Analysis and Discussion

The relative populations of Al charge states and the resulting absorption spectra were calculated for steady-state conditions at various temperatures.[13] This allowed the Al temperature to be inferred as a function of time. Figure 85.8 shows the Al temperature measured (points) and predicted (curves) by 1-D simulations (*LILAC*[14]). Figure 85.8(a) compares calculations and measurements for square-pulse irradiation of targets with the Al layer 5 μm deep (solid line and circles) and 10 μm deep (dashed line and triangles). Both the shock heating of the Al to ~25 eV and the heat-front penetration (≥40 eV) are correctly predicted by the 1-D simulations, indicating stable target behavior. The minor discrepancy in timing of the heat-front arrival times is likely the result of 2-D effects (see below). The lower limit for this measurement technique is the onset of F-like absorption lines that occurs at about 15 eV. The error bars indicate a ±100-ps timing uncertainty in the camera and a ±10-eV precision of the temperature measurement.

Similar temperature profiles for the ramp pulse are shown in Fig. 85.8(b) [5 μm deep (solid/circles); 10 μm deep (dashed/triangles)]. Since there were no absorption lines in the data, only the onset times for Al emission (defined as 500 eV) are shown. The predicted temperatures are below the ~15-eV experimental detection threshold until about 1.7 ns, when the heat front arrives at the Al, which reaches ~500 eV at 1.9 ns for the 5-μm case. The 10-μm case is not predicted to be heated above ~40 eV, yet the experiment reaches 500 eV at ~2.3 ns. The temperature rise predicted (by a 1-D code) for the ramp pulse is similar to that for the square pulse [Fig. 85.8(a)], indicating that the lack of absorption lines is not due to a steep temperature rise.

To explain the observation that the heat front reaches the 10-μm-deep Al layer and the He-like emission occurs with no preceding Al absorption lines, the existence of a mixing region is postulated. The emission lines could result from Al that is prematurely mixed into the ablation region.[6] Using the model discussed in Ref. 15, the thickness of that mix layer was calculated and then added to the depth predicted by 1-D simulations. The mix layer is produced by the RT instability that amplifies imprinted perturbations,[7] producing considerable two-dimensional effects. The model uses the measured spectrum of irradiation nonuniformities to calculate the imprinted perturbations, and then calculates their growth[16] and saturation.[17] The curves in Fig. 85.9 show the calculated location of the ablation surface (the point of steepest density gradient) in uncompressed CH thickness for the square and ramp pulses. The heavy lines are the predictions of 1-D calculations, and the shaded regions are the calculated mix layers centered on those predictions. The data represent the times when the Al layer (buried at the plotted depth) begins to produce He-like emission. Once ablated, this material must traverse the conduction zone before it is heated in the corona. The square-pulse data are not significantly affected by the RT instability and are therefore reasonably predicted by 1-D simulations. In contrast, the ramp pulse has a mix layer that affects the apparent penetration at both 5- and 10-μm depths in the original target. [The temporal offset (~250 ps) between the data and simulations corresponds to the time for the Al to travel from the ablation surface to the 500-eV isotherm.[18]] This explains both the unexpected emission from the Al [10-μm result in Fig. 85.8(b)] and the lack of preceding absorption lines for the 5- and 10-μm cases. Specifically, the RT spikes can "leach" Al from the embedded layer out into the corona (where it emits), whereas the Al in the bubbles has not been heated significantly and therefore has no absorption signature. The relative size of the bubbles and spikes is such that the bubbles dominate the spectroscopic radiography (no absorption line), while the bright (but smaller-sized) spikes are detected in emission but not resolved in absorption.

Simulations indicate that targets driven by either the square or ramp pulse have traveled ~50 μm when the heat front has penetrated 5 μm of CH. Thus, in the absence of any stabilizing mechanisms, both pulses should experience similar RT growth. Targets irradiated by these two pulse shapes behave differently because the square pulse produces a shock that heats the target

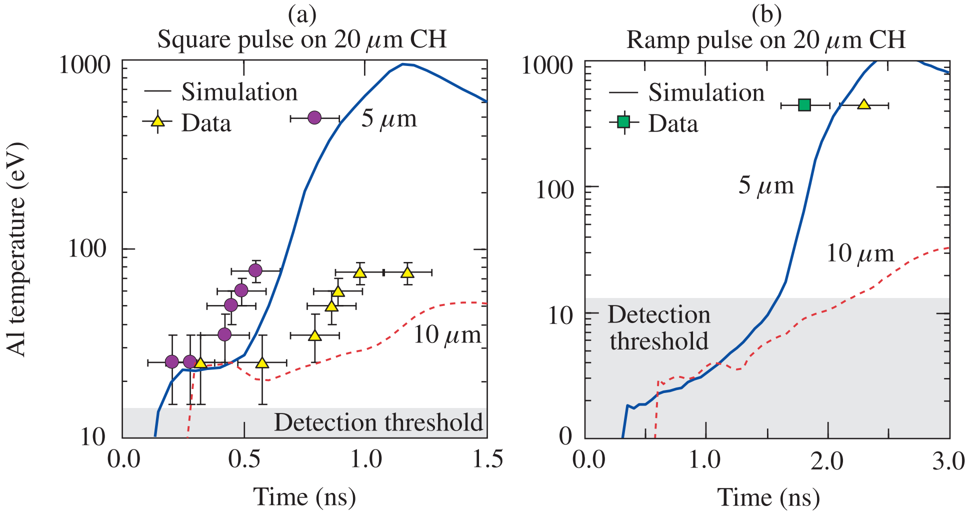
(a)
Square pulse on 20 μm CH

(b)
Ramp pulse on 20 μm CH

E10476, E10477

Figure 85.8
Comparison of the temperatures of the embedded Al layer as predicted by the 1-D code *LILAC* (curves) for various experiments and experimental data (points). (a) Square pulse driving the 5-μm case (solid/circles) and the 10-μm case (dashed/triangles). (b) Ramp pulse driving the 5-μm case (solid/circles) and the 10-μm case (dashed/triangles). Ramp-pulse data were present only for emission lines.

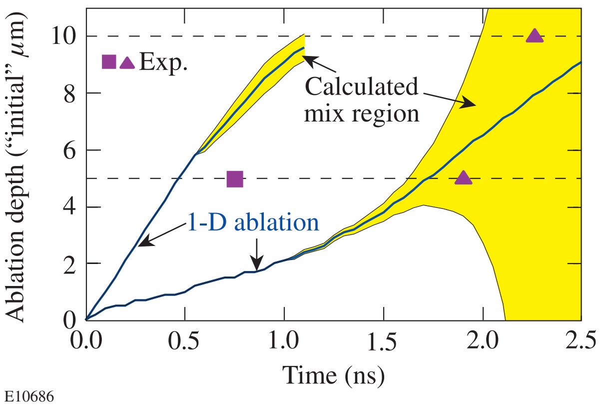

Figure 85.9
The ablation depths in uncompressed CH thickness. The heavy lines are the 1-D simulations, and the shaded regions are the calculated thickness of RT mixing. The measured penetration times are plotted at the embedded layer depths for the experiments.

to ~25 eV, causing it to decompress, thereby increasing the ablation velocity. This lowers the RT growth rate compared to that of the ramp pulse, which experiences less shock heating (<15 eV) and therefore little ablative stabilization. The simulations (which correctly model the observed shock temperatures) confirm that the square pulse produces ablation velocities that are as much as five times larger than those for the ramp pulse.

It has been shown that for the square-pulse drive, 1-D simulations accurately predict the observed shock heating (~25 eV) produced by an ~35-Mb shock and the heat-front penetration depth. In contrast, the ramp pulses produce ~15-Mb shocks that do not appreciably heat the target (<15 eV). The targets exhibit apparent anomalous heat-front penetration that results from two-dimensional effects caused by the RT instability.[15] Simulations of these experiments indicate that the shock heating produced by rapidly rising pulses causes the target to decompress, creating higher ablation velocities that reduce the RT growth rates. In contrast, the slowly rising pulse causes considerably less shock heating, producing less ablative stabilization, and therefore experiences significant effects due to the RT instability. This confirms the expected effect of shock heating and ablative stabilization on the stability of directly driven ICF targets.

ACKNOWLEDGMENT

This work was supported by the U.S. Department of Energy Office of Inertial Confinement Fusion under Cooperative Agreement No. DE-FC03-92SF19460, the University of Rochester, and the New York State Energy Research and Development Authority. The support of DOE does not constitute an endorsement by DOE of the views expressed in this article.

REFERENCES

1. J. D. Lindl, Phys. Plasmas **2**, 3933 (1995).
2. S. E. Bodner, D. G. Colombant, J. H. Gardner, R. H. Lehmberg, S. P. Obenschain, L. Phillips, A. J. Schmitt, J. D. Sethian, R. L. McCrory, W. Seka, C. P. Verdon, J. P. Knauer, B. B. Afeyan, and H. T. Powell, Phys. Plasmas **5**, 1901 (1998).
3. J. D. Kilkenny, S. G. Glendinning, S. W. Haan, B. A. Hammel, J. D. Lindl, D. Munro, B. A. Remington, S. V. Weber, J. P. Knauer, and C. P. Verdon, Phys. Plasmas **1**, 1379 (1994).
4. H. Takabe, L. Montierth, and R. L. Morse, Phys. Fluids **26**, 2299 (1983).
5. R. Betti, V. N. Goncharov, R. L. McCrory, P. Sorotokin, and C. P. Verdon, Phys. Plasmas **3**, 2122 (1996).
6. D. K. Bradley, J. A. Delettrez, and C. P. Verdon, Phys. Rev. Lett. **68**, 2774 (1992).
7. T. R. Boehly, V. N. Goncharov, O. Gotchev, J. P. Knauer, D. D. Meyerhofer, D. Oron, S. P. Regan, Y. Srebro, W. Seka, D. Shvarts, S. Skupsky, and V. A. Smalyuk, "The Effect of Plasma Formation Rate and Beam Smoothing on Laser Imprinting," submitted to Physical Review Letters.
8. T. R. Boehly, D. L. Brown, R. S. Craxton, R. L. Keck, J. P. Knauer, J. H. Kelly, T. J. Kessler, S. A. Kumpan, S. J. Loucks, S. A. Letzring, F. J. Marshall, R. L. McCrory, S. F. B. Morse, W. Seka, J. M. Soures, and C. P. Verdon, Opt. Commun. **133**, 495 (1997).
9. S. Skupsky and R. S. Craxton, Phys. Plasmas **6**, 2157 (1999).
10. C. Chenais-Popovics *et al.*, Phys. Rev. A **42**, 4788 (1990).
11. T. S. Perry *et al.*, J. Quant. Spectrosc. Radiat. Transf. **51**, 273 (1994).
12. D. Hoarty *et al.*, Phys. Rev. Lett. **82**, 3070 (1999).
13. D. Hoarty *et al.*, Phys. Rev. Lett. **78**, 3322 (1997).
14. M. C. Richardson, P. W. McKenty, F. J. Marshall, C. P. Verdon, J. M. Soures, R. L. McCrory, O. Barnouin, R. S. Craxton, J. Delettrez, R. L. Hutchison, P. A. Jaanimagi, R. Keck, T. Kessler, H. Kim, S. A. Letzring, D. M. Roback, W. Seka, S. Skupsky, B. Yaakobi, S. M. Lane, and S. Prussin, in *Laser Interaction and Related Plasma Phenomena*, edited by H. Hora and G. H. Miley (Plenum Publishing, New York, 1986), Vol. 7, pp. 421–448.
15. J. Delettrez, D. K. Bradley, and C. P. Verdon, Phys. Plasmas **1**, 2342 (1994).
16. R. Betti, V. N. Goncharov, R. L. McCrory, and C. P. Verdon, Phys. Plasmas **5**, 1446 (1998).
17. S. W. Haan, Phys. Rev. A **39**, 5812 (1989).
18. J. A. Delettrez, S. P. Regan, P. B. Radha, and R. P. J. Town, Bull. Am. Phys. Soc. **45**, 224 (2000).

Spherical Cavity Expansion in Material with Densification

Introduction

Fused silica (SiO_2) exhibits some unique features when it is ground or polished. It also densifies permanently under large compressive stresses at room temperature;[1–3] up to 15% permanent densification has been observed.[2,3] The experimental data for densification from different works, however, are obviously inconsistent,[4] which may result from different levels of shear stresses present in the experiments. The molecular dynamics simulation by Tse *et al.*[5] proved this suggestion by showing that the densification is caused by extensive bending of atomic bonds, even under pure hydrostatic pressure. Based on these observations, a new constitutive law was suggested by Lambropoulos *et al.*[6] for this kind of material.[7]

To understand the material behavior under compression, the cavity expansion problem is solved analytically. Both associated and non-associated flow theories have been studied. A densification parameter has been introduced in the proposed material model. The material is assumed to be perfectly plastic; however, the introduction of densification produces an effect similar to hardening.

Constitutive Model

The traditional shear flow theory cannot describe the plastic behavior of fused silica because the permanent densification is so large that its effects cannot be neglected. Experiments and observations on fused silica have suggested that the shear will facilitate the densification.[4,5,7] Lambropoulos *et al.*[6] suggested a new material model to describe this kind of material. The yield surface is defined by the effective stress

$$\sigma_e = -\alpha\sigma_m + (1-\alpha)\tau_e, \tag{1}$$

where

$$\sigma_m = \frac{1}{3}\sigma_{kk} = \frac{1}{3}\left(\sigma_{11} + \sigma_{22} + \sigma_{33}\right),$$

$$\tau_e = \sqrt{\frac{1}{2}s_{ij}s_{ij}}, \quad s_{ij} = \sigma_{ij} - \sigma_m\delta_{ij},$$

and α is the densification parameter, which ranges from 0 to 1. Here the summation convention is used. δ_{ij} is the Kronecker delta. For pure hydrostatic compression, where $\sigma_{11} = \sigma_{22} = \sigma_{33} = -p$, the mean hydrostatic stress $\sigma_m = -p$ and effective shear $\tau_e = 0$. For pure shear, $\sigma_m = 0$ and $\tau_e = |\tau|$. For uniaxial tension, $\sigma_m = \sigma/3$ and $\tau_e = \sigma/\sqrt{3}$. Notice that τ_e is always positive.

The material yields when $\sigma_e > Y$. The normal of yield surface can be expressed as

$$\mu_{ij} = \frac{\partial f}{\partial \sigma_{ij}} = -\frac{\alpha}{3}\delta_{ij} + \frac{(1-\alpha)}{2}\frac{s_{ij}}{\tau_e}. \tag{2}$$

When the inner product $\mu_{ij} d\sigma_{ij} > 0$, the small change of stress $d\sigma_{ij}$ causes further deformation loading. When $\mu_{ij} d\sigma_{ij} < 0$, it is unloading. Permanent strains ε_{ij}^p evolve as

$$d\varepsilon_{ij}^p = \begin{cases} 0, & \text{if } \mu_{ij} d\sigma_{ij} \le 0 \\ \ne 0, & \text{if } \mu_{ij} d\sigma_{ij} > 0 \end{cases}. \tag{3}$$

With continued loading, we assume that the permanent strains are not affected by the rate of loading; thus, the flow rule gives

$$d\varepsilon_{ij}^p = d\lambda \frac{\partial g}{\partial \sigma_{ij}}, \quad g\left(\sigma_{ij}\right) = -\alpha'\sigma_m + \left(1-\alpha'\right)\tau_e, \tag{4}$$

where $g(\sigma_{ij})$ is the flow potential. Generally the material constant α' in Eq. (4) is different from α in Eq. (1), which is called the non-associated flow theory. For special case $\alpha = \alpha'$, called the associated flow theory, the permanent strain increment is normal to the yield surface in stress space.

By using the principle of plastic work equivalence $\sigma_{ij} d\varepsilon_{ij}^p = c\sigma_e d\bar{\varepsilon}^p$, where c is a numerical factor, the plastic strain increment can be solved as

$$d\varepsilon_{ij}^{p} = \frac{d\bar{\varepsilon}^{p}}{C}\left(-\frac{\alpha'}{3}\delta_{ij} + \frac{1-\alpha'}{2}\frac{s_{ij}}{\tau_e}\right), \tag{5}$$

where

$$C = \sqrt{\frac{2}{9}\alpha'^{2} + \frac{1}{3}\left(1-\alpha'\right)^{2}}\,.$$

For a standard elastic theory (Hooke's law), the elastic strain increment is

$$d\varepsilon_{ij}^{e} = \frac{1}{2G}ds_{ij} + \frac{\left(1-2\nu\right)}{E}\delta_{ij}d\sigma_{m}\,, \tag{6}$$

where G is shear modulus, defined as $G = E/2(1+\nu)$. Then the total strain increment is given by

$$d\varepsilon_{ij} = d\varepsilon_{ij}^{e} + d\varepsilon_{ij}^{p}. \tag{7}$$

The incremental stress–strain relation, written in tensor format, is

$$d\sigma_{ij} = D_{ijkl}\,d\varepsilon_{kl}\,, \tag{8}$$

where the fourth-order tensor D_{ijkl} is the material's incremental constitutive law matrix.

Cavity Expansion

A spherical cavity embedded in an infinite medium with an initial radius a_0 is subjected to inner pressure P. With the increase of P, the cavity wall expands. When the pressure is larger than the initial yield pressure P_c, a plastic zone forms outside the cavity wall. Due to the symmetry, a spherical polar Lagrangian system (r, θ, φ) at the center of the cavity has been used. The material deforms only along the radius, and the displacement is a function of the radius only. There are only three nonzero stresses $\left(\sigma_r,\sigma_\theta,\sigma_\varphi\right)$ and strains $\left(\varepsilon_r,\varepsilon_\theta,\varepsilon_\varphi\right)$. By symmetry, we also have $\sigma_\theta = \sigma_\varphi$ and $\varepsilon_\theta = \varepsilon_\varphi$. Then the equilibrium equations reduce to

$$r\frac{d\sigma_r}{dr} + 2\left(\sigma_r - \sigma_\theta\right) = 0. \tag{9}$$

From elastic solution and yield function, the initial yield pressure is

$$P_c = \frac{2\sqrt{3}}{3\left(1-\alpha\right)}Y. \tag{10}$$

Equation (10) is plotted in Fig. 85.10. With the increase of α, the material yields at higher inner pressure.

It can be proved that $\sigma_\theta > \sigma_r$ at any point, so the effective stress can be simplified to

$$\sigma_e = -\frac{\alpha}{3}\left(\sigma_r + 2\sigma_\theta\right) + \frac{1-\alpha}{\sqrt{3}}\left(\sigma_\theta - \sigma_r\right). \tag{11}$$

With the help of the yield function, the relation of stresses in a plastic zone is solved by

$$\sigma_\theta = \frac{3Y + \left[\sqrt{3} - \alpha\left(\sqrt{3}-1\right)\right]}{\sqrt{3} - \alpha\left(2+\sqrt{3}\right)}\sigma_r\,. \tag{12}$$

Substituting Eq. (12) into the equilibrium Eq. (9), the stresses in the plastic zone are

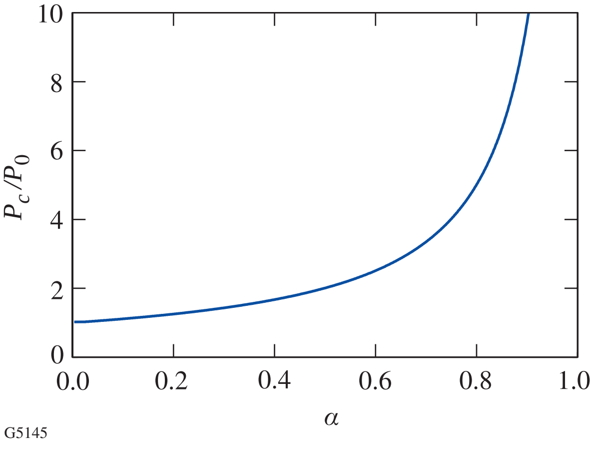

Figure 85.10
Initial yield pressure versus densification parameter. P_0 is the initial yield pressure without densification.

$$\sigma_r = -\frac{Y}{\alpha} + C\,r^{\frac{6\alpha}{\sqrt{3}-\left(2+\sqrt{3}\right)\alpha}},$$

$$\sigma_{\theta,\varphi} = -\frac{Y}{\alpha} + C\frac{\sqrt{3}-\left(\sqrt{3}-1\right)\alpha}{\sqrt{3}-\left(2+\sqrt{3}\right)\alpha}\,r^{\frac{6\alpha}{\sqrt{3}-\left(2+\sqrt{3}\right)\alpha}},\tag{13}$$

where C can be solved from the boundary condition at the cavity wall ($r = a$). At the plastic–elastic boundary ($r = b$), traction continuity gives

$$\left(\frac{b}{a}\right)^{\frac{6\alpha}{\left(2+\sqrt{3}\right)\alpha-\sqrt{3}}} = \frac{\sqrt{3}(1-\alpha)\left(1-\alpha\frac{P}{Y}\right)}{\sqrt{3}-\left(2+\sqrt{3}\right)\alpha}.\tag{14}$$

It can be easily verified that $b \geq a$ if and only if $P > P_c$.

For the cavity problem, the flow potential [Eq. (4)] is

$$g = -\alpha'\frac{\sigma_r+\sigma_\theta+\sigma_\varphi}{3} + \frac{1-\alpha'}{2\sqrt{3}}\left(\sigma_\theta-\sigma_r\right)$$

$$+\frac{1-\alpha'}{2\sqrt{3}}\left(\sigma_\varphi-\sigma_r\right).\tag{15}$$

By the flow theory $d\varepsilon_{ij}^p = d\lambda\partial g/\partial\sigma_{ij}$, we have

$$d\varepsilon_r^p = d\lambda\left(-\frac{\alpha'}{3}-\frac{1-\alpha'}{\sqrt{3}}\right),$$

$$d\varepsilon_\theta^p = d\lambda\left(-\frac{\alpha'}{3}+\frac{1-\alpha'}{2\sqrt{3}}\right),\tag{16}$$

$$d\varepsilon_\varphi^p = d\lambda\left(-\frac{\alpha'}{3}+\frac{1-\alpha'}{2\sqrt{3}}\right).$$

From the elastic theory, the elastic strain rate is

$$d\varepsilon_r^e = \frac{1}{E}\left(d\sigma_r - 2\nu d\sigma_\theta\right),$$

$$d\varepsilon_\theta^e = d\varepsilon_\varphi^e = \frac{1}{E}\left[-\nu d\sigma_r + (1-\nu)d\sigma_\theta\right].\tag{17}$$

The total strain rate contains both elastic and plastic parts: $d\varepsilon_{ij} = d\varepsilon_{ij}^e + d\varepsilon_{ij}^p$. By eliminating the $d\lambda$, we have

$$A'd\varepsilon_r + 2d\varepsilon_\theta = \frac{1}{E}\left\{\left(A'-2\nu\right)d\sigma_r + 2\left[1-\left(1+A'\right)\nu\right]d\sigma_\theta\right\},$$

$$A' = \frac{\sqrt{3}-\left(2+\sqrt{3}\right)\alpha'}{\sqrt{3}-\left(\sqrt{3}-1\right)\alpha'}.\tag{18}$$

Hill has solved this problem for the shear flow theory.[8] Following his method, the displacement increment can be written as

$$du(r,b) = \frac{\partial u}{\partial b}db + \frac{\partial u}{\partial r}dr = \left(\frac{\partial u}{\partial b} + v\frac{\partial u}{\partial r}\right)db,\tag{19}$$

where v is defined as the "velocity" of the particle. Defined in terms of the total displacement u and plastic–elastic boundary b,

$$v = \frac{\frac{\partial u}{\partial b}}{1-\frac{\partial u}{\partial r}}.\tag{20}$$

Written in terms of v and db, the nonzero stress and stain increments are

$$d\varepsilon_r = \frac{\partial}{\partial r}(du) = \frac{\partial v}{\partial r}db,$$

$$d\varepsilon_\theta = \frac{du}{r} = \frac{vdb}{r},$$

$$d\sigma_r = \left(\frac{\partial\sigma_r}{\partial b} + v\frac{\partial\sigma_r}{\partial r}\right)db,\tag{21}$$

$$d\sigma_\theta = \left(\frac{\partial\sigma_\theta}{\partial b} + v\frac{\partial\sigma_\theta}{\partial r}\right)db.$$

Substituting Eqs. (21) and (13) into (18), we have

$$A' \frac{\partial v}{\partial r} + \frac{2v}{r} = \frac{Y}{E} \frac{2\sqrt{3}}{1-\alpha} \left(\frac{b}{r}\right)^{\frac{6\alpha}{\left(2+\sqrt{3}\right)\alpha-\sqrt{3}}} \left(\frac{v}{r} - \frac{1}{b}\right)$$

$$\times \left[\left(A' + \frac{2}{A}\right) - \left(2 + 2\frac{A'}{A} + \frac{2}{A}\right) v\right], \tag{22}$$

$$A = \frac{\sqrt{3} - \left(2+\sqrt{3}\right)\alpha}{\sqrt{3} - \left(\sqrt{3}-1\right)\alpha}.$$

This is a first-order partial differential equation for v. By integrating Eq. (22) from the cavity wall ($r = a$) to the plastic–elastic boundary ($r = b$), the problem is solved. Equation (22) is coupled (via a, b) and subject to numerical integration. The fourth-order Runge–Kutta method is used to solve this equation. For verification, the problem is also solved by using the finite-element package Abaqus (Hibbitt, Karlssoon, & Sorensen, Inc.). The large deformation theory is used in the finite-element simulation.

Associated Flow Theory

For the associated flow theory, $\alpha = \alpha'$ and $A = A'$. The flow potential coincides with the yield surface. Perfect plastic deformation is also assumed. Pressure–expansion curves are shown in Fig. 85.11 from both the finite-element and numerical integration results. It is interesting that with the increase of α the material becomes "softer" for small α and "harder" for large α. It is also noticed that for small α, there is a pressure limit for cavity expansion, as expected for perfect-plastic material deformed with shear flow only. When the inner pressure is close to this limit, the cavity expands spontaneously. For large α, we do not see this pressure limit. The difference between finite-element and numerical integration results is due to the use of the finite deformation theory in the finite-element simulation.

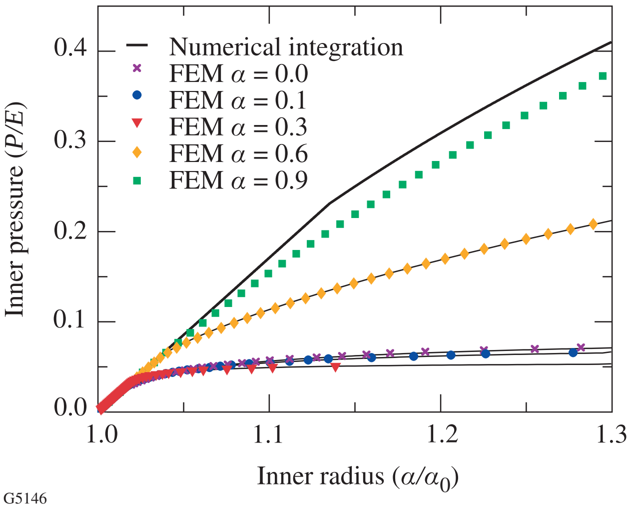

Figure 85.11
Cavity pressure–expansion curves for different α's.

The densification parameter α also affects the distribution of stresses at maximum load. The stresses at maximum load (1.45 P_c) are plotted in Figs. 85.12(a) and 85.12(b). For small α, the hoop stress is compressive; for large α, the hoop stress is tensile. We know that fracture under load is controlled by these stresses. For small α, if there is fracture under load, it happens under the surface; for large α, it will happen at the surface.

The residual stresses after 1.45 P_c loading are plotted in Figs. 85.12(c) and 85.12(d) for $\alpha = 0.3$ and 0.6. The densification parameter also affects the residual stresses. For small α, the surface layer is under compression; for large α, it is under tension. The layer with large residual stresses is thicker for small α. It needs to be mentioned that the initial yield pressure P_c will increase with α, so we expect, under the same load, even smaller residual stresses for large α. It is observed that fused silica has smaller residual stresses after grinding.[9] Figure 85.12(e) also compares the hoop stress under the same load for $\alpha = 0.1$, 0.3, and 0.6. At this load, only elastic deformation occurs for $\alpha = 0.6$.

Non-associated Flow Theory

For the non-associated flow theory, the material behavior is controlled by both yield function [Eq. (1)] and plastic potential [Eq. (4)]; now α is not equal to α'. Thus we have three material parameters (α, α', Y) to describe the plastic deformation. The reasonable combinations of α and α' should be investigated. It is not possible to have $\alpha = 1$ and $\alpha' = 0$, which means that the material yields with pressure but can be permanently deformed only with shear.

The integration of Eq. (22) has been carried out numerically for different combinations of α and α'. The results for $\alpha = 0.3$ and $\alpha = 0.6$ are shown in Fig. 85.13. When $\alpha = 0.3$, it is physically impossible for $\alpha' = 0.6$ and 0.9, which means that the cavity cannot decrease in size with an increase in inner pressure. For the same reason, α' cannot be 0.1 or 0.3 for $\alpha = 0.6$. From the analysis, we found the number separating these two regions to be around 0.46. These findings have been summarized in Fig. 85.14. For small α, α' must be small and vice versa.

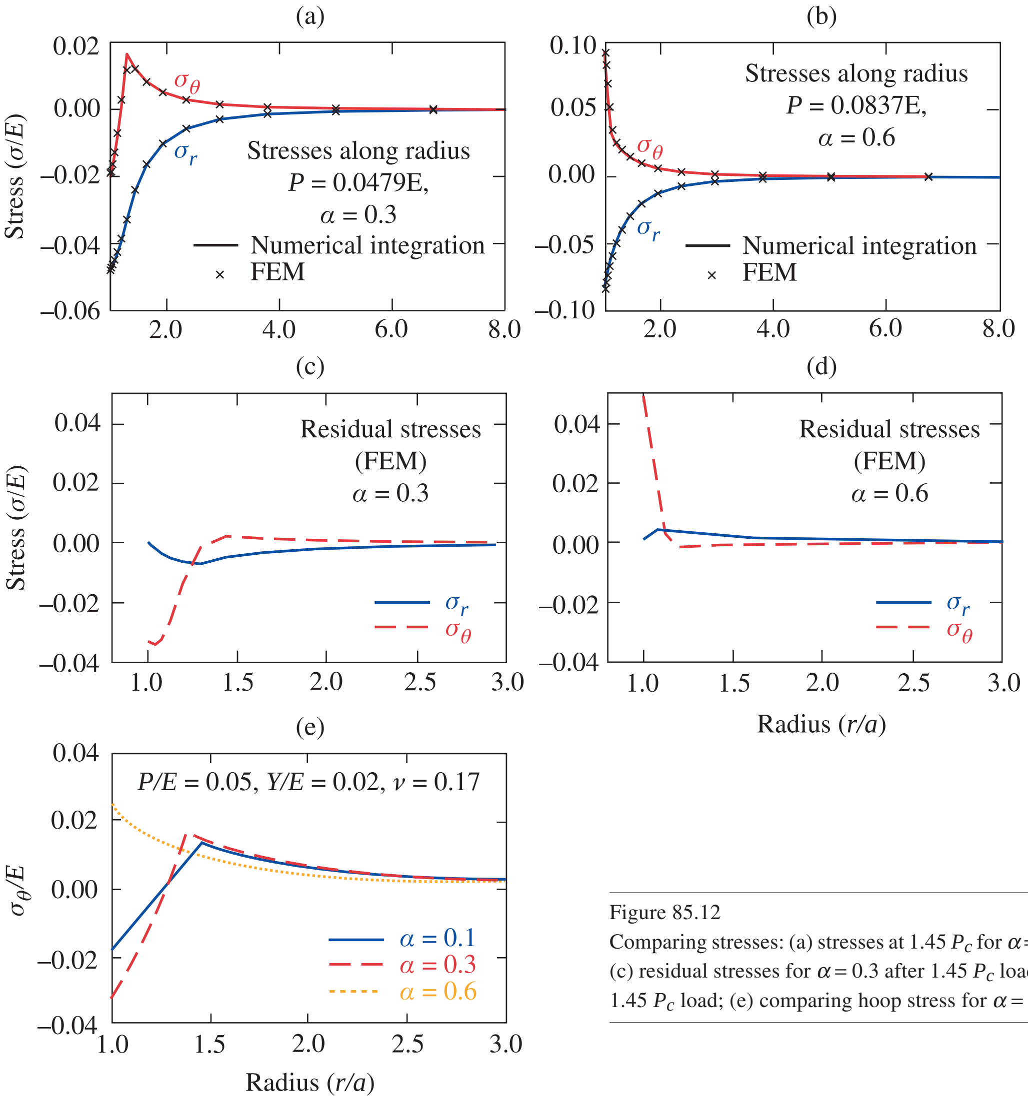

Figure 85.12
Comparing stresses: (a) stresses at 1.45 P_c for $\alpha = 0.3$; (b) stresses at 1.45 P_c for $\alpha = 0.6$; (c) residual stresses for $\alpha = 0.3$ after 1.45 P_c load; (d) residual stresses for $\alpha = 0.6$ after 1.45 P_c load; (e) comparing hoop stress for $\alpha = 0.1$, 0.3, and 0.6.

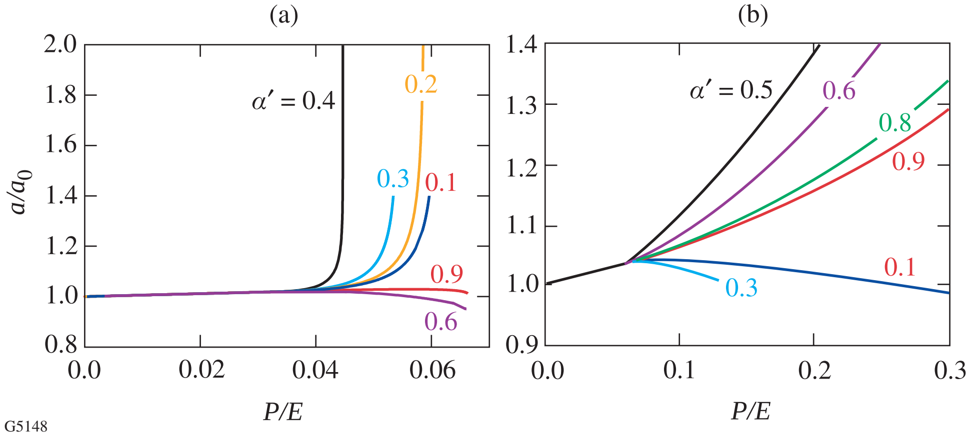

Figure 85.13
Pressure–expansion curves for non-associated flow theory: (a) $Y/E = 0.02$, $\alpha = 0.3$; (b) $Y/E = 0.02$, $\alpha = 0.6$.

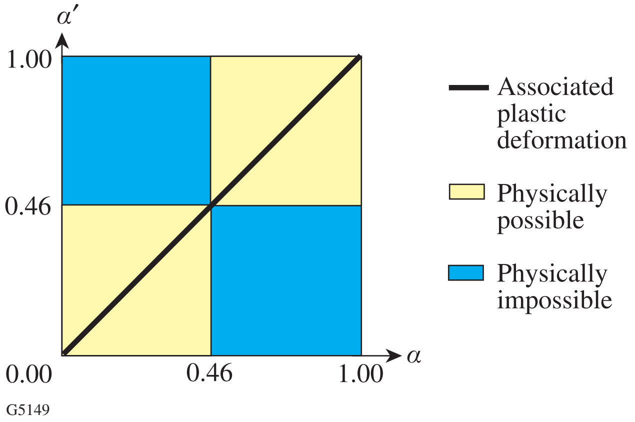

Figure 85.14
Material possibility map.

Figure 85.13(a) shows the pressure expansion curves for small α and α'. As observed in the associated theory, there is a pressure limit for spontaneous growth. For small α, with the increase of α', the limit pressure decreases, which means that the material becomes "softer." The spontaneous growth pressure is not observed for large α and α' [see Fig. 85.13(b)]. We also noticed that, for large α, the material becomes "harder" with the increase of α'.

Conclusion

The cavity problem has been studied by using a new material model. Both associated and non-associated flow theories have been examined. For the associated case, $\alpha = \alpha'$ and plastic potential is coincident with yield surface. We have two material parameters (α, Y) to describe plastic deformation with densification. The initial yield pressure increases with α. When α is small (small densification), there is a small softening with the increase of α. The cavity can grow spontaneously when the inner pressure reaches a limit. When α is large (large densification), there is a remarkable strengthening with the increase of α. The spontaneous cavity growth is not observed. The densification affects stress distributions at loading. When the densification parameter α is small, the hoop stress under load is compressive, similar to the material flowing without densification. When α is large, the hoop stress under load is tensile. The residual stresses are also affected by densification. For small densification, the surface residual stress is compressive; it is tensile for large densification.

For the non-associated case, the plastic behavior is described by three material parameters: α, α', Y. By investigating the non-associated case, we found that there are physically impossible combinations for α and α'. It is necessary to keep both α and α' small (<0.46) or large (>0.46). The increase of α' causes softening for small α and hardening for large α.

REFERENCES

1. P. W. Bridgman and I. Simon, J. Appl. Phys. **24**, 405 (1953).
2. R. Roy and H. M. Cohen, Nature **190**, 789 (1961).
3. E. B. Christiansen, S. S. Kistler, and W. B. Gogarty, J. Am. Ceram. Soc. **45**, 172 (1962).
4. J. D. Mackenzie, J. Am. Ceram. Soc. **46**, 461 (1963).
5. J. S. Tse, D. D. Klug, and Y. Le Page, Phys. Rev. B **46**, 5933 (1992).
6. J. C. Lambropoulos, S. Xu, and T. Fang, J. Am. Ceram. Soc. **79**, 1441 (1996).
7. A. B. Shorey, K. Xin, K.-H. Chen, and J. C. Lambropoulos, in *Inorganic Optical Materials*, edited by A. J. Marker III (SPIE, Bellingham, WA, 1998), Vol. 3424, pp. 72–81.
8. R. Hill, *The Mathematical Theory of Plasticity* (Clarendon Press, Oxford, 1950).
9. J. C. Lambropoulos, S. Xu, T. Fang, and D. Golini, Appl. Opt. **35**, 5704 (1996).

Design and Performance of a Selectable-Rate Streak-Camera Deflection Ramp Generator

Introduction

Electro-optic streak cameras have been used at LLE for many years to resolve high-bandwidth, low-repetition-rate, pulsed laser phenomena. Until now the sweep rate was governed by a fixed-rate voltage ramp generator used to drive the sweep deflection plates.

Altering the time base required physically changing the ramp generator. In this article a new method of generating the sweep deflection ramps is presented that permits changing the sweep rate by computer control without replacing the ramp generator. A logic level signal can now be used to change sweep rates without the need for invasive component changes. This new development permits fast and easy sweep rate changes for streak cameras in any location throughout the laboratory, especially in low accessibility locations such as clean rooms and high-power-laser environments.

As a result of this work, a 50-Ω matched-impedance voltage ramp generator was developed. The matched-impedance design of the generator allows the deflection signals to propagate on standard 50-Ω coaxial cable without distortion of the ramp waveform regardless of cable length. The ramp generator's location and interconnect length to the deflection plates are less restricted than with the previous design. In situations where access to the streak camera's tube deflection electrodes is limited by space or environmental constraints, this feature can be a great asset.

The first production circuit has been installed in an infrared-sensitive streak camera, and tests have been performed to measure sweep rate and linearity. The infrared camera contains a Phillips P510 streak tube[1] coupled to a 512 × 512-pixel CCD. The circuit is designed with four selectable sweep ramp rates, which produce voltage ramps of ±1000 V in 2, 6, 10, and 20 ns. Measured results agree well with design modeling.

Background

The LLE streak camera used for this work contains two deflection plates that are differentially driven by two equal but opposite-polarity voltage ramp signals. Throughout this discussion only one of the ramp generators will be described. It is assumed that the other ramp generator uses the same technology and produces the same result with the opposite-polarity voltage.

The original streak-camera ramp generator designs at LLE were based on a resistor, inductor, capacitor (RLC) resonator.[2] The resonator, when driven by a voltage-step waveform, produced a damped sinusoidal response. The voltage step was produced by switching a fast avalanche transistor stack. Proper selection of the resonant frequency (the frequency where the capacitive reactance equals the inductive reactance) and the resistive damping factor produced a voltage ramp with the desired sweep slope. Closed-form expressions and computer simulations were developed to determine the required values of the resonator components for a specified sweep ramp. The basic circuit configuration is illustrated in Fig. 85.15.

The RLC ramp generator had several shortcomings: In the RLC circuit the values of the rate-determining reactances are small enough that parasitic reactances, such as those introduced by elecromechanical relay contacts and deflection-plate feed lines, can greatly affect the sweep ramp characteristics. For this reason a selectable-rate ramp generator could not be

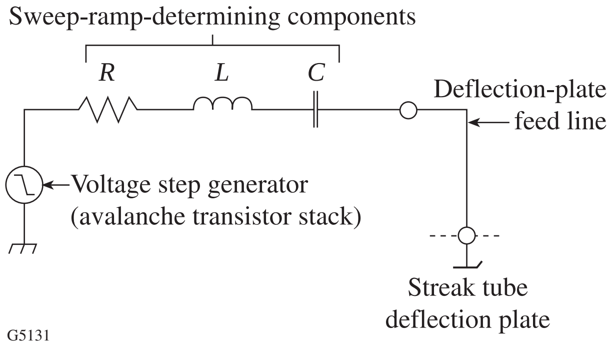

Figure 85.15
Original RLC resonator streak-camera ramp generator design.

designed using the RLC circuit configuration. To change ramp rates, removal and replacement of the RLC ramp generator module was required. For many this limitation was both time consuming and inconvenient.

Another disadvantage of the RLC resonator approach was that the feed line between the ramp generator and the deflection plate connection forms part of the RLC resonant circuit. A feed line that is too long or physically positioned improperly will distort the ramp shape significantly. As a result the ramp generator had to be mounted as close as physically possible to the streak tube deflection plate connections. In streak cameras where space around the tube deflection plate connections is limited, this complicates the overall design of the instrument.

The limitations of the RLC base ramp were overcome by a new sweep ramp generator design. The new design is a matched low-impedance ramp generator. With the low-impedance design, small shunt impedance parasitics, such as relay capacitance and feed line parasitics, have a negligible effect on the sweep ramp shape. Matching the impedance of the generator to the load removes the problems associated with the feed lines. Theoretically, the input impedance of an ideal transmission line terminated in its characteristic impedance is equal to the characteristic impedance regardless of line length. Thus the matched impedance ramp generator will produce the same waveform regardless of the interconnection length between the generator and the deflection plates as long as the generator, cable, and termination are of matched impedance.

The step generator needed for the matched-impedance ramp generator must be able to withstand higher switching current than the step generator for the RLC resonator. An avalanche transistor stack alone will not withstand the step current for a long enough duration when driving a 50-Ω load.[3] The step current duration must be long enough to maintain the step voltage at a specific potential following the active portion of the sweep to avoid retrace problems prior to camera shutter closure. In addition a matched generator and load will divide the switching potential, one half across the step generator internal impedance with the other half developed across the load. For a matched generator a higher voltage step is required to produce the same ramp voltage as developed by the RLC resonator approach.

Multi-rate Network

The block diagram of the selectable-rate streak-camera deflection ramp generator is illustrated in Fig. 85.16. The first production ramp generator module is shown in Fig. 85.17. The basic parts of the generator are the matched-impedance (50 Ω) voltage step generator and the filter network that determines the sweep rate.

Details of the low-pass-filter network are illustrated in Fig. 85.18. There are four individual electromechanical relay-selectable, low-pass filters. A remote-control logic interface within the filter network controls the relays. Each filter limits the high-frequency spectral components produced by the step generator, which in turn produces an output sweep ramp at a slower rate. Selection of the low-pass-filter cutoff frequency f_c determines the produced slope of the ramp. Each filter consists of a three-section inductor/capacitor (LC) passive low-pass circuit. With four filters the generator is capable of four different sweep rates. A fifth filter is included in series with the

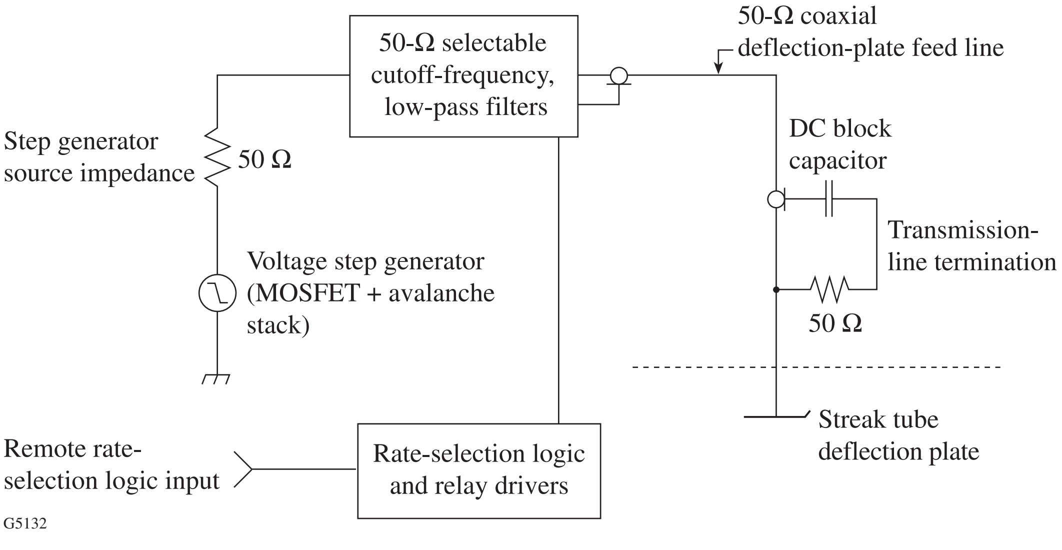

Figure 85.16
Block diagram of a new selectable-rate streak-camera deflection ramp generator.

selectable filters to limit high-frequency-signal leakage through the four selectable low-pass filters. The cutoff frequency of the fifth filter is set higher than the other filters so their passband performance is not affected.

Each 50-Ω matched-impedance low-pass filter is based on the coefficients that produce a Butterworth characteristic.[4] A Butterworth low-pass filter produces monotonically increasing attenuation with increasing frequency. Closed-form equations are well known relating the component values to the one-half-power, or 3-dB, cutoff frequency f_c. Equations (1) through (3) provide the formulas required to calculate the component values for the three-section 50-Ω filters:

$$\omega_c = 2\pi f_c \qquad (1)$$
$$\left(\text{low-pass cutoff radian frequency, rad/s}\right)$$

$$L = 2Z/\omega_c \quad (\text{henrys}), \qquad (2)$$

$$C = 1/(\omega_c Z) \quad (\text{farads}), \qquad (3)$$

where $Z = 50\ \Omega$ is the impedance of the filter.

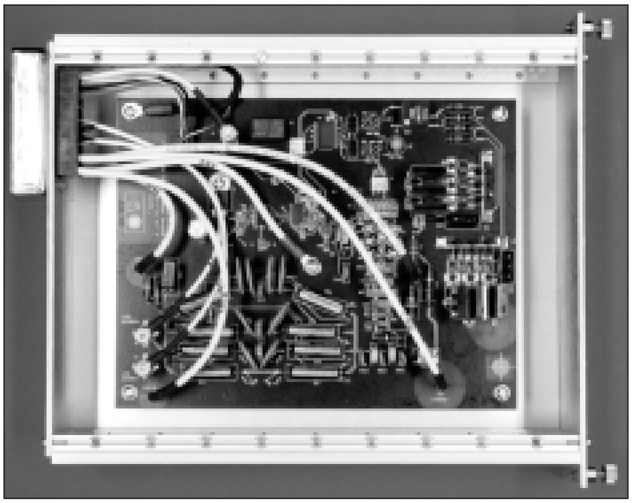
G5133

Figure 85.17
Photograph of the selectable-rate streak-camera deflection ramp generator module. The top side of the board (shown) contains the negative-slope ramp generator, rate-selection logic, and relay drivers. The opposite side of the board (not shown) contains the positive-slope ramp generator.

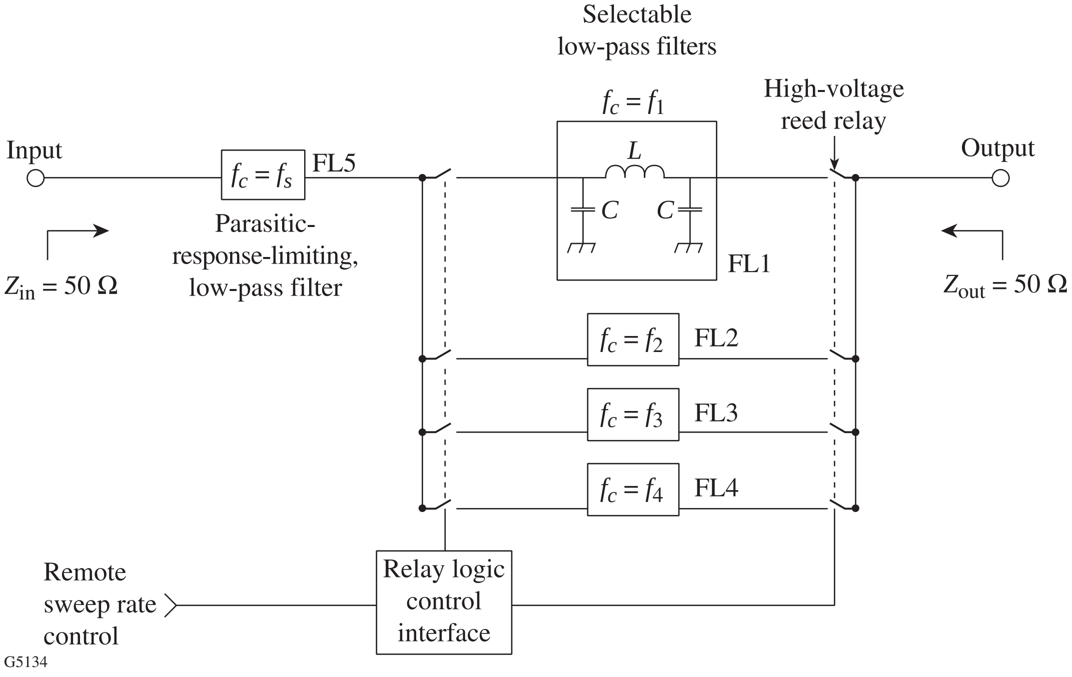

Figure 85.18
Block diagram of the 50-Ω selectable cutoff low-pass filters that determine the sweep ramp rate.

A SPICE[5] computer circuit simulation that includes the low-pass filters was developed for the ramp generator. A simplified schematic of the circuit model is shown in Fig. 85.19. Filters with low-pass cutoff frequencies from 1 to 155 MHz were evaluated using the circuit model to determine their effect on the ramp slope. Two parameters are used to relate the effect of the low-pass filter to the ramp slope. The first parameter t_r is the time required for the voltage ramp to change by 1000 V over its most linear portion. This is the region of the ramp generator's output waveform that produces the sweep deflection over the active region of the streak tube's output window. The second parameter K_f is the product of t_r with the low-pass cutoff frequency f_c. This product is the ratio of the ramp time to the period of the low-pass cutoff frequency. Knowing K_f, the low-pass cutoff frequency can be calculated for a specific active ramp duration t_r using

$$f_c = K_f / t_r \, . \tag{4}$$

Figure 85.20 illustrates the relation between the active sweep ramp time t_r and the constant K_f, as determined through computer modeling. Rearranging and substituting terms from Eq. (4) in Eqs. (2) and (3) leads to the following equations that are needed to determine the values of the low-pass filter components from the value of t_r and K_f:

$$L = \left(2Zt_r\right) \Big/ \left(2\pi K_f\right) \ \text{(henries)}, \tag{5}$$

$$C = t_r \Big/ \left(2\pi K_f Z\right) \ \text{(farads)}, \tag{6}$$

where t_r = active ramp duration in seconds.

In an ideal step generator the step transition occurs instantaneously. For any practical step generator the step transition is of finite duration. In the SPICE circuit simulation the transition rate for the step generator was chosen to be 0.33 ns/kV. Typically an avalanche transistor stack can produce this ramp rate; however, as stated previously, the avalanche stack cannot

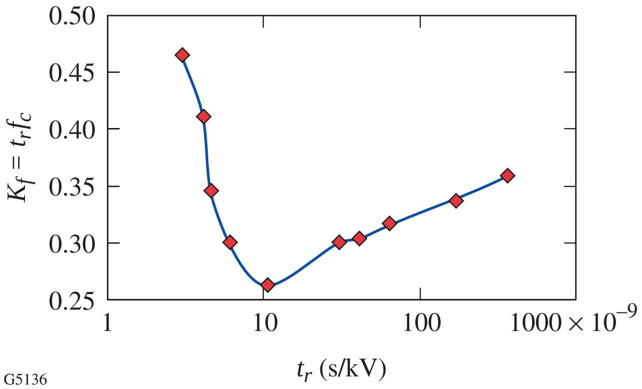

Figure 85.20
Plot of frequency product constant K_f as a function of sweep time t_r. Results produced by SPICE circuit simulation of the selectable-rate ramp generator.

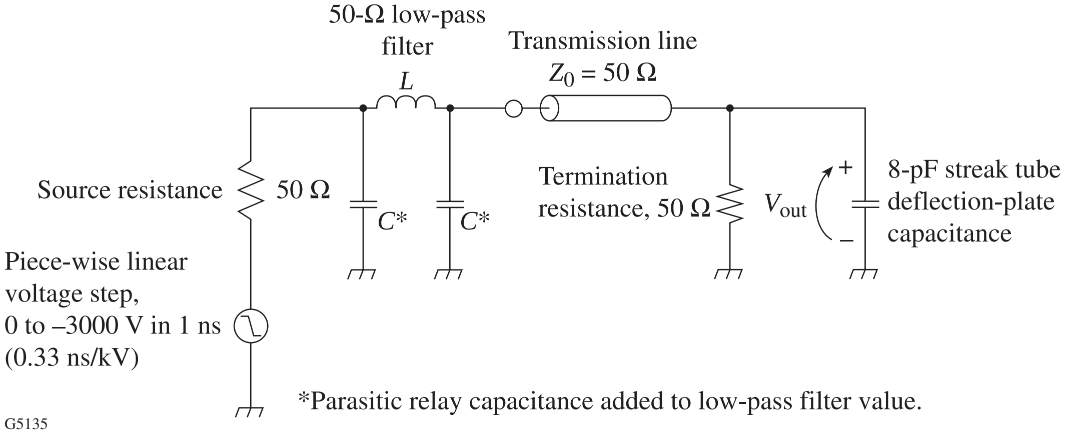

Figure 85.19
Simplified schematic of the SPICE circuit simulation model used to determine a correlation between low-pass-filter cutoff frequency and sweep ramp rate. Actual circuit model contains detailed relay, step generator, and component parasitic models.

withstand the 30-A switching current for a duration of several microseconds as required for a matched 50-Ω step generator.[3] High-voltage MOSFET's (metal-oxide silicon field effect transistors) can support a 50-Ω step generator switching current and voltage but cannot provide a transition rate of 0.33 ns/kV. Typical MOSFET switching speeds are of the order of 3.3 ns/kV. Combining the two switch technologies in parallel provides both the speed and durability required for the 50-Ω step generator by utilizing the speed of the avalanche transistor switch and the current-handling capabilities of the MOSFET switch. The avalanche transistor switch is triggered first, followed by the MOSFET switch after a short delay. This step generator is illustrated in Fig. 85.21.

The avalanche transistor stack follows a design using a tapered transmission line–matching technique developed at Lawrence Livermore National Laboratory.[6] This technique uses the internal self-inductance of the avalanche transistors combined with added collector-to-ground capacitance chosen to effectively create a transmission line that tapers from a low impedance of several ohms at the bottom to 50 Ω at the top of the stack. An avalanche stack designed in this manner produces a faster switching rate into 50 Ω than a conventionally designed stack where impedance matching is not included. The tapered transmission line stack is capable of driving a 50-Ω load for short periods (50 ns) with a typical rise time of 0.33 ns/kV. To limit the switching current duration in the avalanche stack, a capacitance of 220 pF is connected in series with the 50-Ω load. Well before the avalanche transistors are stressed, the series capacitor discharges and reduces the avalanche stack current.

The MOSFET switch is designed to have a switching rate of 3.3 ns/kV with an output matched to 50 Ω through the use of a series resistor. The MOSFET stack has a lower on-state resistance than 50 Ω, and the series resistor raises it up to the desired level. This switch is connected in parallel with the avalanche transistor stack. The MOSFET switch is triggered immediately after the avalanche transistor stack and is fully on before the avalanche stack series current-limiting capacitor is discharged. Thus the avalanche transistor stack provides the leading edge of the voltage step, and the MOSFET stack provides the step-holding time to prevent streak camera retrace and avalanche stack degradation. The source impedance of the composite switch is 50 Ω except for the time interval between the MOSFET switch turn-on and when the avalanche transistor stack series capacitor is fully discharged. This does not produce a measurable effect on the output since any mismatch reflection is terminated at the deflection plate termination and not re-reflected. The composite switch waveform is illustrated in Fig. 85.22.

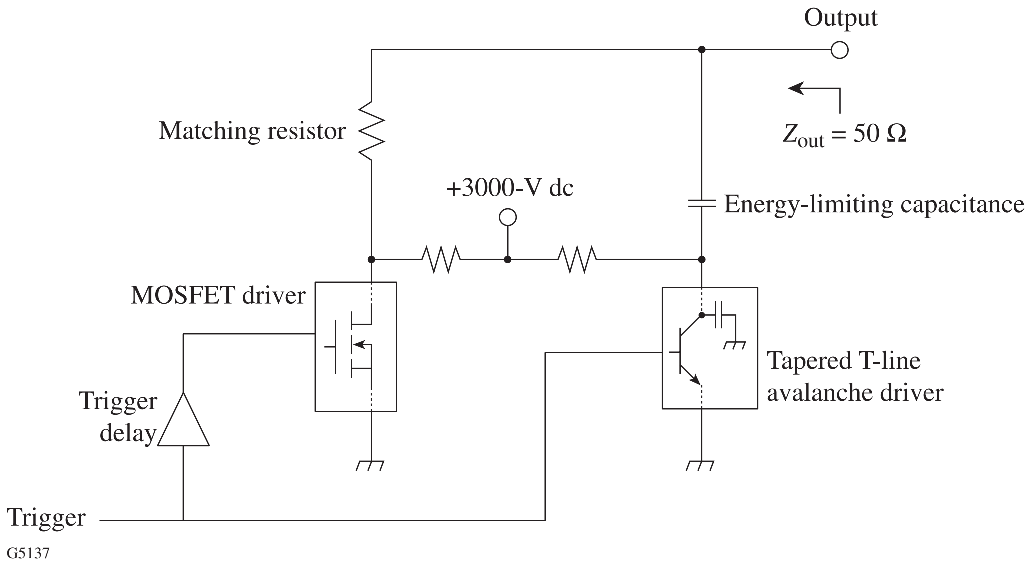

Figure 85.21
Block diagram of the 3000-V composite avalanche transistor stack and MOSFET step generator. The MOSFET driver contains three series-connected, simultaneously triggered 1200-V MOSFET's. The avalanche transistor stack is a ten-level transistor stack designed using the tapered transmission line technique developed at Lawrence Livermore National Laboratory.[6]

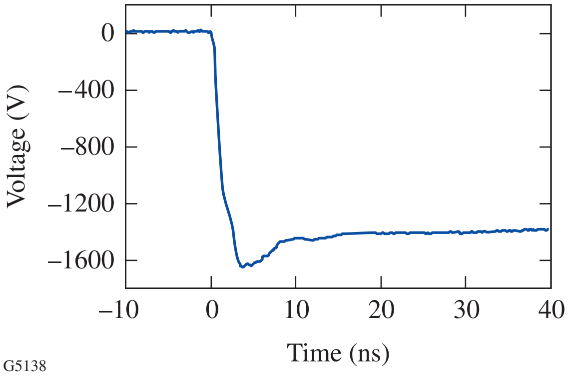

Figure 85.22
Measured output waveform produced by the composite avalanche transistor and MOSFET step generator. Fall time of step is 1 ns/kV.

The composite switch and selectable filter network form the selectable-rate ramp generator. A positive- and negative-voltage pair of these generators are needed to produce a complete differential deflection-plate generator. A 50-Ω transmission line is used to connect the ramp generator to the deflection plates. A matched 50-Ω termination is connected at the deflection-plate end of the transmission line.

Measured Electrical Performance

The electrical performance of the selectable-rate ramp generator is summarized in Figs. 85.23 and 85.24 and Table 85.I. In Fig. 85.23 all four sweep waveforms are superimposed. In Table 85.I the design parameters are listed with the measured results for each of the four sweep rates. The measured data for Fig. 85.23 and Table 85.I were recorded using a high-bandwidth oscilloscope[7] and a high-voltage, high-bandwidth probe[8] connected to the deflection plate of the streak tube. In Fig. 85.24 the measured and desired sweep rates for the four different selectable speeds are compared.

The differences between the desired and measured sweep rates indicate that more refinement of the filter factor K_f must be performed to get a closer correlation between the calculated and measured sweep rates. With an accurate K_f factor any reasonable sweep rate can be defined, and the appropriate low-pass filter can be designed using Eqs. (5) and (6). Errors in K_f are generated by incomplete modeling of the actual circuit parasitics in the SPICE computer simulation model for the ramp generator and by non-ideal characteristics of the composite voltage step generator. Since the measured sweep rates may be faster or slower than the desired rates, it should be possible to determine K_f to a high degree of accuracy with more-accurate computer circuit simulations.

Measurements of the sweep-speed nonlinearity indicate that the deflection rate slope is not uniform across the active sweep. Figure 85.25 illustrates the nonuniformity in the ramp slope for a sweep rate of 4.4 ps/pixel. The sweep rate is generally slow on the edges of the sweep and fast in the center. The measured sweep waveform has a sinusoidal characteristic instead of being a linear ramp. This nonlinearity is produced by the limited summation of sinusoids as theoretically generated by a step response propagated through a low-pass filter. The nonlinearity is reproducible with respect to the sweep waveform timing and should be removable when processing the streak image data. Increasing the ramp generator voltage swing

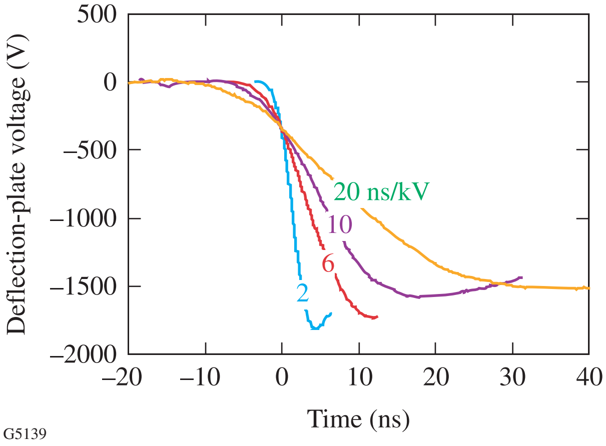

Figure 85.23
Measured output waveforms from the selectable-rate deflection ramp generator. The sweep waveforms for the four different ramp rates are superimposed.

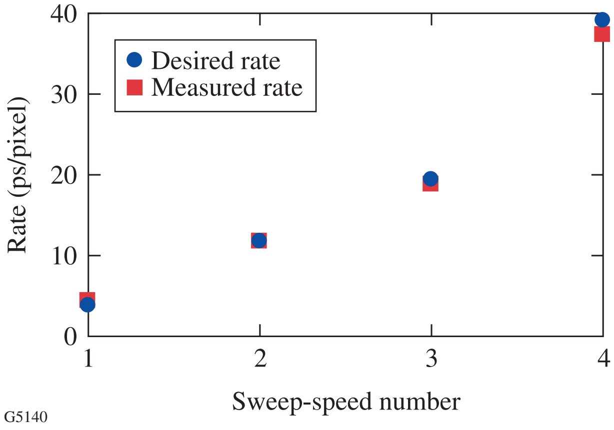

Figure 85.24
Comparison of desired and measured sweep rates.

would reduce the nonlinearity. This would place the active portion of the ramp generator output in an area of the waveform where the slope is more constant. The improved linearity must be traded off with increased complexity of the step generator and low-pass filter networks to accommodate the increased voltages and currents.

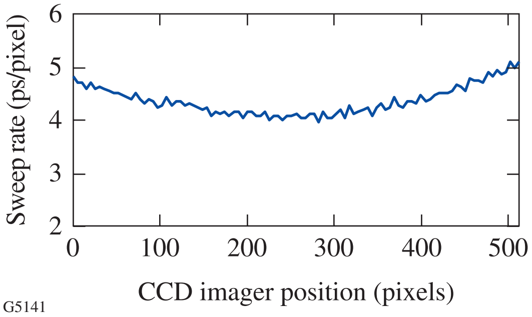

Figure 85.25
Measured sweep rate versus position on the CCD for a 4.4 ps/pixel sweep rate.

Optical Characterization of the Ramp Generator

A selectable-rate ramp generator was installed in a streak camera and characterized at a designed ramp rate of 17 ps/pixel using a 4.5-ns optical comb pulse.[9] The measurement setup (Fig. 85.26) shows the streak camera input illuminated with the comb pulse and the streak camera's deflection plate ramp generator triggered from a timing system synchronized with the comb pulse. Since the duration of the comb pulse is less than the sweep time of the ramp generator, the time delay between the ramp generator trigger and the arrival of the comb pulse at the streak camera was varied in order to scan the comb pulse over the full sweep duration. A series of streaks were recorded while changing this delay. The streak camera's sweep speed was characterized by using the constant time interval between each pair of adjacent peaks within the comb pulse to determine the average sweep dwell time at the center CCD pixel location (Fig. 85.27). By analyzing the acquired streaks of the comb pulse the streak camera's sweep speed as a function of deflection position, in this case CCD pixel position, was determined and compared to the measurement made by the

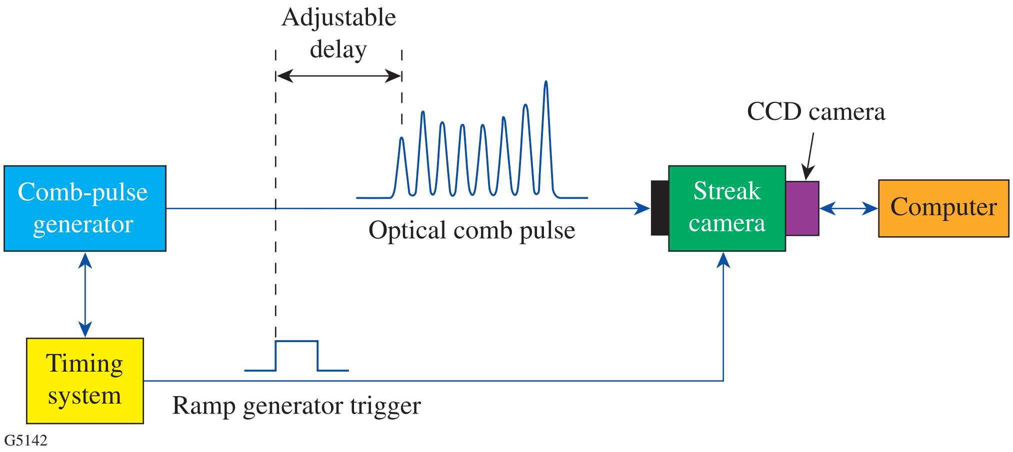

Figure 85.26
The streak camera is illuminated with a 4.5-ns-duration comb pulse, and the deflection-plate ramp generator is triggered from a timing system with an adjustable delay relative to the comb pulse.

Table 85.I: Measured and simulated result comparison for the ramp generator.

Full-Width Sweep Time t_r (ns)	Desired Rate (ps/pixel)	Filter Factor K_f	Theoretical Filter f_c (MHz)	Actual Filter f_c (MHz)	Measured Average Rate (ps/pixel)	Measured Rate Deviations from Average (ps/pixel)	
						min	max
2	3.9	0.47	235.0	155.0	4.4	–0.5	0.3
6	11.7	0.30	50.7	50.8	11.6	–1.7	1.1
10	19.5	0.26	26.0	29.3	18.9	–3.6	3.1
20	39.1	0.29	14.5	15.6	37.5	–8.8	7.3

electrical technique discussed earlier (Fig. 85.28). The spacing between the peaks of the comb pulse limits how close to the beginning and end of a streak the sweep speed can be reliably characterized because two adjacent peaks are required to determine the sweep speed at the point midway between them. We have found that for different ramp-rate selections, the electrical characterization of the ramp generator agrees well enough with the optical characterization to allow the initial setup to be done electrically and then perform the final optical characterization using the comb pulse. This will expedite the building and testing of new ramp generators while maintaining the availability of the streak cameras for use with experiments on OMEGA.

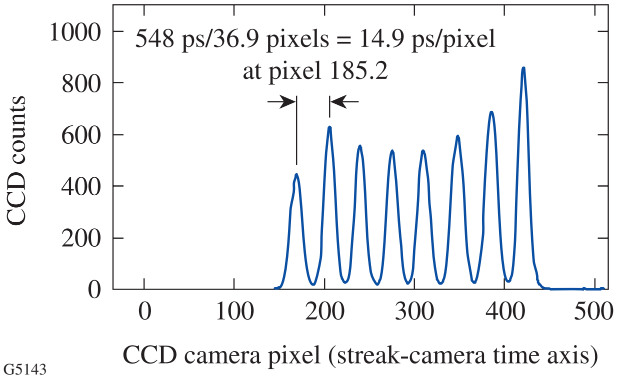

Figure 85.27
The constant time interval between each pair of adjacent peaks within the comb pulse is used to determine the sweep dwell time at the CCD pixel location midway between the peaks.

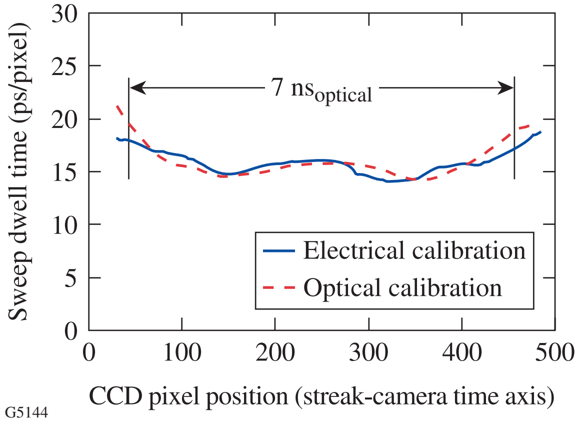

Figure 85.28
The optical and electrical measurements of the ramp generator agree well enough to allow the initial setup to be done electrically and then to perform the final optical characterization using the comb pulse.

Conclusion

A new method of generating streak-camera deflection ramps utilizing a 50-Ω composite MOSFET/avalanche transistor step generator and a relay-selectable low-pass-filter network was presented. This new design allows remote selection of four different sweep rates and provides a 50-Ω interface to the streak tube deflection plates. The 50-Ω interface relieves the requirement of mounting the ramp generator in close proximity to the deflection plates since the deflection signal can propagate along any length of standard 50-Ω coaxial cable.

There is good agreement between the modeled and measured sweep rates. The observed differences can be reduced by incorporating a more detailed computer-aided simulation model that accounts for all non-ideal component behavior. The nonlinearity in the ramp rate is reproducible and can be corrected in the data analysis.

ACKNOWLEDGMENT

This work was supported by the U.S. Department of Energy Office of Inertial Confinement Fusion under Cooperative Agreement No. DE-FC03-92SF19460, the University of Rochester, and the New York State Energy Research and Development Authority. The support of DOE does not constitute an endorsement by DOE of the views expressed in this article.

REFERENCES

1. P510PSU streak tube, Philips Photonics, Slatersville, RI 02876.
2. Laboratory for Laser Energetics LLE Review **73**, 6, NTIS document No. DOE/SF/19460-212 (1997). Copies may be obtained from the National Technical Information Service, Springfield, VA 22161.
3. Zetex, Inc., Commack, NY 11725.
4. E. C. Jordan, *Reference Data for Engineers: Radio, Electronics, Computer, and Communications*, 7th ed. (H. W. Sams, Indianapolis, IN, 1985), pp. 9-14, 9-19.
5. SPICE 3F.2, developed by the Department of Electrical Engineering and Computer Sciences, University of California, Berkeley, CA 94720.
6. E. S. Fulkerson and R. Booth, Lawrence Livermore National Laboratory, Livermore, CA, UCRL-JC-116309 (1994).
7. Oscilloscope Model No. TDS684, Tektronix Corporation, Beaverton, OR 97077.
8. Oscilloscope Probe Model No. P5100, Tektronix, Inc., Wilsonville, OR 97070.
9. Laboratory for Laser Energetics LLE Review **72**, 184, NTIS document No. DOE/SF/19460-199 (1997). Copies may be obtained from the National Technical Information Service, Springfield, VA 22161.

Unique High-Bandwidth, UV Fiber Delivery System for OMEGA Diagnostics Applications

Introduction

The OMEGA laser at the Laboratory for Laser Energetics was built for direct-drive inertial confinement fusion (ICF) experiments.[1] Sixty symmetrically disposed laser beams are used to compress ICF capsules that typically contain deuterium–tritium (DT) or deuterium. The laser beams heat and compress the target, causing the fuel to undergo thermonuclear fusion. Special temporally shaped pulses, which typically have a 1- to 3-ns duration, must be generated to optimize the target compression. To avoid hydrodynamic instabilities during the target compression the target illumination must be highly uniform.[2] This requires good power balance of all 60 OMEGA beams. The characteristic time of the hydrodynamic instability seed is under 100 ps, which means that the laser drive must be uniform on a 100-ps time scale. This defines the time scale over which power balance must be achieved.[3]

To measure the UV pulse shape and OMEGA power imbalance (see Fig. 85.29), we developed a ten-channel streak camera based on a commercial P510 streak tube.[4] Six such cameras are used to measure the pulse shape in the 60 OMEGA beams.

Motivation

High fusion neutron yield produced during OMEGA target shots causes excessive noise in the streak camera's charge-coupled devices (CCD's), significantly reducing the camera's dynamic range. The neutron-induced noise could be reduced by placing the cameras behind the Target Bay's shield wall. This required the development of a longer fiber optic system to deliver light from the sampling point to the streak camera input.

The most important parameters of the optical fiber to be used in this delivery system are high transmission at the OMEGA working wavelength (351 nm) and low modal dispersion. We require ~15-m-long fibers, so we set our attenuation requirement to ≤220 dB/km at 351 nm. The modal dispersion must be low enough to allow an overall bandwidth of the streak camera diagnostic to be ≥30 GHz.

To assure pulse-shape fidelity of the frequency-modulated and wavelength-dispersed laser pulse,[5] a speckle pattern is launched into the fibers, which is matched to the multimode

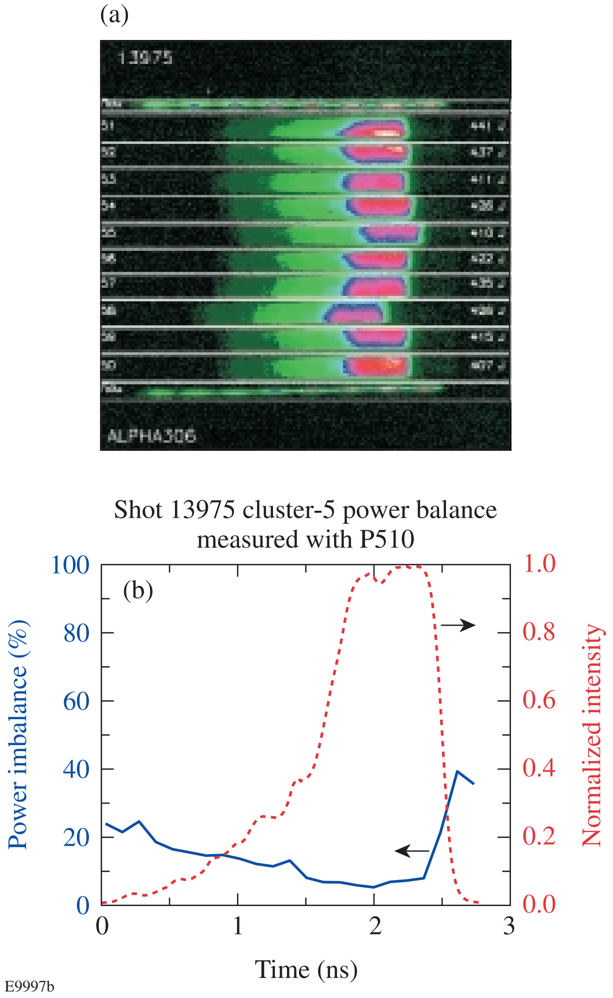

Figure 85.29
P510 streak cameras provide pulse-shape and power-imbalance measurements for all 60 beams of OMEGA. (a) Streak camera recording of all ten beams in one OMEGA cluster. (b) P510 streak camera average pulse shape for all ten beams of cluster 5 on shot 13975 (dashed line) and beam-to-beam power imbalance (solid line) determined from the streak records.

pattern of the fiber. The statistics are further improved by launching into a bundle of seven fibers (Fig. 85.30). To increase the fiber bundle's light-launching efficiency, the ratio of the cladding diameter to the core diameter (clad/core ratio) should be close to 1.

Assembling fiber bundles requires high precision in matching individual fiber lengths. Unequal fiber lengths will reduce the bandwidth of the optical fiber delivery system.

Optical Fiber Manufacturing

Optical fibers were made using the modified chemical vapor deposition (MCVD) method.[6] The 13-mm-diam preforms used consisted of a P_2O_5 doped silica core and a pure silica glass cladding; initial clad/core ratio was 2. Before fiber drawing, the preforms were etched in hydrofluoric acid (HF) to achieve a clad/core ratio of 1.25. The MCVD method ensured the required graded index profile and low dispersion at the working wavelength. Figure 85.31(a) shows the preform's index-of-refraction profile. The central dip in this profile is due to vaporization of P_2O_5 while the preform collapses under high temperature during the preform manufacturing process. While this dip cannot be removed completely, it can be minimized. The presence of the dip did not affect fiber performance. The optical fibers were drawn from preforms and covered in line with an epoxyacrylate coating using a pressurized die. The fibers have a core diameter of 100 μm, a cladding diameter of 125 μm, and a coating diameter of 250 μm. The typical fiber attenuation dispersion curve in Fig. 85.31(b) demonstrates that the optical fiber satisfies the <220-dB/km attenuation requirement at OMEGA's working wavelength.

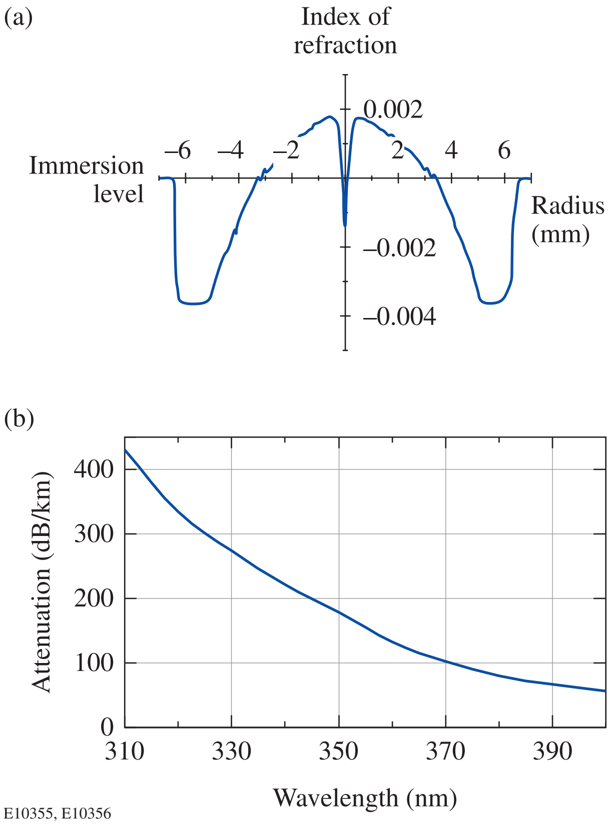

Figure 85.31
(a) Index-of-refraction profile for the fiber preform and (b) the fiber attenuation dispersion curve.

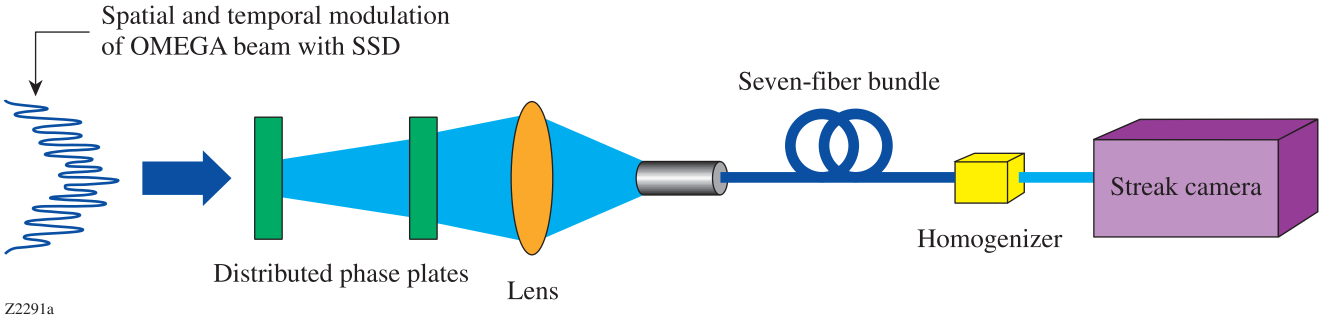

Figure 85.30
Schematic of optical UV fiber delivery system that was designed to sample the OMEGA laser beam and bring the light to the streak camera.

Laser System with Pulse Compression for Fiber Testing

To test the optical fiber and fiber bundle bandwidth, a laser system similar to that described in Ref. 7 was used; it produced 20-ps synchronizable laser pulses at 337-nm wavelength at a ≤10-Hz repetition rate. A block diagram of the laser system is shown in Fig.85.32. Starting with the *Q*-switched Nd:YLF monomode laser, a 10-ns square pulse with ~10-μJ energy was sliced out. After amplification, this pulse was directed to a stimulated Brillouin scattering (SBS) cell filled with CCl_4. By choosing the right focusing geometry and input energy, the incoming 10-ns pulse was compressed to ~360 ps with more than 50% energy efficiency. After second-harmonic conversion the 527-nm pulse was further compressed to ~20 ps using a pressurized-hydrogen, stimulated Raman scattering (SRS) cell (frequency shift is 4156 cm^{-1}). The energy of the SRS 674-nm pulse was >2 mJ; another second-harmonic conversion resulted in a ~20-ps, 337-nm, >0.5-mJ externally synchronizable pulse. The timing jitter of this pulse was measured to be ~150-ps rms. The SBS pulse compression mechanism is the source of this timing jitter. The focused-laser-beam Rayleigh range inside the SBS cell defines the jitter of the compressed pulse because the compression process may start at any point within the Rayleigh range.

A streak camera was used to measure the single-fiber modal dispersion. Single-shot measurements were made, recording the pulse width after its propagation through a 40-m piece of optical fiber compared to propagation through air. The optical-fiber modal dispersion was calculated using the following relationship:

$$\Delta t = \sqrt{(t_{\text{out}})^2 - (t_{\text{in}})^2} \Big/ L_{\text{fiber}} \,,$$

where Δt is the modal dispersion, t_{in} is the fiber input-pulse width, t_{out} is the fiber output-pulse width, and L_{fiber} is the

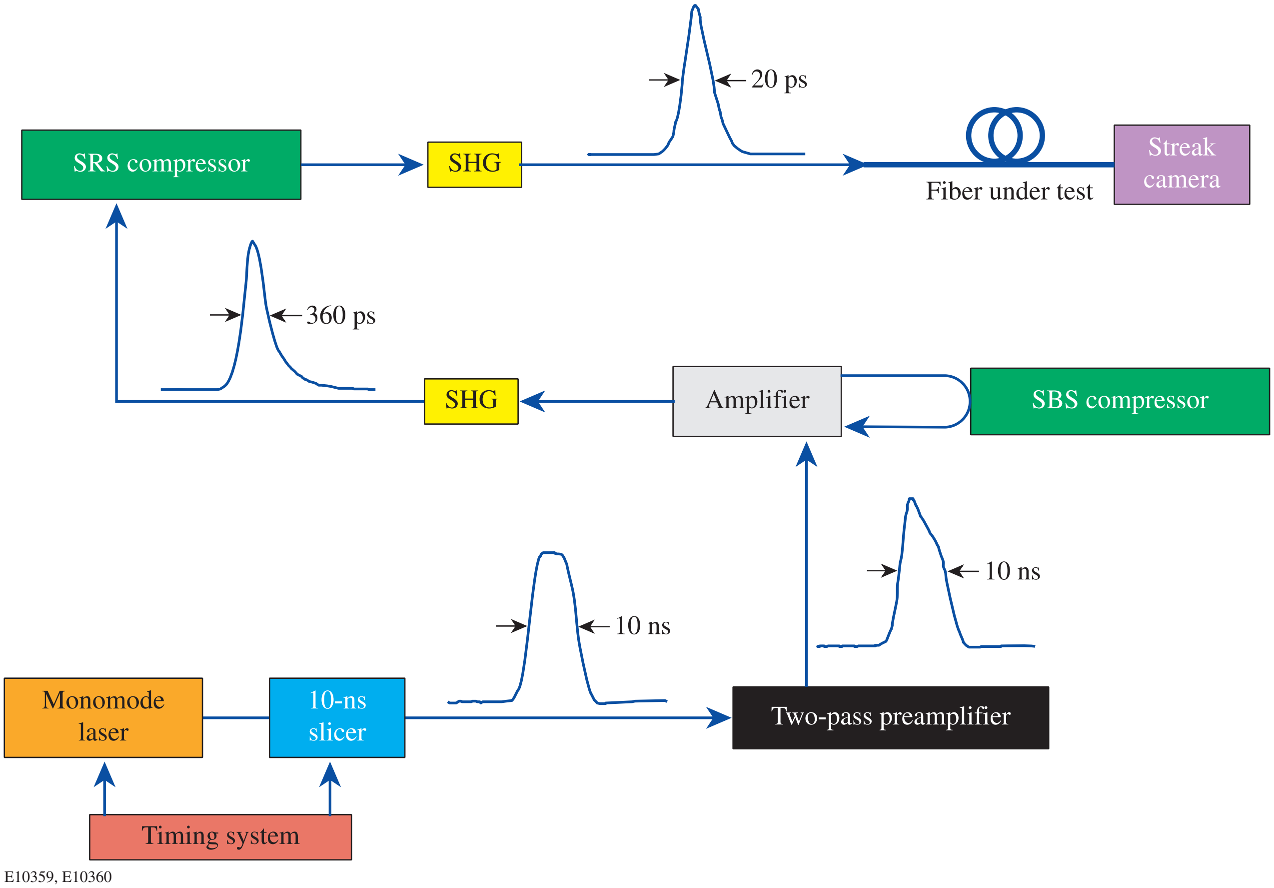

Figure 85.32
Schematic diagram of the SBS–SRS pulse-compression laser system that produces 500× compressed pulse in UV. The system can be externally synchronized.

length of the fiber under test. The modal dispersion was measured to be 0.3 to 0.7 ps/m, depending on the fiber preform. Hence, the single optical fiber bandwidth limited by the fiber modal dispersion is >33 GHz, which satisfies OMEGA requirements. A summary of the optical fiber parameters is shown in Table 85.II.

Table 85.II: Technical characteristics of the optical fiber.

Core diameter	100 μm
Cladding diameter	125 μm
Coating diameter	250 μm
Core/cladding concentricity	2.5 to 3 μm
Cladding/coating concentricity	<10 μm
Core noncircularity	4% to 5%
Cladding noncircularity	1.8% to 2%
Minimum working bend radius	100 mm
Numerical aperture	0.13
Attenuation @ 351 nm	170 to 220 dB/km
Modal dispersion	0.3 to 0.7 ps/m

Fiber Bundle Manufacturing and Testing

The seven-fiber-bundle assembly requires a close matching of the individual fiber lengths. Fiber-length differences will cause a spread in time of the output pulse [see Fig. 85.33(a)], which will degrade the fiber delivery system's bandwidth. Figure 85.33(b) shows the simulated broadening of a 10-ps input pulse in a 15-m seven-fiber bundle with ±1-mm fiber-length differences. In this case, unequal fiber lengths limit the fiber delivery system's bandwidth to ~35 GHz, which is still acceptable for OMEGA applications. The goal was to maintain fiber-length differences within a ±1-mm range for seven 15-m individual fibers. A process was developed that achieved this level in fiber-length accuracy. The process started with a stainless steel tube that accepts seven fibers in a hexagonal close-pack pattern. Fibers were aligned flush with the edge of the tube using a glass slide. Using a microscope, the seven-fiber pattern was rotationally aligned to a key of FC/PC fiber connector to minimize coupling losses when the two fiber bundles were connected. Next, the seven fibers were formed into a fiber ribbon. The fiber ribbon was tensioned, and the fibers were cut flush with the edge of another stainless steel tube installed in the far end. Finally a fiber jacket was placed over the fiber bundle, and the fiber connectors were polished.

Forty fiber bundles were assembled by this method. To characterize the fiber-bundle bandwidth, a pulse propagated through a single 15-m fiber was compared with a pulse propagated through the seven-fiber bundles. Figure 85.34 shows minor spreading of the pulse in the fiber bundles caused by unequal fiber length, demonstrating that the fiber-bundle bandwidth exceeds 50 GHz.

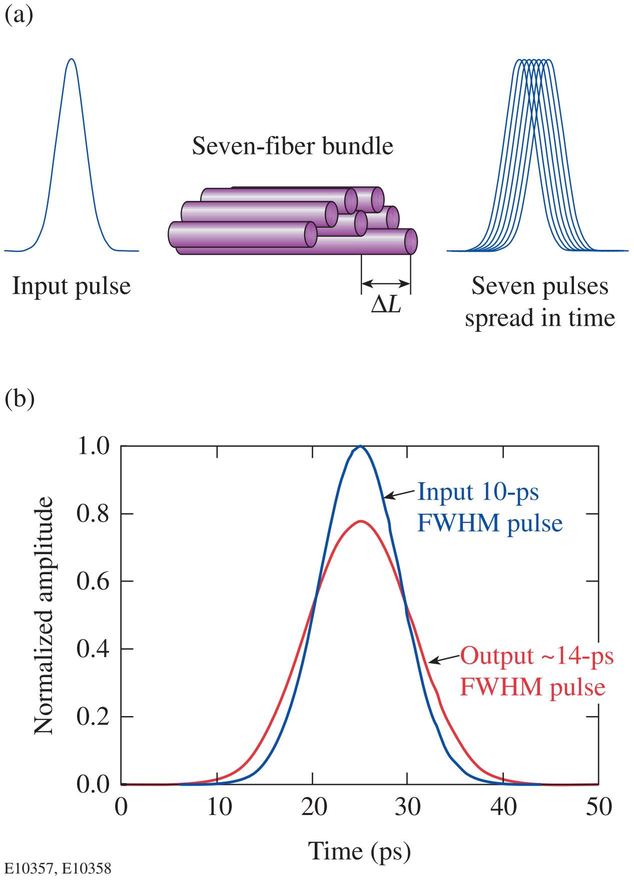

Figure 85.33
(a) A fiber bundle broadens the output pulse because of fiber-length differences that limit the bandwidth of a fiber delivery system. (b) Simulated broadening of a 10-ps pulse in a 15-m fiber bundle when $\Delta L = \pm 1$ mm.

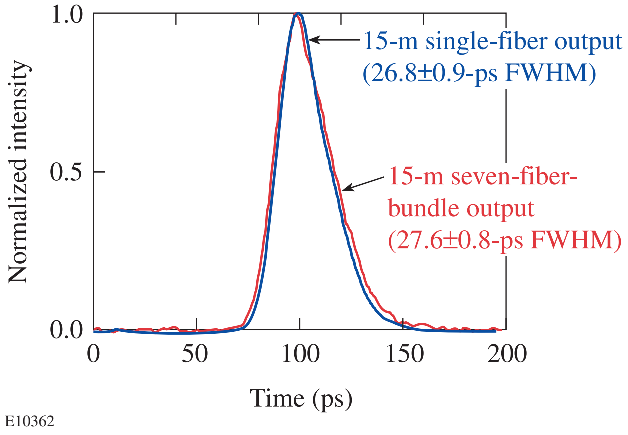

Figure 85.34
Streak camera recording of a pulse propagated through a single fiber is compared with that propagated through a seven-fiber bundle. The seven-fiber-bundle assembly procedure does not limit the bandwidth of the fiber-delivery system.

Conclusion

A special optical fiber for OMEGA laser pulse shape and power imbalance diagnostics was developed and tested. Modal dispersion of less than 1 ps/m was measured for this fiber. A fiber-bundle-assembly procedure was implemented that provides better than ±1-mm fiber length matching over a 15-m fiber length. The fiber delivery system based on these bundles has more than 30-GHz bandwidth and high transmission at 0.35-μm wavelength.

ACKNOWLEDGMENT

The high-bandwidth, UV-transmitting, graded-index optical fiber for this fiber delivery system was developed by the Vavilov State Optical Institute, St. Petersburg, Russia, for use in laser diagnostics on the NIF laser. Funding was provided by Lawrence Livermore National Laboratory. This work was supported by the U.S. Department of Energy Office of Inertial Confinement Fusion under Cooperative Agreement No. DE-FC03-92SF19460, the University of Rochester, and the New York State Energy Research and Development Authority. The support of DOE does not constitute an endorsement by DOE of the views expressed in this article.

REFERENCES

1. T. R. Boehly, R. S. Craxton, T. H. Hinterman, P. A. Jaanimagi, J. H. Kelly, T. J. Kessler, R. L. Kremens, S. A. Kumpan, S. A. Letzring, R. L. McCrory, S. F. B. Morse, W. Seka, S. Skupsky, J. M. Soures, and C. P. Verdon, Fusion Technol. **26**, 722 (1994).

2. J. M. Soures, R. L. McCrory, C. P. Verdon, A. Babushkin, R. E. Bahr, T. R. Boehly, R. Boni, D. K. Bradley, D. L. Brown, R. S. Craxton, J. A. Delettrez, W. R. Donaldson, R. Epstein, P. A. Jaanimagi, S. D. Jacobs, K. Kearney, R. L. Keck, J. H. Kelly, T. J. Kessler, R. L. Kremens, J. P. Knauer, S. A. Kumpan, S. A. Letzring, D. J. Lonobile, S. J. Loucks, L. D. Lund, F. J. Marshall, P. W. McKenty, D. D. Meyerhofer, S. F. B. Morse, A. Okishev, S. Papernov, G. Pien, W. Seka, R. Short, M. J. Shoup III, M. Skeldon, S. Skupsky, A. W. Schmid, D. J. Smith, S. Swales, M. Wittman, and B. Yaakobi, Phys. Plasmas **3**, 2108 (1996).

3. W. R. Donaldson, R. Boni, R. L. Keck, and P. A. Jaanimagi, in *Optical Pulse and Beam Propagation*, edited by Y. B. Band (SPIE, Bellingham, WA, 1999), Vol. 3609, pp. 121–127.

4. P510PSU streak tube, Philips Photonics, Slatersville, RI 02876.

5. S. Skupsky, R. W. Short, T. Kessler, R. S. Craxton, S. Letzring, and J. M. Soures, J. Appl. Phys. **66**, 3456 (1989).

6. S. R. Nagel, J. B. MacChesney, and K. L. Walker, IEEE J. Quantum Electron. **QE-18**, 459 (1982).

7. R. R. Buzyalis *et al.*, Sov. J. Quantum Electron. **17**, 1444 (1987).

Fabrication and Properties of an Ultrafast NbN Hot-Electron Single-Photon Detector

Introduction

Currently, visible photon counting is commonplace for advanced optical imaging and spectroscopy. Several types of devices, including photomultiplier tubes,[1] quantum semiconductor avalanche photodiodes,[2] and superconducting tunnel junctions,[3] have been successfully implemented. In general, such detectors work by a cascade mechanism: an incident single photon is absorbed, releasing an electron, which then instigates a multiplication process, leading to a measurable electron current pulse. Unfortunately, vacuum photomultipliers are slow and bulky and have an extremely low quantum efficiency for longer-wavelength photons. The major drawback of the most popular and most successful silicon photodiodes is that the wavelength sensitivity is limited to below 1 μm, restricted by the Si bandgap. In addition, the single-photon avalanche photodiodes exhibit low detection rates due to complicated Geiger-mode readout schemes.

The current most-pressing need is to develop practical infrared single-photon detectors, operational at either 1.3 μm or 1.55 μm, for novel quantum communication and quantum computation systems. The problem is that infrared photons carry significantly less energy than those of visible light, so in this case it is difficult to engineer an efficient electron cascade mechanism. Avalanche photodiodes based on narrow-gap semiconducting materials exhibit unacceptably large dark counts, while recently proposed single-electron transistors[4] are slow and require millikelvin temperatures and tesla-level magnetic fields.

In this article, we present a simple-to-manufacture and easy-to-operate, NbN hot-electron photodetector (HEP) with picosecond response time, high intrinsic quantum efficiency, negligible dark counts, and the capability to detect single photons from the ultraviolet to the infrared wavelength range. Our photodetector is the conversion of a well-known, unselective, superconducting hot-electron bolometer[5] into an optical and infrared wavebands quantum detector.[6] The detector consists of an ultrathin, submicron-width NbN stripe, maintained at 4.2 K and current-biased close to the critical value. The detection mechanism is based on supercurrent-assisted, temporary formation of a resistive barrier across the stripe due to photon-induced hot-spot generation. Practical implementation of this device should lead to revolutionary progress in areas ranging from ultrafast free-space satellite communication[7] through quantum computation[8] and quantum cryptography[9] to semiconductor integrated circuit testing.[10]

Device Fabrication

NbN films were sputtered onto sapphire substrates by reactive magnetron sputtering in an argon–nitrogen gas mixture. Using an optimized sputtering technique, the NbN samples exhibited a superconducting transition temperature of T_c = 10.5 K for 60-Å-thick films and 11 K for 100-Å-thick films, respectively. The superconducting transition width was equal to $\Delta T_c = 0.3$ K. A more detailed description of the NbN film deposition can be found in Ref. 11.

The fabrication process of the HEP's included several deposition and patterning manufacturing stages, resulting in the devices shown in Figs. 85.35 and 85.36. After the NbN film sputtering, TiAu alignment marks for future lithography steps and interior 5-μm × 16-μm Ti/Au contacts were formed using *e*-beam lithography and *e*-beam evaporation. Exterior contact pads for wire bonding of the entire structure were fabricated by a vacuum evaporation of 2000 Å of Au. The final, desired geometry of the NbN microbridge was achieved by ion milling the NbN film through a 200-Å-thick Ti mask placed inside the gap between the inner Ti/Au contacts. For a straight bridge (Fig. 85.35) this mask was a single 0.2-μm-wide stripe, while in the case shown in Fig. 85.36, it was a 0.2-μm-wide meander-type line covering the 4-μm × 4-μm area. After ion milling of the NbN detector, the remaining Ti layer was chemically removed.

After fabrication, each device was carefully inspected using both the AFM (Fig. 85.35) and SEM (Fig. 85.36) microscopes for bridge uniformity. In addition, the only samples selected were those in which room-temperature resistance was almost equal to the value calculated according to the structure dimensions and measured sheet resistance of the unpatterned NbN film. This procedure assured homogeneity and high quality of the superconductor microbridge, with minimal, if any, variations along its width.

Experimental Setup

The experimental setup and device connections inside an optical liquid-helium cryostat are shown schematically in Fig. 85.37. The NbN HEP was mounted on a cold plate and maintained at $T = 4.2$ K. Two cold glass filters were used to prevent the room-temperature thermal radiation from falling onto the device. The device was mounted on a rigid coplanar transmission line and connected with a cold bias-tee through a stainless steel, semirigid coaxial cable. The ac output of the bias-tee was connected to a cryogenic low-noise amplifier. Outside the dewar, the signal passed through a second power

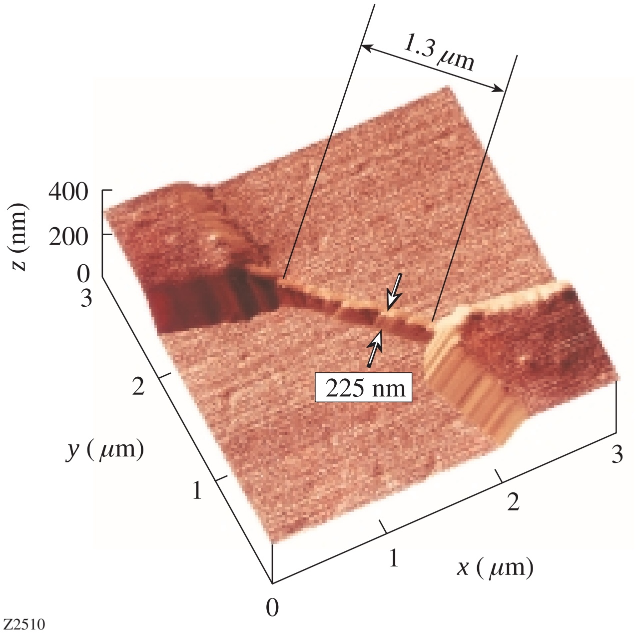

Figure 85.35
AFM image of a 1.3-μm × 0.23-μm simple bridge device.

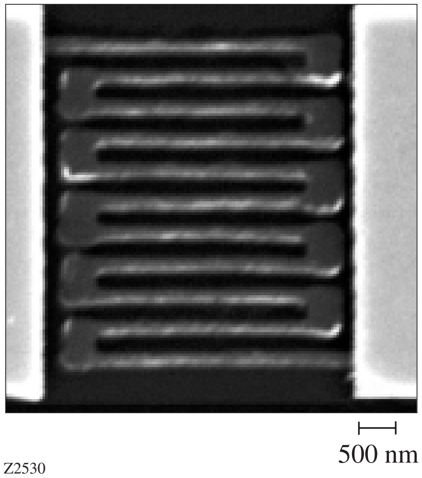

Figure 85.36
SEM photograph of a meander-type photodetector structure.

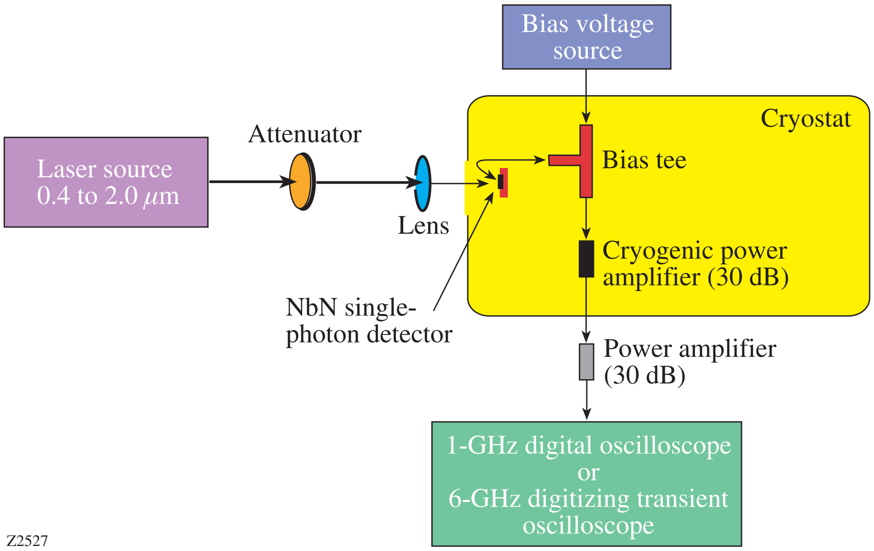

Figure 85.37
Experimental setup.

amplifier, connected to a single-shot oscilloscope and pulse counter (not shown). The oscilloscope was either externally triggered by laser pulses or self-triggered. The experiments were performed using 20-ps-wide, ~3-pJ-energy, 0.85-μm-wavelength pulses generated by a GaAs laser with a repetition rate ranging from 1 Hz to 100 kHz, or 100-fs-wide optical pulses from a mode-locked Ti:sapphire laser. In this latter case, the wavelength could be varied quasi-continuously from 0.5 μm to 2.1 μm, while the repetition rate was either 76 MHz or 1 kHz. The intensity of the laser pulses was attenuated using banks of neutral-density filters. The diameter of the beam incident on the device was always at least 200 μm, assuring stable (no "beam walking") and uniform illumination throughout the experimental session.

Experimental Results

An experimental *I-V* curve for meander-type HEP, measured by a two-point method, is presented in Fig. 85.38. The curve is typical for a long superconducting microbridge and shows that depending on the biasing condition (either purely current-bias or voltage-bias), the device switches from the superconducting, zero-resistance state to the switched, resistive state. This particular device exhibits $I_c = 80$ μA and the switched-state resistance $R = 46$ kΩ. The dashed line between points A and B in Fig. 85.38 represents the switching condition when the device is connected to a 50-Ω microwave transmission line. For a HEP biased close but below I_c (point A in Fig. 85.38), the photon absorption leads to a temporary switch along the dashed line to the metastable resistive point B. As a result, a voltage pulse is observed whose amplitude corresponds to the voltage value of point B, while the duration depends on the dynamics of formation and destruction of the resistive state induced by the photon absorption (see the **Discussion** section).

The time-resolved HEP response to a 0.85-μm-wavelength, 20-ps-wide optical pulse, captured using a single-shot, 6-GHz-bandwidth digitizing oscilloscope, is shown in Fig. 85.39. The width of the photoresponse is equal to ~150 ps and, based on our earlier electro-optic time-domain measurements,[12] is limited by the upper cutoff frequency of our amplifier chain. The signal-to-noise ratio is ~30 dB. Qualitatively, the same response pulses, with the same ~150-ps pulse widths and essentially the same amplitudes, were obtained at all the studied photon energies, independently of the incident optical pulse width, or the laser repetition rate. In addition, the response amplitude did not depend on the laser beam intensity.

Device Operation

Figure 85.39 shows the quantum nature of the HEP detector, but it does not show indisputably that it is indeed a single-photon counter. To demonstrate the latter, the statistical dependence of the number of recorded photoresponse pulses on the number of input quanta per pulse per unit area was measured. We progressively attenuated the intensity of laser pulses, using calibrated neutral density filters, and observed the decreasing number of response pulses. The experimental data allowed us to calculate the probability of recording a detector output for a given photon flux input, which is shown in Fig. 85.40 for two different device types. Curves *a* and *b* correspond to a simple,

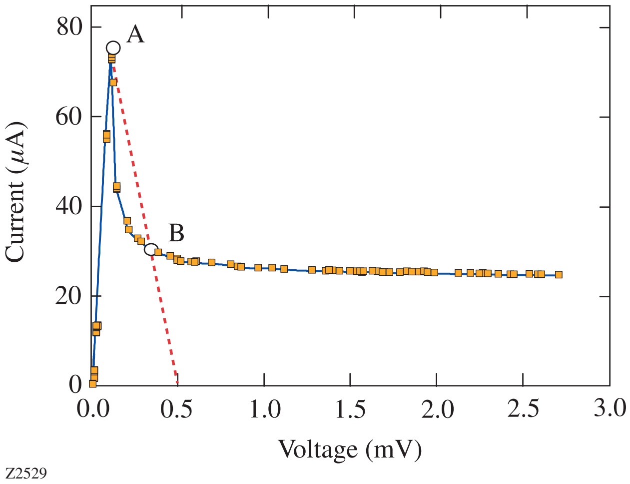

Figure 85.38
I-V curve of a meander-type device measured at $T = 4.2$ K.

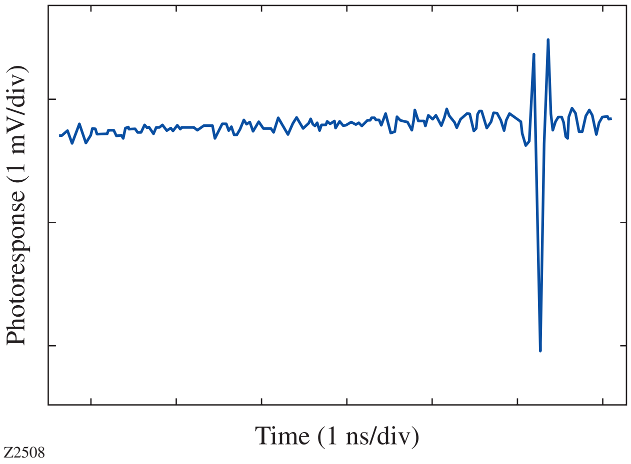

Figure 85.39
Time-resolved, single-photon-type event recorded by a single-shot digitizing oscilloscope.

1-μm-long microbridge, biased at the current value $I_b = 0.92\ I_c$ and $I_b = 0.8\ I_c$, respectively. Curves *c* and *d* are taken for a meander-type device, under the same conditions as curves *a* and *b*, respectively.

Note that while for high photon fluxes both HEP's are saturated, showing 100% efficiency in photon counting, the significant decrease in the number of photons *m* per pulse results in lower probability of recording a photon. Based on simple statistics, one can expect that for very weak photon fluxes, the probability of detecting one photon should be proportional to *m*, while the probability of simultaneously detecting two photons depends on m^2, the three-photon counting should obey the m^3 law, and so on. Indeed, we observe the linear decrease of response pulse probability versus number of quanta per unit area for curves *a* and *c*. At the same time, curve *b* follows a clear m^2 dependence, indicating a two-photon detection. Thus, the 0.92 ratio of I_{bias}/I_c is required for the single-photon operation. In general, photon detection probability versus I_{bias} was an exponentially decreasing function, indicating that the I_{bias} redistribution from the uniform state to the sidewalk-restricted flow, rather than the hot-spot formation, is the dominant factor of the device response.

The other characteristic parameter of a single-photon detector is its quantum efficiency, defined as the ratio of the number of response pulses to the number of incident photons per area for the device in the linear regime (Fig. 85.40, curves *a* and *c*). The quantum efficiency for the microbridge (curve *a*) may be estimated as 20%. The meander-type HEP's have been designed to increase both the active area of the device and its total quantum efficiency. As was expected, the absolute quantum efficiency for the meander device is significantly higher than that for the 1-μm device, but the detector's active area was increased by the factor of 80, while the quantum efficiency increased only 20 times. Thus, the intrinsic quantum efficiency for the meander HEP is equal to approximately 5%. The reason for the observed decrease in the meander device's performance might be associated with the limited uniformity of the device width over the very long length of the meander stripe. We also note that in the case of the lower bias current (Fig. 85.40, curve *b*), the meander device exhibits a nonlinear probability dependence on the photon flux.

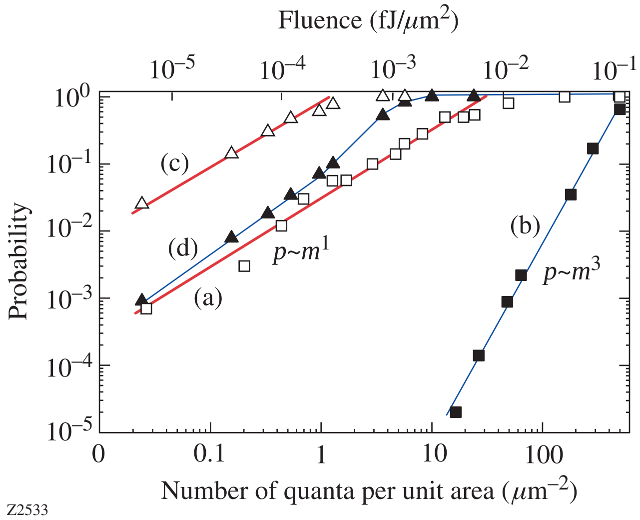

Figure 85.40
Dependence of the detector response probability on the number of incident photons per pulse per unit area. Curves *a* and *b*: microbridge-type device; curves *c* and *d*: meander-type device; △, □: $I_b = 0.92\ I_c$; ▲, ■: $I_b = 0.8\ I_c$.

Discussion and Conclusions

The physical mechanism of operation of the NbN HEP optical single-photon counter is based on supercurrent-assisted, temporary formation of a resistive barrier across the stripe due to photon-induced hot-spot generation and is presented in Ref. 13. A single optical photon is absorbed by an ultrathin, very narrow stripe of a NbN superconductor, maintained at a temperature well below T_c, and biased with I_{bias} close to the device I_c. The photon absorption generates a very high number of excited, hot electrons, leading to local suppression of superconductivity and hot-spot formation. The resistive hot spot pushes the supercurrent out of the center of the stripe, causing it to exceed the critical value for the remaining superconducting part, and leading to the formation of a resistive barrier across the entire width of the device. For the current-biased sample, this resistance results in a large, easily measurable voltage signal. The subsequent hot-electron outdiffusion and cooling lead to hot-spot healing and the collapse of the resistive barrier. The superconductivity is restored in approximately 30 ps,[12] and the detector is ready to register another photon.

The main difference between our detection mechanism and the earlier proposed hot-spot mechanism[14] is that our response is due to a collaborative effect of the bias current and the radiation quantum, leading to a large voltage output signal. To a certain extent the magnitude of the voltage pulse does not depend on the quantum energy, although the pulse shape does, providing the basis for the spectral sensitivity of the device. The rate of photon counting, which can be defined as the inverse of the total photon response time, is also a direct function of the operating parameters and can be as fast as tens of gigahertz. Finally, as we have demonstrated, depending on the device's operating parameters, our HEP can act as a single-photon, two-photon, or even three-photon quantum counter.

Our device should be able to find immediate applications, primarily in the area of ultrafast near-infrared photon counting, where there are currently no competing technologies. The 1.3-μm- to 1.55-μm-wavelength range is important for optical communication. Already-identified applications of our superconducting HEP's range from sensing ultraweak electroluminescence from submicron complementary metal-oxide-semiconductor VLSI circuits to quantum cryptography and quantum computation.

ACKNOWLEDGMENT

We wish to thank Kenneth Wilsher and Steven Kasapi for helpful discussions.

REFERENCES

1. Photomultiplier tubes, Hamamatsu Photonics K.K., http://www.hamamatsu.com (2000).
2. F. Zappa *et al.*, Opt. Eng. **35**, 938 (1996).
3. A. Peacock *et al.*, Nature **381**, 135 (1996); R. J. Schoelkopf *et al.*, IEEE Trans. Appl. Supercond. **9**, 293 (1999).
4. S. Komiyama *et al.*, Nature **403**, 405 (2000).
5. G. N. Gol'tsman, Infrared Phys. Technol. **40**, 199 (1999).
6. K. S. Il'in *et al.*, Appl. Phys. Lett. **73**, 3938 (1998).
7. G. G. Ortiz, J. V. Sandusky, and A. Biswas, in *Free-Space Laser Communication Technologies XII*, edited by G. S. Mercherle (SPIE, Bellingham, WA, 2000), Vol. 3932, pp. 127–138.
8. E. Knill, R. Laflamme, and G. Milburn, "Efficient Linear Optics Quantum Computation," (http://arXiv.org/abs/quant-ph/0006088) (2000).
9. G. Gilbert and M. Hamrick, "Practical Quantum Cryptography: A Comprehensive Analysis (Part One)," *MITRE Technical Report*, Report No. MTR 00W0000052 (http://xxx.lanl.gov/abs/quant-ph/0009027) (2000); to appear in Physics Reports.
10. J. C. Tsang and J. A. Kash, Appl. Phys. Lett. **70**, 889 (1997).
11. S. Cherednichenko *et al.*, in *Proceedings of the Eighth International Symposium on Space Terahertz Technology* (Harvard University, Cambridge, MA, 1997), pp. 245–252.
12. K. S. Il'in, M. Lindgren, M. Currie, A. D. Semenov, G. N. Gol'tsman, R. Sobolewski, S. I. Cherednichenko, and E. M. Gershenzon, Appl. Phys. Lett. **76**, 2752 (2000).
13. G. N. Gol'tsman, O. Okunev, G. Chulkova, A. Lipatov, A. Semenov, K. Smirnov, B. Voronov, A. Dzardanov, C. Williams, and R. Sobolewski, "Picosecond Superconducting Single-Photon Optical Detector," submitted to Applied Physics Letters.
14. A. M. Kadin and M. W. Johnson, Appl. Phys. Lett. **69**, 3938 (1996).

Preliminary Design of NIF 2-D SSD

Introduction

Direct-drive operation of the National Ignition Facility (NIF) will require broadband beam smoothing to successfully implode a direct-drive inertial confinement fusion (ICF) capsule and achieve high gain.[1] The base-line system parameters for NIF beam smoothing with two-dimensional smoothing by spectral dispersion (2-D SSD) are 1-THz total bandwidth in the ultraviolet, 50 × 100-μrad laser divergence, and 2 × 1 color cycle.

Broadband-beam-smoothing techniques critical to high-performance direct-drive implosions have been demonstrated successfully on OMEGA.[2] Two different configurations of a 2-D SSD system have been employed to improve irradiation uniformity. One mode producing a 1-THz bandwidth in the ultraviolet with approximately one color cycle in each SSD dimension dramatically improved direct-drive target performance, while another mode operating at only 0.35-THz bandwidth but with three color cycles in one direction also exhibited substantial benefits.[3] Both broadband 2-D SSD systems depended on a high-frequency, bulk phase modulator to realize these beam-smoothing improvements.[4]

As a partner in the National Inertial Confinement Fusion (ICF) Program, LLE has taken a lead role in defining direct-drive requirements for NIF and preparing a preliminary 2-D SSD system design to meet the beam-smoothing requirements. A prototype NIF 2-D SSD preamplifier module (PAM) will be built and tested in the Laser Development Laboratory at LLE to demonstrate satisfactory performance before transferring it to LLNL, where it will be integrated into the Preamplifier Module Laboratory. This article provides a summary of this design, including discussions of NIF features that constrain the design and direct-drive requirements.

NIF Features Influencing the 2-D SSD Design

Two aspects of NIF's direct-drive operation dictate a different 2-D SSD system architecture than was demonstrated on OMEGA:

- the longer pulses required to drive ignition-scale targets, which increases the threat of pinhole closure in the laser system's spatial filters, and

- the extremely compact space limitations of the 48 independent PAM's.

1. Pinhole Closure

Pinhole closure occurs when plasma created at the edge of a spatial-filter pinhole expands into the region of the pinhole where the laser pulse is transmitted, as shown in Fig. 85.41(a). Pinhole closure is particularly troublesome for 2-D SSD operation since the large divergence of a beam smoothed with this technique fills a large fraction of the pinhole. Plasma interactions with the beam reduce the total 2-D SSD bandwidth propagated to the target and can even distort the beam profile or retroreflect the beam, which can cause laser damage. OMEGA pulse lengths are limited to less than 3.8 ns by these pinhole closure concerns.

Pulse lengths of the order of 10 ns are required for direct-drive NIF ignition capsules.[5] This is long enough to cause significant pinhole closure, particularly for the large, 100 × 50-μrad divergence required for high-gain, direct-drive target performance. Fortunately, it is anticipated that this large 2-DSSD diver gence will be required only during the "foot" portion of the drive, when laser imprinting occurs. One solution to this problem is dynamically reducing the laser divergence after sufficient smoothing is applied, but before pinhole closure interferes with the beam. Detailed laser imprint experiments on OMEGA and early laser experiments on the NIF using a subset of beams outfitted with 2-D SSD will be required to establish the dynamic profile of this approach. Additional experiments will be performed to establish the lower limit of SSD bandwidth required late in the drive pulse to mitigate adverse laser–plasma interactions.

Since laser divergence is directly related to the product of grating dispersion and SSD bandwidth, dynamic SSD bandwidth reduction can be implemented to achieve the desired reduction. Two different approaches are available to realize dynamic bandwidth reduction. First, the microwave signal applied to a phase modulator producing the SSD bandwidth can be reduced or turned off. This approach, shown in Fig. 85.42(a), requires fast microwave switches and an electro-optic modulator with sufficient bandwidth. Highly resonant phase modulator designs like the bulk modulators used in OMEGA are unsuitable for this application, but traveling-wave integrated optic devices are commercially available.[6] Fast microwave devices with switching times of approximately 2 ns, which may be satisfactory for this application, are also available.[7]

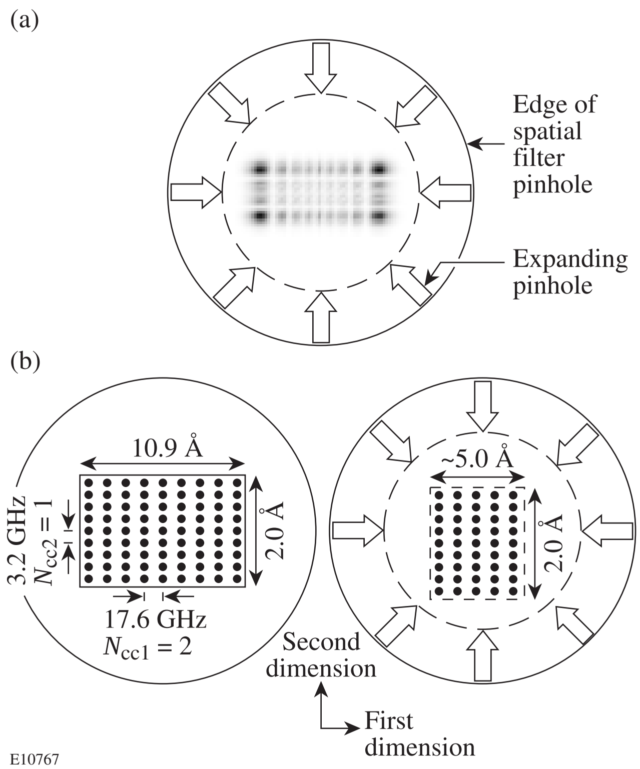

Figure 85.41
(a) Laser energy deposited at the edge of a spatial-filter pinhole creates a plasma that expands into the center of the pinhole. Pinhole closure is particularly troublesome with 2-D SSD beams since a large fraction of the pinhole is filled and the far-field energy distribution for phase-modulated 2-D SSD beams is corner-peaked. Interactions of the pinhole plasma with the SSD sidebands also convert phase modulation into amplitude modulation. (b) Dynamic bandwidth reduction can minimize the impact of pinhole closure by reducing the beam divergence before the pinhole closure affects the beam. A schematic representation of dynamic bandwidth reduction shows how full beam smoothing will be achieved during the foot of the pulse with reduced bandwidth later in the pulse.

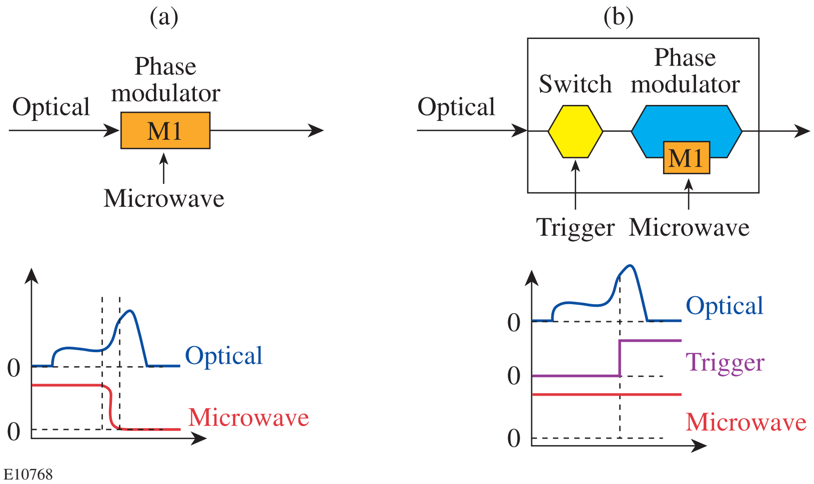

Figure 85.42
Dynamic bandwidth reduction can be implemented either electrically or optically. (a) Switching the microwave power delivered to an integrated-optic phase modulator poses the simplest approach since fast microwave switches are available, but switching times are limited to approximately a nanosecond. (b) Optical methods might also be applied to dynamically reduce SSD bandwidth during the pulse. One approach would direct the initial portion of the pulse through a phase modulator and then bypass the modulator during the latter portion.

An alternate approach to realizing dynamic bandwidth reduction for direct-drive NIF involves "optically splicing" two pulses with different SSD bandwidths, as shown in Fig. 85.42(b). This scheme produces the drive pulse in two separate sections that are combined to form the desired pulse shape and SSD bandwidth profile.

"Optical pulse splicing" offers a potential for extremely fast bandwidth reductions limited only by optical switching times of the order of ~40 ps, plus a straightforward approach for doubling the pulse-shaping contrast. Two separate front-end laser systems would be required in the Master Oscillator Room (MOR) to realize these improvements; some development would also be required. This approach is compatible with implementing ultrafast picket-fence pulses in the foot of the drive pulse, which is currently being evaluated to improve frequency-conversion efficiency and power balance.[8]

Microwave switching was selected for the base-line dynamic bandwidth reduction system since it utilizes existing technology. Preliminary design of this system has started and will be demonstrated in the NIF 2-D SSD PAM test-bed. Either approach is consistent with the all-fiber-optic front-end architecture currently implemented on the NIF.

2. Preamplifier Module (PAM) Space Constraints

A significant constraint on the NIF 2-D SSD design is the tight space limit imposed by the PAM design. A modular 2-D SSD design will be pursued so that 2-D SSD beam smoothing can be retrofitted into the first NIF PAM's built for indirect drive that will not include this feature. The PAM design integrates a high-gain, Nd:glass regenerative amplifier, beam shaping, and a four-pass amplifier on a single optical breadboard assembly that composes a line replaceable unit (LRU). In comparison, these same functions are realized in OMEGA on two large optical tables. A 2-D SSD module must fit within the PAM LRU envelope for NIF, whereas for OMEGA this functionality occupies another 4-ft × 14-ft optical table that is larger than the entire PAM assembly, shown in Fig. 85.43(a).

One side of the PAM includes the regenerative amplifier and beam-shaping module (BSM), as shown in Fig. 85.43(b). A shaped pulse launched into free space from an optical fiber is mode matched to the regenerative amplifier. This *Q*-switched cavity amplifies the pulse to approximately 20 mJ. After cavity dumping the pulse, two isolation Pockels cells provide high prepulse contrast. The beam-shaping module expands the pulse and reshapes the Gaussian beam into the square profile required to compensate the NIF gain with a serrated aperture and transmission masks. The BSM output pulse is approximately 2 mJ and is directed to the four-pass amplifier on the other side of the PAM assembly.

The four-pass amplifier side of the PAM, depicted in Fig. 85.43(c), produces up to a 17-J output pulse required to inject four separate NIF main amplifiers. A location is provided inside the four-pass amplifier for the 1-D SSD grating required for indirect drive. This side of the PAM is extremely compact.

NIF's 2-D SSD Preliminary Design

Figure 85.44 schematically highlights portions of the NIF architecture relevant to 2-D SSD. The seed pulse for all 192 NIF beams originates in the Master Oscillator Room (MOR) from a continuous-wave, single-frequency, fiber laser that is subsequently sliced into pulses and amplified. Frequency modulation is applied to the pulse by an integrated-optic phase modulator (M1). This device is actually three separate phase modulators integrated into a single package. One modulator applies a small amount of bandwidth (~0.5 Å) at a modulation frequency of ~3 GHz, which is required to suppress transverse stimulated Brillouin scattering (SBS) in the large NIF optics. The remaining two modulators are used to apply SSD bandwidth for beam smoothing. After bandwidth is applied in M1, the seed pulse is split and amplified into 48 channels, which supply each of the PAM's. All pulses with FM bandwidth are transported by polarizing (PZ) fiber to minimize FM-to-AM conversion caused by polarization mixing at fiber connectors. An arbitrary waveform generator (AWG) shapes the input pulse and provides fine timing for each PAM.

In addition to the amplification and beam shaping in the PAM, a 2-D SSD module will be added that can be bypassed during non-direct-drive NIF operation to avoid the additional system complexity and insertion loss when it is not required. Most of the 2-D SSD module will be located on the regenerative amplifier side of the PAM, including

- a "rolled" reflection grating (G2/G3),
- a bulk phase modulator (M2),
- spatial filters and telescopes required to control beam size and image relay the beam from the serrated aperture (RP_0) into the four-pass amplifier, and
- Faraday isolation stages used to double pass both the G2/G3 grating and bulk modulator.

It is significant to note that a precompensation grating (G1) for the first SSD direction is not possible with this design since the integrated-optic phase modulator (M1) is a single transverse mode device. As a result, the pulse shape is distorted by the G2/G3 grating, which is a reflection grating operated at the Littrow angle. This grating also precompensates the pulse before the second dimension of SSD bandwidth is applied by the bulk modulator (M2) and dispersed by the G4 grating. Both the first SSD dimension dispersion (G2) and second SSD dimension precompensation (G3) grating functions are accomplished with a single grating by "rolling" the grating about its input (Littrow) axis, as shown in Fig. 85.45.

The NIF 2-D SSD bulk modulator will be based on an existing OMEGA design.[9] The M2 bandwidth is dispersed in an orthogonal direction by a second 2-D SSD grating (G4)

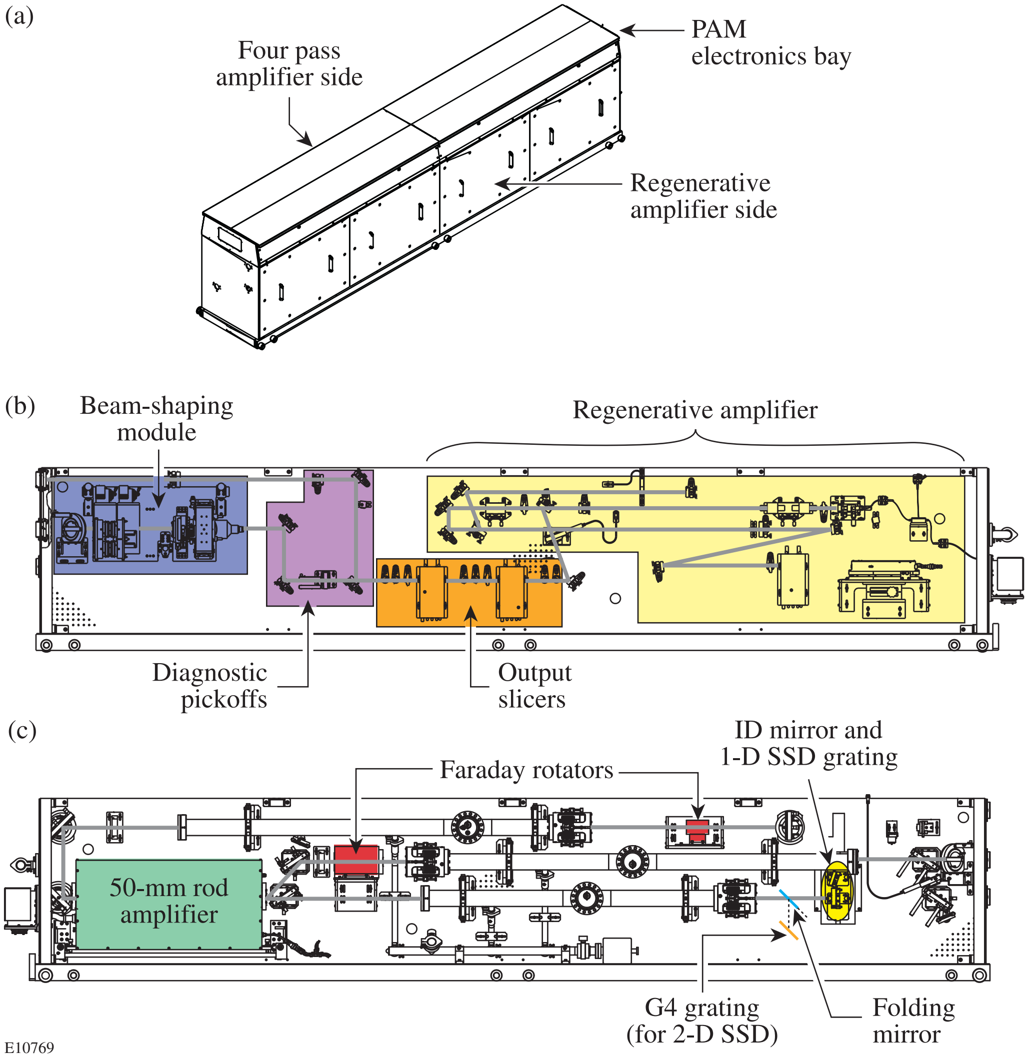

Figure 85.43
The NIF preamplifier module (PAM) poses severe space constraints on implementing 2-D SSD beam smoothing. (a) The PAM is a self-contained "line replaceable unit" that includes a regenerative amplifier (regen) and beam-shaping module (BSM) on one side of a vertically mounted optical breadboard and a four-pass amplifier on the other side. (b) The regen and BSM are highly engineered systems that ideally would require no changes when implementing a 2-D SSD module in the PAM. (c) The four-pass amplifier side is extremely compact but will require only the addition of another grating to disperse the bandwidth produced by the bulk phase modulator.

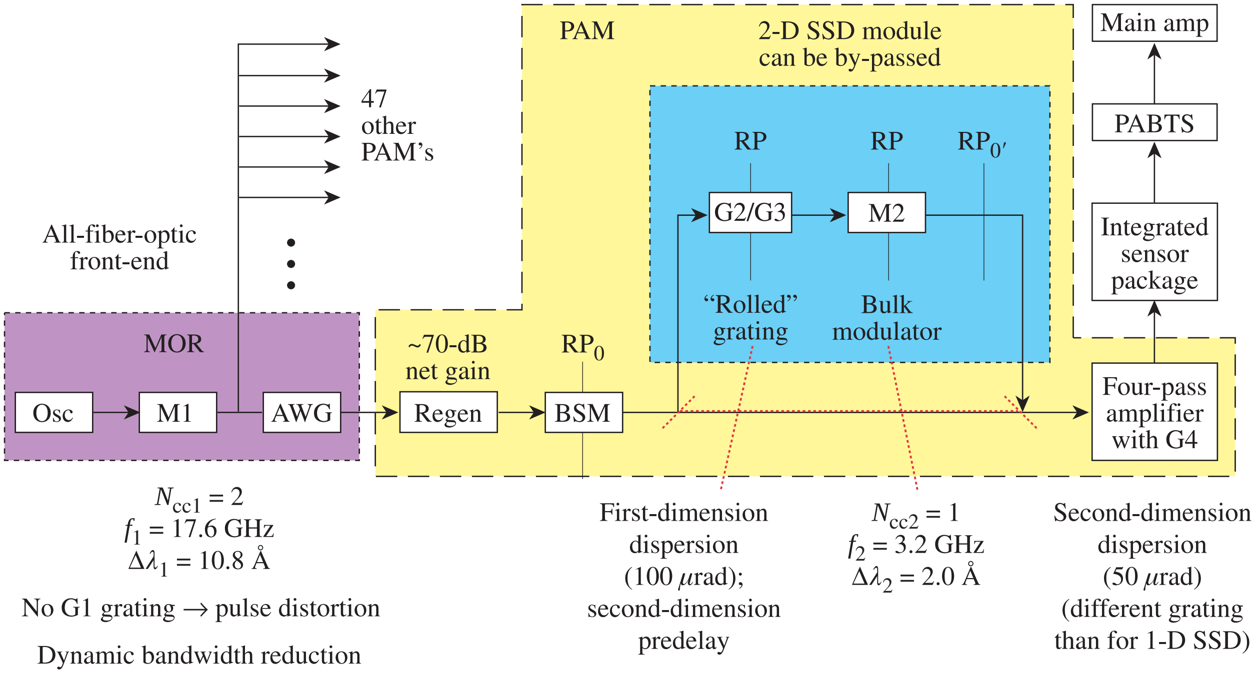

E10770

Figure 85.44
NIF architecture is significantly different from OMEGA. An all-fiber-optic front-end generates and distributes shaped pulses to 48 PAM's. The first 2-D SSD modulator (M1) is an integrated-optic phase modulator located in the Master Oscillator Room (MOR), but separate bulk modulators are required in each PAM. The BSM magnifies and spatially shapes the regen output pulse. The 2-D SSD module must be located after the BSM, where the pulse energy is lower, to avoid damaging the bulk modulator and to maximize the beam size.

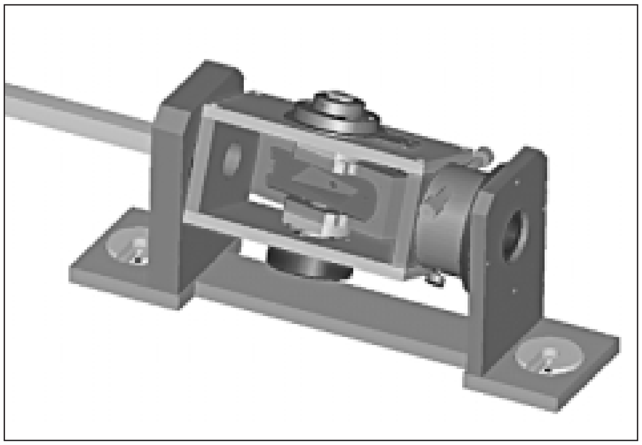

E10771

Figure 85.45
A "rolled" reflection grating performs two separate 2-D SSD grating functions by taking advantage of the vector nature of grating dispersion. It disperses the bandwidth produced by the integrated-optic modulator, and it precompensates the distortion introduced by the grating that disperses the bandwidth produced by the bulk modulator. These grating functions are identified using the same OMEGA convention as G2/G3 and G4, respectively.

located in the four-pass amplifier, as shown in Fig. 85.43(c). The G4 grating required for 2-D SSD is different from the 1-D SSD grating currently implemented for indirect-drive operation. All SSD gratings are located at image-relay planes of the serrated aperture (RP_0) in the BSM, which is image relayed throughout the laser system. After the PAM, the alignment, energy, and pulse shape of the PAM output beam are diagnosed by the integrated sensor package (ISP) and transported to the NIF's main amplifiers by the preamplifier beam transport system (PABTS).

Description of the NIF PAM Operation with a 2-D SSD Module

Figure 85.46 represents the base-line layout of the regenerative amplifier side of the PAM in which a 2-D SSD module can be realized. A key aspect of this design is that the regenerative amplifier and beam-shaping module are unchanged, and only minor changes to the existing isolation stage and diagnostic pickoffs are required to provide adequate space for the 2-D SSD module. The isolation Pockels cells are reoriented and more compactly arranged to free up space for the G2/G3 grating telescope at the bottom of the PAM, as well as in the main section of the 2-D SSD module located adjacent to the BSM. Additionally, the centering glass (RC1), diagnostic wedge (RS1), and folding mirror assemblies are reconfigured to further increase the space envelope available for the 2-D SSD module.

The output direction from the BSM will be remotely selectable by a new BM1/SM1 mirror stage. A single mirror is used to select whether the beam proceeds directly to the four-pass amplifier (BM1) for non-direct-drive operation or is diverted into the 2-D SSD module (SM1) for direct-drive operation. Figure 85.47 shows both of these configurations. This scheme provides a 2-D SSD bypass that will not affect 1-D SSD performance for indirect-drive operations, plus it does not require relocating the BSM. Operation of the 2-D SSD module is described below.

The 30-mm-square beam produced by the BSM is down-collimated by a 4× input spatial filter to a 7.5-mm-square beam (~10.6-mm diagonal) to fit through a 15-mm-clear-aperture Faraday rotator (SFR1). The spatial-filter pinhole removes high-spatial-frequency components introduced by the serrated aperture and beam-shaping masks in the BSM before the beam is imaged into the bulk phase modulator. The pinhole assembly will include the ability to remotely select its position to either "IN" or "OUT" to facilitate alignment operations. The first Faraday isolation stage extracts the pulse from the double-pass grating section of the 2-D SSD module.

The 2.25× grating telescope magnifies the beam to the correct size to achieve two SSD color cycles for the integrated-optic modulator (M1) operating at 17.6 GHz, plus to pre-compensate a single color cycle for the bulk modulator (M2)

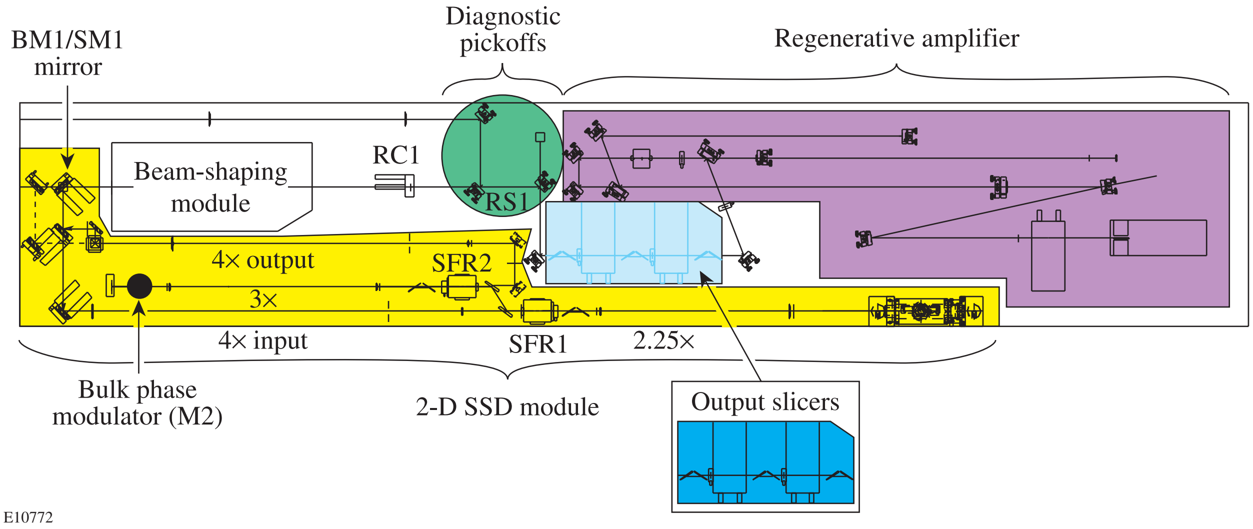

Figure 85.46
The regen side of the PAM will require minor modifications to accommodate a 2-D SSD module, but the regen and BSM will not need to be changed. The 2-D SSD module includes an input spatial filter, two Faraday isolation stages for the double-pass grating and modulator legs that include image relays, and an output spatial filter. A rotating mirror assembly (shown in Fig. 85.47) selects either indirect-drive or direct-drive PAM operation.

operating at 3.2 GHz. This image relay is sandwiched between two quarter-wave plates and preceded by polarizers to provide first-order ghost suppression in the double-pass section. Ultra-low-reflectivity antireflection (AR) coatings ($R \leq 0.05\%$) are also specified for the lenses to minimize ghost reflections since first-order ghosts will produce undesirable prepulses.

The G2/G3 reflection grating disperses the M1 bandwidth in each of two orthogonal components. The component normal to the plane of the PAM breadboard corresponds to the 100-μrad SSD divergence direction, while the in-the-plane component is matched but opposite to the dispersion produced by the G4 grating that produces the 50-μrad SSD divergence.

After the pulse is extracted from the double-pass grating section, it is injected into the double-pass bulk modulator section by a reflection off the input polarizer, in the second Faraday isolation stage. A 3× bulk modulator telescope demagnifies the beam to a 3-mm-square beam that fits the 5-mm × 6-mm-aperture bulk modulator. Like the grating telescope, first-order ghost suppression is achieved with quarter-wave plates, double polarizers, and ultra-low-reflectivity AR-coated lenses.

The bulk modulator (M2) employs a $LiNbO_3$ crystal with 1°-wedged, AR-coated input surface. A retroreflecting mirror positioned behind M2 serves to double pass the modulator crystal. The return path length is carefully set to phase match the microwave and optical fields in the modulator during the second pass.

The beam height within most of the 2-D SSD module is 105 mm. An image rotation periscope lowers the 2-D SSD beam height to 45 mm. This beam height is required to reinject the beam back into the path toward the four-pass amplifier. The beam is reinjected using a mirror located between the SM1 mirror and the breadboard hole, as shown in Fig. 85.47. The image rotation periscope also rotates the beam 90° to compensate for an additional 90° rotation introduced when the beam is passed through the PAM breadboard into the four-pass amplifier.

Both the BSM and the 2-D SSD module output beams are delivered through leaky mirrors to the ISP for alignment operations and can be individually selected by shutters (not shown).

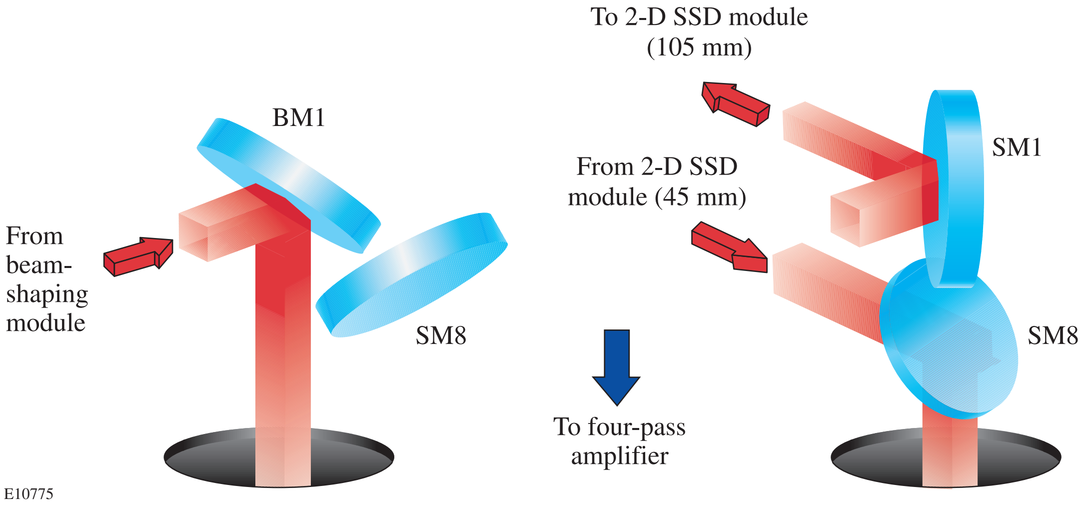

Figure 85.47
PAM operation in either the indirect-drive (2-D SSD bypassed) or direct-drive modes will be remotely selectable. A single mirror assembly rotating around the beam-shaping module's output axis will be used to reflect the beam either directly to the four-pass amplifier side of the PAM or into the 2-D SSD module. This mirror is designated BM1/SM1 and functions as a remotely operable centering mirror to support alignment in either mode. A second mirror in this rotating assembly (SM8) swings under the BM1/SM1 mirror to reflect the 2-D SSD module output beam that is returned at a 45-mm beam height. Remotely operable mirror SM7, shown in Fig. 85.46, provides the centering function during 2-D SSD operation since mirror SM8 must be stationary.

Conclusion

Direct-drive NIF operation will require a two-color-cycle, 1-THz 2-D SSD system to achieve beam smoothing required for ignition with high gain. A preliminary 2-D SSD design has been outlined in this article that is compatible with the NIF architecture and the existing PAM design. Detailed design is underway, and a prototype 2-D SSD module will be demonstrated at LLE before transferring it to LLNL for integration testing.

ACKNOWLEDGMENT

This work was supported by the U.S. Department of Energy Office of Inertial Confinement Fusion under Cooperative Agreement No. DE-FC03-92SF19460, the University of Rochester, and the New York State Energy Research and Development Authority. The support of DOE does not constitute an endorsement by DOE of the views expressed in this article.

REFERENCES

1. Laboratory for Laser Energetics LLE Review **84**, 181, NTIS document No. DOE/SF/19460-371 (2000). Copies may be obtained from the National Technical Information Service, Springfield, VA 22161.

2. Laboratory for Laser Energetics LLE Review **80**, 197, NTIS document No. DOE/SF/19460-321 (1999). Copies may be obtained from the National Technical Information Service, Springfield, VA 22161.

3. D. D. Meyerhofer, J. A. Delettrez, R. Epstein, V. Yu. Glebov, R. L. Keck, R. L. McCrory, P. W. McKenty, F. J. Marshall, P. B. Radha, S. P. Regan, W. Seka, S. Skupsky, V. A. Smalyuk, J. M. Soures, C. Stoeckl, R. P. J. Town, B. Yaakobi, R. D. Petrasso, J. A. Frenje, D. G. Hicks, F. H. Séguin, C. K. Li, S. Haan, S. P. Hatchett, N. Izumi, R. Lerche, T. C. Sangster, and T. W. Phillips, "Core Density and Temperature Conditions and Fuel–Pusher Mix in Direct-Drive ICF Implosions," to be published in Physics of Plasmas; T. R. Boehly, V. N. Goncharov, O. Gotchev, J. P. Knauer, D. D. Meyerhofer, D. Oron, S. P. Regan, Y. Srebro, W. Seka, D. Shvarts, S. Skupsky, and V. A. Smalyuk, "Optical and Plasma Smoothing of Laser Imprinting in Targets Driven by Lasers with SSD Bandwidths up to 1 THz," *ibid.*; Laboratory for Laser Energetics LLE Review **84**, 173, NTIS document No. DOE/SF/19460-371 (2000). Copies may be obtained from the National Technical Information Service, Springfield, VA 22161.

4. Laboratory for Laser Energetics LLE Review **78**, 53, NTIS document No. DOE/SF/19460-295 (1999). Copies may be obtained from the National Technical Information Service, Springfield, VA 22161.

5. C. P. Verdon, Bull. Am. Phys. Soc. **38**, 2010 (1993); Laboratory for Laser Energetics LLE Review **79**, 121, NTIS document No. DOE/SF/19460-317 (1999). Copies may be obtained from the National Technical Information Service, Springfield, VA 22161.

6. Alenia Marconi Systems, 00131 Roma, Italy (http://www.crisel-instruments.it/alenia/html/index01.htm) (2000).

7. MITEQ, Inc., Hauppauge, NY 11788 (http://www.miteq.com) (1999); M/A-COM, Inc., Lowell, MA 01853 (http://www.macom.com) (2000).

8. J. E. Rothenberg, Appl. Opt. **39**, 6931 (2000); J. A. Marozas and J. D. Zuegel, Bull. Am. Phys. Soc. **45**, 327 (2000).

9. Laboratory for Laser Energetics LLE Review **68**, 192, NTIS document No. DOE/SF/19460-139 (1996). Copies may be obtained from the National Technical Information Service, Springfield, VA 22161.

Publications and Conference Presentations

Publications

T. R. Boehly, A. Babushkin, D. K. Bradley, R. S. Craxton, J. A. Delettrez, R. Epstein, T. J. Kessler, J. P. Knauer, R. L. McCrory, P. W. McKenty, D. D. Meyerhofer, S. Regan, W. Seka, S. Skupsky, V. A. Smalyuk, R. P. J. Town, and B. Yaakobi, "Laser-Uniformity and Hydrodynamic-Stability Experiments at the OMEGA Laser Facility," Laser Part. Beams **18**, 11 (2000).

W. Göb, W. Liebich, W. Lang, I. Puica, R. Sobolewski, R. Rössler, J. D. Pedarnig, and D. Bäuerle, "Double Sign Reversal of the Vortex Hall Effect in $YBa_2Cu_3O_{7-\delta}$ Thin Films in the Strong Pinning Limit of Low Magnetic Fields," Phys. Rev. B **62**, 9780 (2000).

K. Green and R. Sobolewski, "Extending Scattering-Parameter Approach to Characterization of Linear Time-Varying Microwave Devices," IEEE Trans. Microw. Theory Tech. **48**, 1725 (2000).

D. Katsis, H. P. Chen, S. H. Chen, L. J. Rothberg, and T. Tsutsui, "Polarized Photoluminescence from Solid Films of Nematic and Chiral-Nematic Poly(*p*-phenylene)s," Appl. Phys. Lett. **77**, 2982 (2000).

R. L. McCrory, R. E. Bahr, T. R. Boehly, T. J. B. Collins, R. S. Craxton, J. A. Delettrez, W. R. Donaldson, R. Epstein, V. N. Goncharov, R. Q. Gram, D. R. Harding, P. A. Jaanimagi, R. L. Keck, J. P. Knauer, S. J. Loucks, F. J. Marshall, P. W. McKenty, D. D. Meyerhofer, S. F. B. Morse, O. V. Gotchev, P. B. Radha, S. P. Regan, W. Seka, S. Skupsky, V. A. Smalyuk, J. M. Soures, C. Stoeckl, R. P. J. Town, M. D. Wittman, B. Yaakobi, J. D. Zuegel, R. D. Petrasso, D. G. Hicks, and C. K. Li, "OMEGA Experiments and Preparation for Moderate-Gain Direct-Drive Experiments on NIF," in *C. R. Acad. Sci. Paris*, t.1, Série IV (Elsevier, Amsterdam, 2000), pp. 681–691.

S. P. Regan, J. A. Marozas, J. H. Kelly, T. R. Boehly, W. R. Donaldson, P. A. Jaanimagi, R. L. Keck, T. J. Kessler, D. D. Meyerhofer, W. Seka, S. Skupsky, and V. A. Smalyuk, "Experimental Investigation of Smoothing by Spectral Dispersion," J. Opt. Soc. Am. B **17**, 1483 (2000).

A. B. Shorey, K. M. Kwong, K. M. Johnson, and S. D. Jacobs, "Nanoindentation Hardness of Particles Used in Magnetorheological Finishing (MRF)," App. Opt. **39**, 5194 (2000).

V. A. Smalyuk, B. Yaakobi, F. J. Marshall, and D. D. Meyerhofer, "X-Ray Spectroscopic Measurements of Areal Density and Modulations in Areal Density of Compressed Shells in Implosion Experiments on OMEGA," in *Atomic Processes in Plasmas: Twelfth Topical Conf.*, edited by R. C. Mancini and R. A. Phaneuf (American Institute of Physics, New York, 2000), pp. 15–24.

Forthcoming Publications

R. Adam, R. Sobolewski, and M. Darula, "Subpicosecond Dynamics of the Switching Process in Y-Ba-Cu-O Josephson Junctions," to be published in Oxide Superconductors: Physics and Nano-engineering IV.

S. R. Arrasmith, S. D. Jacobs, I. A. Kozhinova, A. B. Shorey, D. Golini, W. I. Kordonski, S. Hogan, and P. Dumas, "Development and Characterization of Magnetorheological Fluids for Optical Finishing," to be published in the Proceedings of Fine Powder Processing '99, University Park, PA, 20–22 September 1999.

A. Babushkin, M. J. Harvey, and M. D. Skeldon, “The Output Signal-to-Noise Ratio of a Nd:YLF Regenerative Amplifier,” to be published in Applied Optics.

R. Betti and J. P. Freidberg, “Low-β, Magnetohydrodynamic Tokamak Equilibria with Poloidal Transonic Flow,” to be published in Physical Review Letters.

T. R. Boehly, Y. Fisher, D. D. Meyerhofer, W. Seka, J. M. Soures, and D. K. Bradley, “The Effect of Optical Prepulse on Direct-Drive Inertial Confinement Fusion Target Performance,” to be published in Physics of Plasmas.

D. P. Butler, Z. Celik-Butler, and R. Sobolewski, “Y-Ba-Cu-O as an Infrared Radiation Sensing Material,” to be published in the Handbook of Advanced Electronic and Photonic Materials (Academic Press, NY).

T. J. B. Collins and S. Skupsky, “Imprint Reduction Using an Intensity Spike in OMEGA Cryogenic Targets,” to be published in Physics of Plasmas.

J. A. Frenje, D. G. Hicks, C. K. Li, F. H. Séguin, R. D. Petrasso, K. Fletcher, H. Olliver, S. Padalino, S. Thompson, J. M. Soures, S. Roberts, C. Sorce, T. C. Sangster, and T. W. Phillips, “CR-39 Tract Detector Response to Charged Particles and Neutrons,” to be published in the Review of Scientific Instruments.

V. Yu. Glebov, D. D. Meyerhofer, C. Stoeckl, and J. D. Zuegel, “Secondary Neutron Yield Measurements by Current Mode Detectors,” to be published in the Review of Scientific Instruments.

G. N. Gol’tsman, O. Okunev, G. Chulkova, A. Dzardanov, A. Lipatov, A. Semenov, K. Smirnov, B. Voronov, G. Chulkova, C. Williams, and R. Sobolewski, “Picosecond Superconducting Single-Photon Optical Detector,” to be published in Applied Physics Letters.

V. N. Goncharov, P. W. McKenty, S. Skupsky, R. P. J. Town, R. Betti, and C. Cherfils-Clérouin, “Modeling Hydrodynamic Instabilities in Inertial Confinement Fusion Targets,” to be published in Physics of Plasmas.

P. A. Jaanimagi, R. Boni, and R. L. Keck, “Neutron-Induced Background in CCD Detectors,” to be published in the Review of Scientific Instruments.

S. D. Jacobs, A. E. Marino, L. L. Gregg, G. Chen, and Y. Due, “Durable Phosphate Glasses with Lower Transition Temperatures,” to be published in the Journal of Non-Crystalline Solids.

D. Katsis, D. U. Kim, H. P. Chen, L. J. Rothberg, S. H. Chen, and T. Tsutsui, “Circularly Polarized Photoluminescence from a Gradient-Pitch Chiral-Nematic Film,” to be published in Chemistry of Materials.

C. K. Li, D. G. Hicks, F. H. Séguin, J. Frenje, R. D. Petrasso, J. M. Soures, P. B. Radha, V. Yu. Glebov, C. Stoeckl, J. P. Knauer, F. J. Marshall, D. D. Meyerhofer, S. Skupsky, S. Roberts, C. Sorce, T. C. Sangster, T. W. Phillips, and M. D. Cable, “Measuring Fusion Yields, Areal Densities, and Ion Temperatures of Imploded Capsules at OMEGA,” to be published in the Review of Scientific Instruments.

V. Lobatchev and R. Betti, “Ablative Stabilization of the Deceleration-Phase Rayleigh–Taylor Instability,” to be published in Physical Review Letters.

F. J. Marshall, T. A. Ohki, D. McInnis, Z. Ninkov, and J. Carbone, “Imaging of Laser–Plasma X-Ray Emission with Charge Injection Devices (CID),” to be published in the Review of Scientific Instruments.

A. V. Okishev, R. Boni, M. Millecchia, P. A. Jaanimagi, W. R. Donaldson, R. L. Keck, W. Seka, K. V. Dukelsky, M. A. Eronyan, V. S. Shevandin, G. A. Ermolaeva, G. Nikolaev, and V. B. Shilov, “Unique High-Bandwidth, UV Fiber Delivery System for the OMEGA Diagnostic Applications,” to be published in the IEEE Journal on Selected Topics in Quantum Electronics.

A. V. Okishev, M. D. Skeldon, R. L. Keck, and W. Seka, “A New High-Bandwidth, All-Solid-State Pulse-Shaping System for the OMEGA Laser Facility,” to be published in SPIE’s Proceedings of Laser Optics 2000.

A. B. Shorey, S. D. Jacobs, W. I. Kordonski, and R. F. Gans, “Experiments and Observations Regarding the Mechanisms of Glass Removal in Magnetorheological Finishing (MRF),” to be published in Applied Optics.

M. D. Skeldon, “An Optical-Pulse-Shaping System Based on an Electrooptic Modulator Driven by an Aperture-Coupled-Stripline Electrical-Waveform Generator,” to be published in the Journal of the Optical Society of America B.

S. Skupsky, R. L. McCrory, R. E. Bahr, T. R. Boehly, T. J. B. Collins, R. S. Craxton, J. A. Delettrez, W. R. Donaldson, R. Epstein, V. N. Goncharov, R. Q. Gram, D. R. Harding, P. A. Jaanimagi, R. L. Keck, J. P. Knauer, S. J. Loucks, F. J. Marshall, P. W. McKenty, D. D. Meyerhofer, S. F. B. Morse, O. V. Gotchev, P. B. Radha, S. P. Regan, W. Seka, V. A. Smalyuk, J. M. Soures, C. Stoeckl, R. P. J. Town, M. D. Wittman, B. Yaakobi, J. D. Zuegel, R. D. Petrasso, D. G. Hicks, and C. K. Li, "Recent Progress in Direct-Drive ICF Research at the Laboratory for Laser Energetics," to be published in SPIE's Proceedings of the XXVI European Conference on Laser Interaction with Matter.

V. A. Smalyuk, T. R. Boehly, L. S. Iwan, T. J. Kessler, J. P. Knauer, F. J. Marshall, D. D. Meyerhofer, C. Stoeckl, B. Yaakobi, and D. K. Bradley, "Fourier-Space Image Processing for Spherical Experiments on OMEGA," to be published in the Review of Scientific Instruments.

V. A. Smalyuk, B. Yaakobi, J. A. Delettrez, F. J. Marshall, and D. D. Meyerhofer, "Compressed-Shell Integrity Measurements in Spherical Implosion Experiments," to be published in Physics of Plasmas.

D. J. Smith, J. A. Warner, N. E. LeBarron, T. J. Kessler, and S. LaDelia, "The Development of Ion-Etched Phase Plates," to be published in Applied Optics.

E. A. Startsev and C. J. McKinstrie, "Relativistic Ponderomotive Dynamics of a Test Particle in a Plasma," to be published in Physical Review E.

C. Stoeckl, V. Yu Glebov, D. D. Meyerhofer, W. Seka, B. Yaakobi, R. P. J. Town, and J. D. Zuegel, "Hard X-Ray Detectors for OMEGA and NIF," to be published in the Review of Scientific Instruments.

B. Yaakobi, C. Stoeckl, T. R. Boehly, D. D. Meyerhofer, and W. Seka, "Measurement of Preheat due to Fast Electrons in Laser Implosions," to be published in SPIE's Proceedings of the XXVI European Conference on Laser Interaction with Matter.

J. D. Zuegel and D. W. Jacobs-Perkins, "An Efficient, High-Frequency Bulk Phase Modulator," to be published in Applied Optics.

J. D. Zuegel and S. A. Letzring, "Bulk Microwave Phase Modulators for Smoothing by Spectral Dispersion," to be published in Applied Optics.

Conference Presentations

S. D. Jacobs and S. R. Arrasmith "Magnetorheological Finishing of Optics," ASME International Joint Tribology Conference, Seattle, WA, 1–4 October 2000.

R. L. McCrory, R. E. Bahr, R. Betti, T. R. Boehly, T. J. B. Collins, R. S. Craxton, J. A. Delettrez, W. R. Donaldson, R. Epstein, J. Frenje, V. Yu. Glebov, V. N. Goncharov, O. V. Gotchev, R. Q. Gram, D. R. Harding, D. G. Hicks, P. A. Jaanimagi, R. L. Keck, J. Kelly, J. P. Knauer, C. K. Li, S. J. Loucks, L. D. Lund, F. J. Marshall, P. W. McKenty, D. D. Meyerhofer, S. F. B. Morse, R. D. Petrasso, P. B. Radha, S. P. Regan, S. Roberts, F. Séguin, W. Seka, S. Skupsky, V. A. Smalyuk, C. Sorce, J. M. Soures, C. Stoeckl, R. P. J. Town, M. D. Wittman, B. Yaakobi, and J. D. Zuegel, "OMEGA ICF Experiments and Preparation for Direct-Drive Ignition on NIF," 18th IAEA Fusion Energy Conference, Sorrento, Italy, 4–10 October 2000.

The following presentations were made at the 16th Interdisciplinary Laser Science Conference (ILS-XVI), Providence, RI, 22–26 October 2000:

M. J. Guardalben, L. Ning, N. Jain, and D. J. Battaglia, "Investigation of Error Sources in the Liquid Crystal Point Diffraction Interferometer (LCPDI)."

J. H. Kelly, A. Babushkin, R. Boni, W. R. Donaldson, P. A. Jaanimagi, R. L. Keck, R. L. McCrory, S. F. B. Morse, A. V. Okishev, R. G. Peck, R. G. Roides, W. Seka, M. D. Skeldon, and K. A. Thorp, "Safely Operating a Large-Scale Laser Facility for Fusion Research."

T. Z. Kosc, K. L. Marshall, and S. D. Jacobs, "Polymer Liquid Crystal Flakes for Switchable Optical Devices."

K. L. Marshall, M. J. Guardalben, S. M. Corsello, M. S. Moore, I. A. Lippa, and R. P. Brecker, "Device Applications of Highly Soluble Near-Infrared Transition Metal Dyes in Liquid Crystal Hosts."

The following presentations were made at the 42nd Annual Meeting of the APS Division of Plasma Physics, Quebec City, Canada, 23–27 October 2000:

R. Betti, M. Umansky, and V. Lobatchev, "Theory of the Deceleration-Phase Rayleigh–Taylor Instability."

T. R. Boehly, "Optical and Plasma Smoothing of Laser Imprinting in Targets Driven by Lasers with SSD Bandwidths up to 1 THz" (invited).

T. R. Boehly, B. Yaakobi, J. P. Knauer, D. D. Meyerhofer, R. P. J. Town, D. Hoarty, and O. Willi, "Measurements of Shock Heating Al Absorption Spectroscopy in Planar Targets."

T. J. B. Collins and S. Skupsky, "Imprint Reduction with Shaped Pulses."

R. S. Craxton, J. A. Marozas, and S. Skupsky, "Two-Dimensional Hydrodynamic Simulations of SSD Laser Imprint."

J. A. Delettrez, S. P. Regan, P. B. Radha, and R. P. J. Town, "A New Model for the Analysis of Burnthrough Experiments on OMEGA."

R. Epstein, J. A. Delettrez, P. B. Radha, T. R. Boehly, S. P. Regan, B. Yaakobi, and J. J. MacFarlane, "Two-Dimensional Simulations of X-Ray Absorption Spectra from Nonuniformly Driven Planar Targets."

J. A. Frenje, K. M. Green, D. G. Hicks, C. K. Li, F. H. Séguin, R. D. Petrasso, T. C. Sangster, T. W. Phillips, V. Yu. Glebov, D. D. Meyerhofer, S. Roberts, J. M. Soures, C. Stoeckl, K. Fletcher, and S. Padalino, "A Neutron Spectrometer for Precise Measurements of DT Neutrons from 10 to 18 MeV at OMEGA and the National Ignition Facility."

V. Yu. Glebov, D. D. Meyerhofer, and C. Stoeckl, "Measurement of Secondary Neutron Yield by Copper Activation."

O. V. Gotchev, P. A. Jaanimagi, J. P. Knauer, F. J. Marshall, and D. D. Meyerhofer, "A High-Throughput, High-Resolution, Streaked Kirkpatrick-Baez Microscope for Planar Direct-Drive Experiments on OMEGA."

D. G. Hicks, C. K. Li, F. H. Séguin, A. K. Ram, J. A. Frenje, R. D. Petrasso, J. M. Soures, V. Yu. Glebov, D. D. Meyerhofer, S. Roberts, C. Sorce, C. Stoeckl, T. C. Sangster, and T. W. Phillips, "Charged-Particle Acceleration and Energy Loss Measurements on OMEGA."

A. V. Kanaev and C. J. McKinstrie, "Numerical Simulations of the SSD- and DPP-Smoothed Laser Beam Filamentation and Forward Stimulated Brillouin Scattering in Plasmas."

R. L. Keck, W. R. Donaldson, P. A. Jaanimagi, W. Seka, and R. Boni, "Beam Power Matching on the OMEGA Laser."

D. Keller, T. J. B. Collins, J. A. Delettrez, R. Epstein, P. W. McKenty, P. B. Radha, R. P. J. Town, G. A. Moses, P. P. H. Wilson, and J. J. MacFarlane, "Modeling Planar Burnthrough and Adiabat Experiments Using *DRACO*."

J. P. Knauer, R. Betti, T. R. Boehly, T. J. B. Collins, D. D. Meyerhofer, R. P. J. Town, and V. A. Smalyuk, "Measured Reduction of RT Growth at the Ablation Interface by Modification of the Isentrope."

M. V. Kozlov and C. J. McKinstrie, "Nonlinear Sound Waves in Two-Ion Plasmas."

C. K. Li, D. G. Hicks, F. H. Séguin, J. A. Frenje, K. M. Green, R. D. Petrasso, J. M. Soures, D. D. Meyerhofer, V. Yu. Glebov, C. Stoeckl, S. Roberts, T. C. Sangster, and T. W. Phillips, "Measurements of Areal Densities and Temperatures from DT Capsule Implosions on OMEGA."

V. Lobatchev, M. Umansky, and R. Betti, "Growth Rates of the Deceleration-Phase Rayleigh–Taylor Instability."

J. A. Marozas and J. D. Zuegel, "The Smoothing Performance of Various Picket-Fence Schemes on NIF."

F. J. Marshall, J. A. Delettrez, D. D. Meyerhofer, T. A. Ohki, S. P. Regan, V. A. Smalyuk, B. Yaakobi, and J. A. Oertel, "Monochromatic Imaging of Direct-Drive Implosions on OMEGA."

P. W. McKenty, V. N. Goncharov, R. P. J. Town, S. Skupsky, R. Betti, and R. L. McCrory, "Analysis of a Direct-Drive Ignition Capsule Designed for the NIF."

C. J. McKinstrie and M. V. Kozlov, "SBS from Fast and Slow Waves in Two-Ion Plasmas."

D. D. Meyerhofer, J. A. Delettrez, R. Epstein, V. Yu Glebov, V. N. Goncharov, R. L. Keck, R. L. McCrory, P. W. McKenty, F. J. Marshall, P. B. Radha, S. P. Regan, S. Roberts, W. Seka, S. Skupsky, V. A. Smalyuk, J. M. Soures, C. Stoeckl, C. Sorce, R. P. J. Town, B. Yaakobi, J. D. Zuegel, R. D. Petrasso, S. Padalino, J. A. Frenje, D. G. Hicks, F. H. Séguin, C. K. Li, N. Izumi, R. Lerche, T. C. Sangster, and T. W. Phillips, "Core Performance and Mix in Direct-Drive Spherical Implosions with High Uniformity" (invited).

P. B. Radha, V. Yu. Glebov, F. J. Marshall, D. D. Meyerhofer, R. D. Petrasso, S. P. Regan, W. Seka, S. Skupsky, V. A. Smalyuk, J. M. Soures, C. Stoeckl, and B. Yaakobi, "A Measurement-Based Picture of Core Conditions in OMEGA Implosions."

S. P. Regan, J. A. Delettrez, B. Yaakobi, R. Epstein, D. D. Meyerhofer, W. Seka, P. B. Radha, and R. P. J. Town, "Laser-Driven Burnthrough Experiments on OMEGA with 1-THz SSD."

F. H. Séguin, J. A. Frenje, C. K. Li, D. G. Hicks, K. M. Green, R. D. Petrasso, V. Yu. Glebov, C. Stoeckl, P. B. Radha, J. M. Soures, D. D. Meyerhofer, S. Roberts, C. Sorce, T. C. Sangster, M. D. Cable, S. Padalino, and K. Fletcher, "Secondary-Proton Spectra from D_2-Filled OMEGA Targets."

W. Seka, D. D. Meyerhofer, R. S. Craxton, S. P. Regan, R. E. Bahr, R. W. Short, B. Yaakobi, J. Fuchs, D. Montgomery, and B. Afeyan, "Stimulated Brillouin Scattering in Very Long Velocity Scale-Length NIF Plasmas."

R. W. Short, "The Effects of Beam-Intensity Structure on Two-Plasmon Decay in Direct-Drive Laser Fusion Targets."

R. W. Short and A. Simon, "Propagation of Plasma Waves in Weakly Collisional Plasmas."

A. Simon, R. W. Short, R. Betti, and V. N. Goncharov, "The Effect of Weak Collisions on Plasma Oscillations."

V. A. Smalyuk, J. A. Delettrez, F. J. Marshall, D. D. Meyerhofer, S. P. Regan, R. P. J. Town, and B. Yaakobi, "Time-Resolved Measurements of Compressed Shell Temperature and Areal Density with Titanium-Doped Targets on OMEGA."

C. Stoeckl, J. A. Delettrez, V. Yu Glebov, P. W. McKenty, and D. D. Meyerhofer, "Comparison of Neutron Burn History Measurements with One- and Two-Dimensional Hydrodynamic Simulations."

R. P. J. Town, J. A. Delettrez, V. N. Goncharov, D. R. Harding, P. W. McKenty, and R. L. McCrory, "The Effect of Elevated Internal Gas Pressure on Direct-Drive Cryogenic Target Performance."

M. Umansky, J. P. Freidberg, and R. Betti, "Stability of the Resistive Wall Mode in the Presence of Moving Walls."

The following presentations were made at the Annual Symposium on Optical Materials for High Power Lasers, Boulder, CO, 16–18 October 2000:

S. Papernov, A. W. Schmid, R. Krishnan, and L. Tsybeskov, "Using Colloidal Gold Nanoparticles for Studies of Laser Interaction with Defects in Thin Films."

A. L. Rigatti, D. J. Smith, G. L. Mitchell, J. Dirmyer, A. W. Schmid, and S. Papernov, "Moisture Barrier Coatings to Prevent Environmental Degradation of KDP Crystals."

D. J. Smith, J. B. Oliver, J. Howe, C. Stolz, and A. Rigatti, "The Use of Hafnia/Silica Multilayer Coatings on Large Mirrors and Polarizers for the National Ignition Facility."

J. Taniguchi, N. LeBarron, J. Howe, D. Smith, C. Stolz, C. Weinzapfel, and J. Kimmons, "Functional Damage Thresholds of Hafnia/Silica Coating Designs for the NIF Laser."

A. V. Okishev, "High-Energy Solid-State Lasers for ICF Applications" International Congress on "Optics-XXI Century," St. Petersburg, Russia, 16–18 October 2000.

S. P. Regan, J. A. Delettrez, B. Yaakobi, V. A. Smalyuk, F. J. Marshall, D. D. Meyerhofer, W. Seka, D. A. Haynes, Jr., and C. F. Hooper, Jr., "Characterization of Direct-Drive-Implosion Core Conditions on OMEGA with Time-Resolved Ar *K*-Shell Spectroscopy Radiative Properties of Hot Dense Matter," Santa Barbara, CA, 30 October–3 November 2000.

UNIVERSITY OF
ROCHESTER